# Encapsulation of nanomagnetite within polycaprolactone microspheres for bone replacement

by

Yi Pei Hung

A thesis submitted to the
School of Chemical Engineering of
the University of Birmingham
for the degree of
Doctor of Philosophy

School of Chemical Engineering,
University of Birmingham,
Edgbaston,
Birmingham,
B15 2TT

## Abstract

There is a clear need for the development of novel materials for bone regeneration. There is, however, with the exception of poly-(methyl methacrylate) a lack of mouldable polymeric fillers for irregular bone defects. In this thesis, we investigate the production of a new bone graft replacement combining magnetite nanoparticles with polycaprolactone (PCL) to produce a material that can soften in response to the application of an alternating magnetic field. The magnetite nanoparticles were synthesized by a non-surfactant method and then emulsified with PCL. Particle size analysis using light scattering showed that the size distributions of magnetite nanoparticles were influenced by acid concentration and mixing conditions. In contrast, the size of the PCL particles were not strongly related to the mixing conditions, but was influence by the stabilizer used during emulsification.

The magnetite nanoparticles showed superparamagnetic behaviour when analysed using SQUID. In the thermal test, magnetite nanoparticles display smooth curves both in the heating and cooling processes and do not shows significant heat loss. Scanning electron microscopy and chemical analysis showed that the magnetite nanoparticles were evenly distributed through the polymer matrix and could be caused to melt following an appropriate external magnetic stimulus. It was demonstrated that magnetite containing microspheres could successful be used for the encapsulation and delivery of antibiotics at a dose which was sufficient to be lethal to *E. coli*.

# Acknowledgments

Gratitude to my supervisor Dr. Liam Grover and my co-supervisor Gary Leeke who have provide patient and pertinent guidance throughout my PhD. In addition, I would like to thank the staff at the school of Chemical Engineering. I would also like to express my appreciations to those have offered support and help during my study, including Adrian Wright, Fiona Coomer, Ming Chu, Paul Stanley, Rory Dickerson, Stuart Hillmansen and Theresa Morris.

Thanks to my fellow PhD and master students who have been participating grand support during my stay in UK, particularly Dr A. Bolarinwa, Dr A. Smith, Dr H. Liu, Dr J. Paxton, Dr K. Zourna, Dr N. Hunt, Dr P. Jiang, Dr. S. Patel, Dr T. Willet, I. Vizcaino, P. Cao, Y. Tan, Y. Yao, and the group of Biochemical Engineering.

Thank to my family with my genuine affections, especially to the selfless devotion from my mother. I would like to thank my brother, Ming-Chun and my fiancé, Chun-Hung for all the spiritual supports and encouragements.

**To Mum, Dad, Ming-Chun and Chun-Hung**

# Table of Contents

# List of Figures

# List of Tables

# Chapter 1 Introduction

As the mean age of the population increases, there is a growing need for new methods to regenerate diseased and damaged bone (Braddock *et al.*, 2001). The current most frequently used approach to fill bone defects is the tissue graft, which can be harvested from the patient (autograft), a cadaver (allograft) or an animal (xenograft) (Kawamura and Urist, 1988; Teixeira and Urist, 1998), (Murray *et al*., 1993) before implantation. Numerous problems, however, are associated with each of these approaches. In the case of autografts, the harvesting procedure can be traumatic and can result in a range of complications including pain, morbidity and gait disturbance (Schmelzeisen *et al*., 2003). Allografting is associated with some major ethical issues (Stock and Vacanti, 2001) and bone xenografts are not typically used in the UK due to concerns with interspecies disease transmission (Teixeira and Urist, 1998). These problems have stimulated research into the development of new treatment methods utilising synthetic materials, which may be applied with or without cells and other temperature sensitive therapeutic molecules. Polymeric materials, in particular, have been investigated widely for this purpose. Examples of polymeric materials previously investigated for use as bone graft replacements include: alginate, chitosan, gelatin, hyaluronic acid (HA), poly-(ethylene glycol) (PEG), poly-(ε-caprolactone) (PCL) and poly-(L-lactic acid) (PLLA) (Rezwan *et al*., 2006)

PCL is not cytotoxic, is of relatively low cost and can degrade over a period of years in the body. It has been suggested that electrospun PCL is a potential candidate scaffold for bone tissue engineering (Sinha *et al*., 2004). As PCL can soften at relatively low temperatures (45 ℃ to 60 ℃), it has been proposed that it can be used to deliver a range of heat sensitive therapeutic

entities (cells, proteins) that may be effective in stimulating new bone formation. To date, however, without directly heating the polymer outside the body prior to application, nobody has reported a method that allows PCL to be moulded to irregular defects (Coombes *et al*., 2004; Abukawa *et al*., 2006). One possible approach could be the generation of heat by an immobilised particulate, such as nanomagnetite, which has been used in many medical applications and is accepted in body (Matsura *et al*., 2004; Ito *et al*., 2004).

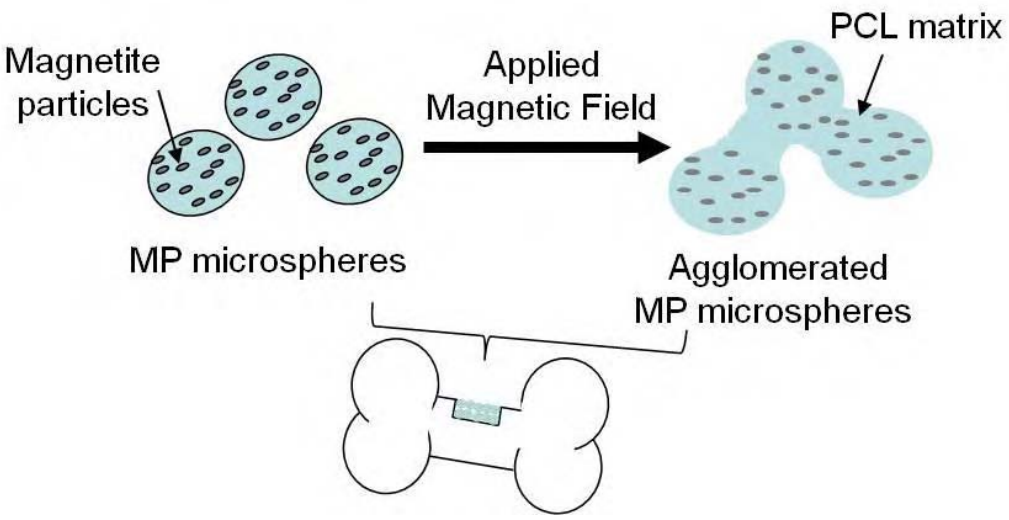


**Figure 1.1 Nanoscale magnetite was encapsulated within a polymeric matrix, which was subsequently melted in an alternating magnetic field. The softened material could be moulded into irregular defects.**

The objective of this study was to process microspheres of poly-(caprolactone) containing nano-scale magnetite. As shown in Figure 1.1, when placed in a magnetic field the local production of heat by the magnetite particles may cause the PCL to soften. Once softened, the magnetite/PCL

(MP) microspheres can be deformed and moulded into irregular defects such as those encountered in a wide range of bone traumas.

# Chapter 2 Bone and bone replacements

## 2.1 Bone replacements

Bone, to a certain extent, may repair itself following injury. However, certain diseases and treatments may result in extensive bone-loss. In these cases, a bone graft may be employed with the aim to: fill the bone defects (preventing fibrous ingrowth), stimulate bone growth and play a structural role (Froum *et al*., 2002). In the United Kingdom, health care is alone set to cost over £900 million and this cost will rise with an increasing ageing population, each year (Chrischilles *et al*., 1994). Due to osteoporosis, there are 150,000 fractures (wrist, vertebral and hip) in the UK, each year (Reeve and Metz, 1998). Moreover, an estimated 500,000 to 600,000 bone grafting procedures are performed annually in the United States (Bucholz, 2002). In 2007, a leading bone grafting materials company reported sales over 700 million dollars in the US, and the global orthobiologics market was reported that which worth nearly US$3.1 billion in 2009 (Krohn, 2008, Espicom Business Intelligence, 2010).

Over all, synthetic bone grafts have numerous advantages over tissue grafts including unlimited supply, easy sterilization and storage. Furthermore, tissue grafts are associated with poor handling properties, variable rates of resorption, poor performance in diaphyseal defects and potentially adverse effects on normal bone remodeling (Bucholz, 2002). Autografts lack sufficient availability, may be of poor quality, and result in trauma to the donor site. The use of allograft is associated with ethical issues and can also result in disease transmission. Disease transmission is also the main problem associated with xenografts (Teixeira and Urist, 1998; Patience *et al*., 1997).

## 2.2 Tissue grafting replacements

The problems associated with bone tissue grafting have driven research to develop new synthetic materials, to replace bone with ceramics, cements, metals and polymers. In addition, there is a growing need for bone regeneration due to bone infections, bone tumors and bone loss by trauma. The materials may or may not be absorbable, and can be naturally derived materials or synthetic materials, such as polymers. Recent research has primarily focused on biodegradable and biocompatible materials; both naturally derived and synthetic (Burg *et al*., 2000, Braddock *et al*., 2001, Stevens *et al*., 2008).

### 2.2.1 Currently used biodegradable materials

Currently used biomaterials for resorbable bone replacements could be classified into three types: ceramics, hydrogels and synthetic polymers.

Ceramics

Ceramics have been commonly used for bone replacements as they can have a composition similar to bone and may be osteoconductive. There are several types of ceramic materials, such as, alumina, calcium sulphate hemihydrate, bioglass and calcium phosphates. The most widely studied calcium phosphate ceramics include ß tricalcium phosphate (ß-TCP), hydroxyapatite (HA) and biphasic calcium phosphate (BCP) (Hollinger and Battistone, 1986; Burg *et al*., 2000; Grover *et al*., 2006).

Hydrogels

Hydrogels are an appealing material because they are structurally similar to the extracellular matrix of many tissues. The formation of hydrogels occurs under relatively mild conditions, and they may be delivered in a minimally invasive manner. Novel methods to control material degradation have been engineered into many hydrogels. Furthermore, hydrogels encapsulating cells have been applied for regeneration of skin, bone and many different types of tissues (Hunt and Grover, 2010). Several naturally derived materials may be used to form hydrogels, including agarose, alginate, chitosan, collagen, fibrin, gelatine, and hyaluronic acid (Drury and Mooney, 2003, Seol *et al*., 2004, Xiong *et al*., 2001).

The term alginate refers to a family of polyanionic copolymers derived from brown sea algae and comprises 1,4-linked β–D-mannuronic (M) and α–L-guluronic (G) residues in varying proportions. Sodium alginate is soluble in aqueous solutions and forms stable gel at room temperature. It has found biomedical and biotechnology applications mainly as a material for encapsulation and immobilisation of a variety of cells for immunoisolatory and biochemical processing applications (Drury and Mooney, 2003, Wang *et al*., 2003).

Chitosan is a biodegradable natural polymer that has been shown to improve wound healing. It can be produced in various forms including film, sponge and its degradation rate can be controlled. It is a 1,4 linked 2-amino-2-deoxy-β-D-glucan derived from chitin, poly-β-(1→4)-N-acetyl-D-glucosamine, and therefore the biologic origin of the aminopolysaccharide allows multiple bioactivites, for example, low toxicity, biocompatibility, biodegradability, antimicrobial,

and wound-healing properties (Drury, and Mooney, 2003; Lee *et al*., 2000; Seol *et al*., 2004; Yin *et al*., 2003). In vitro investigation demonstrated that chitosan sponges support the differentiation of seeded osteoblastic cells as well as their proliferation (Seol *et al*., 2004).

Gelatin is obtained through a controlled denaturation of the fibrous insoluble protein collagen, a major component of skin, bone and connective tissue. It displays several attractive qualities: It does not show antigenicity or resorbability *in vivo* and its physicochemical properties may be suitably modulated (Yin *et al*., 2003).

Hyaluronic acid is a linear polysaccharide composed of a repeating disaccharide. It is a simple glycosaminoglycan (GAG) and is found in nearly every mammalian tissue and fluids. It is especially prevalent during wound healing and in the synovial fluid of joints and usually degraded by hyaluronicdase, allowing cells in the body to regulate the clearance of the material in a localized manner (Drury and Mooney, 2003).

Synthetic Polymers

Synthetic polymers are commonly used for bone replacement. The local tissue responses to polymers *in vivo* depend on the biocompatibility of the polymer as well as the by-products of its degradation (Hollinger and Battistone, 1986). Diverse types of polymer have been widely used in biomaterial engineering to form scaffolds in the form of sponges and nanofibres (Ikada, 2006). Furthermore, polymers can be easily formed into polymer-based biocomposites with other type of materials. For example, nano-hydroxyapatite (NHAP) and composite scaffolds may serve as an

excellent 3D substrate for cell attachment and migration in bone regeneration and tissue engineering. (Burg *et al*., 2000, Wei and Ma, 2004).

There are various kinds of polymeric materials for bone replacements and their modes of application depend on the resultant structures and physiochemical properties. For example, biodegradable and absorbable polymeric fillers will disappear over time, or porous scaffold allow room for bone growth into the scaffold constructs. Polymers are also used for the delivery of cells and other therapeutic entities. Therapeutic objects are added into polymeric carriers prior to implantation. For instance, polymeric sponges are used to grow osteoblasts in a 3D structure for transplantation into a site for bone regeneration (Lee *et al*., 2000). There is some research focused on developing nanomaterial for tissue or bone replacements, such as nanofibre fabrication and nanopolymers. These kinds of materials supply highly porous microstructures for cell attachments and migration to better mimic the natural bone (Wei and Ma, 2004, Yashimoto *et al*., 2003).

Some widely used polymeric materials for bone replacements include polyether (such as poly-ethylene glycol (PEG)) and polyester (such as poly-caprolactone (PCL) and poly-L-lactic acid (PLA)); use depends on different purposes and methods of application (Yoon and Fisher *et al*., 2006). For example, PLA satisfies many biomaterial requirements, such as controlled porous architecture, and appropriate mechanical properties, and has been used as a scaffold for engineering. It is one of the biodegradable polymers and has been demonstrated to be biocompatible and degrade into non-toxic components with a controllable degradation rate *in*

*vivo* (Xiong *et al*., 2001, Wei and Ma, 2004, Gross and Rodriguez-Lorenzo, 2004). In addition, PCL is a polymer lacking toxicity, is of low cost and degrades at an appropriate rate. It has been suggested that electrospun PCL is a potential candidate scaffold for biomaterial and tissue engineering (Hutmacher, 2000). One researcher reported that while the relatively high transition temperature of PCL (65 ℃) is likely to have a beneficial effect on the structural integrity of the scaffold, the key different can be attributed to the processing methods and resulting different structures (Yashimoto *et al*., 2003).

## 2.3 BMPs/osseoactive factors or growth factors and drug delivery

Bone morphogenetic protein (BMP) is a group of proteins responsible for a variety of events in embryogenesis and in the postnatal skeleton. BMPs have been shown to play a role in embryological bone formation, osteo-induction, and bone repair as well as the possibility that they may assist in the replacement of autogenous bone graft (Drury and Mooney, 2003). Osteoblast transplantation using polymers scaffolds is a promising strategy that may overcome the limitations of traditional bone graft materials (Wang *et al*., 2003, Seol *et al*., 2004). There are some growth factors and cells that can be used in tissue repair, e.g. stem cells and fibroblasts, have been applied as drug delivery systems in bone replacements. The use of growth factors has the potential to markedly increase scaffold effectiveness (Rosa *et al*., 2004; Yashimoto *et al*., 2003).

# Chapter 3 Polycaprolactone

## 3.1 General physicochemical properties

Researchers have investigated the use of poly-caprolactone (PCL) for 80 years; and many of its physicochemical properties, such as biodegradability, drug permeability, non-toxicity, were established between the 1930s and 1970s (Sinha *et al*., 2004). PCL exhibits a molecular weight from 1000 to over 100,000 which affects the properties of resultant products (Chen *et al*., 1998; Fields *et al*., 1974; Tang *et al*., 2004). PCL's melting point ($T_m$) is dependent on Mw and can range from 45 ℃ to 60 ℃, it usually has a glass transition temperature ($T_g$) around -60 ℃ and biodegrades in a period from weeks to years. The degradation of PCL in human body may be affected by molecular weight, crystallinity, environment and temperature (37 ℃). (Ali *et al*., 1993; Coombes *et al*., 2004).

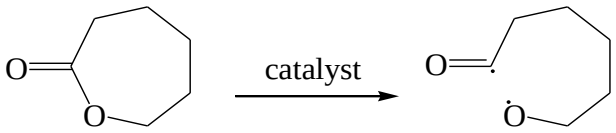


caprolactone

**Figure 3.1 Initiation of open-ring polymerization in the monomer of PCL.**

Caprolactone monomers are polymerized to form polycaprolactone of different molecular weight and copolymers via a ring opening polymerization as shown in Figure 3.1. PCL presents good solubility in organic solvents, such as dichloromethane, toluene and chloroform. PCL is a semi-crystalline polymer and has a high permeability due to its low $T_g$ point, which makes PCL a potential candidate in drug delivery and tissue engineering. The crystallinity of PCL is affected

by temperature and the chemical production in the environment (Pitt *et al*., 1979; Parthiban *et al*., 2010).

## 3.2 PCL based biomaterials and their composites

Polymers can be formulated into spheres, which have attracted huge interest from researchers as they can be used to synthesis supports for cell growth and tissue replacement (Abukawa *et al*., 2006). Advantages of PCL includes low cost, slow degradation and biocompatibility, a variety of products of PCL composites are formed by combining drug, cell and several biomaterials (Williams *et al*., 2005). PCL composites can be simply divided into two categories, PCL based biomaterials and as therapeutic carriers; and many processing methods can be used to synthesise a range of PCL composites.

### 3.2.1 PCL based biomaterials

Much research has been undertaken with composites of PCL and other materials to enhance stress crack resistance and compatibility. To broaden the field of application of PCL, structure and chemistry can be varied by altering process methods (Parthiban *et al*., 2010). Rearrangement of polymer chain structures has been investigated by using different catalyst methods and varying the temperature and time of the polymerization process. Copolymers of PCL in diblock and triblock with poly (D,L-lactide) (PLA), poly (hydroxyl acids) (PHA) and other polyesters were reported to improve mechanical properties, enables some control over degradation rate and allows manipulation of structural shape (Pitt *et al*., 1981; Ural *et al*., 2000).

The production of covalently attached inorganic substances enabled the fabrication of a range of tissue engineering scaffolds and drug delivery systems (Rhee, 2003). For example, PCL covalently bonded to silica has been shown to initiate apatite formation and enables good bone attachment *in vitro*. Hydroxyapatite (HA) and other calcium phosphate based materials are often used to form a composite with PCL, because of their chemical similarity to natural bone and osteoconductivity (Kim *et al*., 2004[1]; Yang *et al*., 2008). Moreover, PCL particles on the nanoscale have been of interest in developing drug delivery and targeting systems by encapsulating magnetite, which has been used in PCL applications not only in tissue engineering but also in pharmaceutics and tumor therapy (Kim *et al*., 2002).

### 3.2.2 Therapeutic carrier

Pharmaceutical application of PCL has attracted a great deal of interest in therapeutic substance delivery due to its high permeability and biodegradability. Porous PCL scaffolds are popular candidates for delivering of drugs, growth factors and proteins, and preventing fibrous tissue ingrowth while providing an idea environment for cell proliferation (Abukawa *et al*., 2006). In addition, mineralized tissue formation was also observed following osteoblast penetration into PCL scaffolds (Yoshimoto *et al*., 2003). PCL containing gentamicin, bovine serum albumin, insulin, nerve growth factor and so on have been reported, providing evidence that such molecules can be encapsulated by PCL alone and once released have activity *in vivo* (Sinha *et al*., 2004).

## 3.3 Fabrication of PCL biomaterials

The fabrication of PCL and PCL composites depends on the derived applications. Generally, PCL has to be dissolved or melted before further processing. Single and double emulsions with oil in water (o/w) and water in oil in water (w/o/w) systems are commonly used to form PCL microspheres and nanospheres. Polymer emulsification combined with solvent evaporation can be utilized for drug encapsulation within hydrophobic polymers. The emulsification and stabilization agents also affect the resultant products of PCL and copolymers (Perez *et al*., 2000; Chen *et al*., 2000).

Hybrid coating by spray drying or solution immersion can be employed to combine non-organic substances with PCL particles and scaffolds. Non organic layers, like HA, can be loaded onto the PCL surface and formed a uniform coating to enhance the biocompatibility and hydrophilicity of polymers (Yang *et al*., 2008; Kim *et al*., 2004[2]).

Porous PCL scaffolds have been made by electrospinning, which enables fibre synthesis on the nanoscale, providing space for drug coating and room for cell proliferation to occur. Electrostatic fibre spinning allows ejection of PCL solution toward a grounded collector via a fluid jet at a constant flow rate and a high voltage. After that, a non-woven fabric will be cut at the required size and then sterilized before further drug or cell loading process (Yoshimoto *et al*., 2003).

Porous fabric-like PCL scaffolds can also be easily produced by hot-melt homogenization followed by precipitation casting (Oh *et al*., 2007). Melted mixture blending is also a fast and of

relatively lower cost which enables production of polymer blends without considerable degradation and trans-reaction from chemicals (Antunes *et al*., 2005). A polymerization reactor undertakes proper catalyzed ring opening process and formulation of copolymers; the catalyst temperature, duration dimer or trimer catalyst ratio are controllable (Ural *et al*., 2000). Moreover, controlling the 3D structures and pore sizes of tissue replacements propose further approaches of scientists (Luciani *et al*., 2008).

# Chapter 4 Fundamentals of magnetism and magnetite nanoparticles

## 4.1 Magnetism

Magnetism is a subject, which has been studied for more than thousand years; when a selection of ores was found to be 'attractive' or 'magnetic'. In Europe, iron or Lodestone was later used for navigational purposes in a compass. The first mention of a magnetic device used for establishing direction can be found in a Chinese manuscript dated about 1040. The term magnetism describes a range of materials but can be diamagnetic, paramagnetic, ferromagnetic and antimagnetic (Getzlaff, 2008).

The symbol of a magnetic field can be referred to either B or H, which are different in both unit and definition. The B field is also defined as the magnetic induction or flux density, and the unit is Tesla (T) in the SI system and gauss (G) in the CGS system, where one T is equal to 10,000 G. The field induced by either pole (south and north poles) of a bar magnet or a magnetic material and therefore occurs an internal magnetic field. The H field, which is also defined as the field strength and the unit is ampere per meter (A $m^{-1}$) in the SI system and is oersted (Oe) in the CGS system. The B field and the H field is in a linear relationship and in accordance with Equation 4-1, where μ is the magnetic permeability of the materials (Chen, 1986; Crowell, 1998).

$$B = \mu H \qquad \text{Equation } 4-1$$

Figure 4.1 shows the magnetic field pattern around a bar magnet, which is created by the superposition of the dipole fields of individual iron particles. The field looks like a big dipole

especially farther away from the magnet and bears some resemblance to the magnet's rectangular shape in the area closest to the magnet (Crowell, 2008).

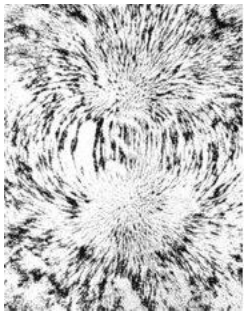

**Figure 4.1 A typical magnetic field represented by iron filings around a bar magnet (Crowell, 2008).**

The biggest natural magnetic field is the earth. Permanent magnets can oscillate about a vertical axis through their centre, and always turn and come to rest in the same approximately N-S direction at a given point on the earth's surface. One end is called an N-seeking or N pole of the magnet and the other end is S pole (Duffin, 1990). There are several types of equipment that can supply measurements of magnetism and alternating magnetic fields, such as a Superconducting Quantum Interference Device (SQUID) (Lee *et al*., 2005), a Vibration Sample Magnetometer (VSM) (Asmatulu *et al*., 2005) and Physical Property Measurement System (PPMS) (Lee *et al*., 2006).

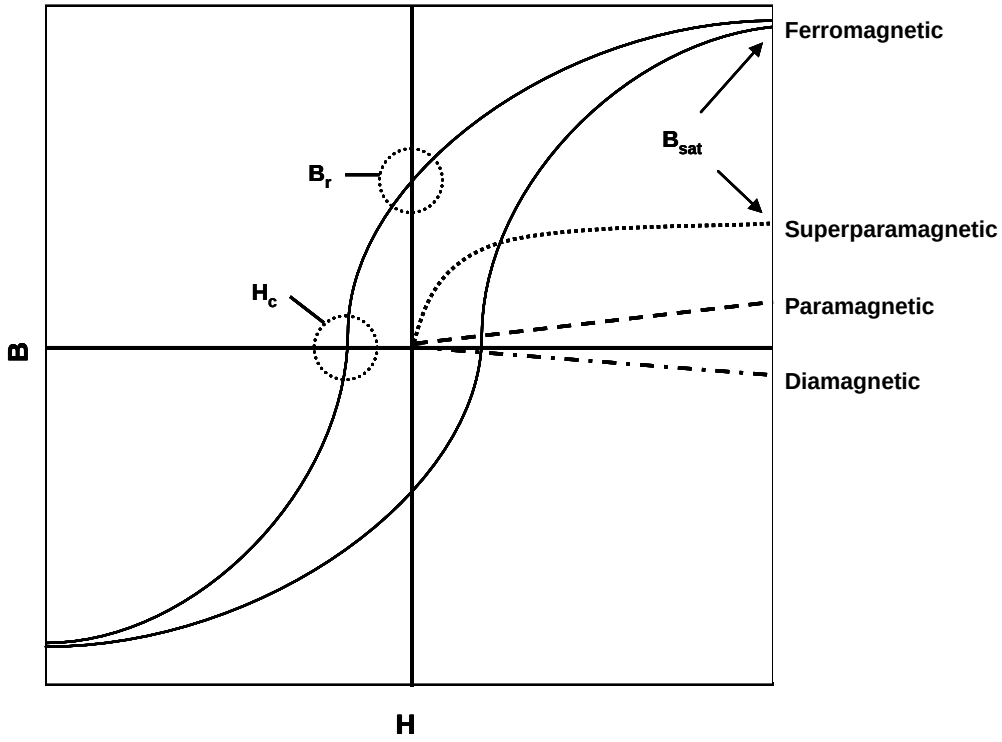


**Figure 4.2 Magnetization curves for dia-, para-, superpara- and ferromagnetic materials showing the shape and approximate relative magnitude of the magnetisation (Heeboll-Nielsen, 2002).**

Different magnetic effects can be observed when magnetisms like paramagnetism, diamagnetism and ferromagnetism, in matter are formed. Figure 4.2 shows the shape of magnetization curves for the different types of magnetism (Heeboll-Nielsen, 2002). The magnetization will saturate when in high values of H, which is described as $B_{sat}$; and $B_r$ is the remnant magnetization, the value is the magnetic field of the ferromagnetic materials after removal of external field. The coercivity ($H_c$) is the point at which the B-field is zero. There are only few substances are ferromagnetic, for example iron; and some iron alloys and ceramics can be found this kind of properties (Hatch and Stelter, 2001).

### 4.1.1 Paramagnetism and Diamagnetism

If materials contain magnetic moments which can be aligned in an external magnetic field and will amplify the field, then such substances have the property of paramagnetism. In contrast to ferromagnetic materials (ferromagnetism), there is no permanent magnetization remaining in paramagnetic materials when they are removed from the magnetic field. The characteristic of paramagnetism can be understood by postulating permanent atomic magnetic moments, which can be re-oriented in an external field. These moments can be either due to orbiting electrons or due to atomic nuclei. The torque applied by an external magnetic field on these moments will tend to fix them parallel to the field, which then reinforces it (Chen, 1986).

Living things mostly consist of diamagnetic molecules. Nearly all organic substances, some metals like Hg, and superconductors below the critical temperatures are all diamagnetic. An external magnetic field induces magnetic dipoles that are oriented antiparallel with respect to the exciting field due to Lenz's rule (magnetic field is produced in a induced current and the magnetism is parallel to the electromotive force). Therefore, the susceptibility, $\chi$, of diamagnetism is negative, as shown in Equation 4-2; while that of paramagnetism is characterized by $\chi^{para} > 0$ (Getzlaff, 2008; Simon and Geim, 2000).

$$x^{dia} = constant < 0 \qquad \text{Equation 4-2}$$

### 4.1.2 Ferromagnetism

Particles which have unpaired electron spins align them spontaneously so that the material can show magnetizations without being in a magnetic field; such particles are called ferromagnetic. Ferromagnetism is a so-called cooperative phenomenon, where single atoms cannot exhibit ferromagnetism, but the ferromagnetic properties arise when some of the atoms are bound together in solid form. Ferromagnetic particles exhibit permanent magnetization when they are removed from magnetic fields. If the field is reversed, ferromagnetic material will initially resist the field change, however most domains will eventually switch their magnetization vectors and come to the same inverse magnetization (Elliott, 1998).

## 4.2 Fundamentals of magnetite nanoparticles

### 4.2.1 Preparation of nanomagnetite

Nanomagnetite has been intensively used as fundamental scientific material and for many technological applications (Lee *et al*., 2005); due to a variety of properties include magnetism, catalytic, conduction and biological acceptance (Matsura *et al*., 2004). Accepted applications of magnetite nanoparticles are for example: magnetic storage media (Terris and Thomson, 2005), Ferro fluids (Sahoo *et al*., 2005), magnetic resonance imaging (MRI) (Cunningham *et al*., 2005), magnetically guided drug delivery (Dobson, 2006), magnetic bio-separation (Safarik and Safarikova, 2004), medical diagnosis (Mornet *et al*., 2004) and cancer therapy (Zhang *et al*., 2002).

Colloidal suspensions containing ultra-fine ferro- or ferromagnetic particles are known as magnetic fluids, or normally as Ferro fluids (Odenbach, 1993), (Scholten, 1983). In 1965, Papell from NASA, developed magnetite nanoparticles for aerospace technology. Nanomagnetite was produced by grinding micron sized material for around 1,000 hours (Papell, 1965); this elaborate procedure is costly and time consuming. Then, Shimoiizaka produced magnetic fluid via chemical co-precipitation, in 1966; nanomagnetite was acquired from the reaction of alkaline and a liquid combining ferric and ferrous ion (Shimoiizaka, 1966). In 1972, Khalafalla and Reimers achieved an improvement to the process by removing the complex process of absorbing surfactant on the surface of nanomagnetite particles; instead, the magnetic fluid was produced by co-precipitation and directly introduced into the mixture with surfactant. This method was been named as the peptization technique (Khalafalla and Reimers, 1980).

The preparation processes of nanomagnetite have been improved to attain particles with required shapes, sizes and magnetism. The production methods of magnetite nanoparticles can be separated generally into two approaches, physical and chemical methods.

## Physical method

For many applications, nanoparticles produced from the gas phase are of interest due to their physical properties. One of the major methods is to evaporate particulate materials in a tube furnace containing ultra-pure nitrogen. Homogeneous nucleation of the vapour takes place during the cooling process downstream of the furnace. Particles then grow during homogeneous condensation and proceed with the coagulation of primary particles. The coagulation leads to

agglomerates that are poly-disperse in the aerosol. The aerosol is charged by a UV charger. The particles are then selected using a differential mobility analyser (DMA). In a second furnace tube, the step of reshaping by heating takes place. This is necessary for obtaining spherical nanoparticles is desired. The size distributions of the nanoparticles are narrowed by a second DMA, the particles are then deposited in an electrostatic precipitator (ESP) (Krinke *et al*., 2002).

The other major physical method for magnetic nanoparticles is electron beam deposition. Dediu *et al*., 2007, have grown epitaxial magnetite ($Fe_3O_4$) thin film by electron beam ablation on spinel substrates. The electron beam method uses a pulsed plasma system for ablation. The deposition takes place in a reactive which reduce atmosphere from hematite target. The thin films contain no impurities, are homogenous over the entire surfaces, and are ferromagnetic at room temperature (Dediu *et al*., 2007).

Magnetic nanoparticles have long been of interest to science and have been synthesized for their size and morphologies. However, nanometre scale obtaining particles by physical routes suffers from the inability of poor size and shape controlled such as particles produced by gas phase deposition and electron beam lithography (Gupta and Gupta, 2005).

## Chemical methods

The size, composition and even morphology of nanomagnetite particles can be appreciably controlled by wet chemical methods, which are simpler, more attractive, and efficient (Gupta and Gupta, 2005). Iron oxides, $Fe_3O_4$ and $Fe_2O_3$, can be synthesized from $Fe^{3+}$ and $Fe^{2+}$ aqueous solutions with addition of base (Reimers and Khalafalla, 1972). Synthesized magnetite

nanoparticles by co-precipitation of ferric and ferrous ions is undertaken typically in a ($Fe^{3+}$ : $Fe^{2+}$) 2 : 1 molar ratio (Gupta and Curtis, 2002).

Co-precipitations of magnetite nanoparticles can be achieved by addition of extra base, for example, NaOH, $NH_4OH$, LiOH and KOH; the alkalis have different effects on the saturation magnetization of products. NaOH is a good choice because of its reasonable price, easy availability and does not lead to unwanted product (such as α-FeOOH) in the precipitate (Chen, 1993). Jeong and colleagues have reported that selected urea or ammonia can be used for controlling size distribution by pH value (Jeong *et al*., 2006). Passing $N_2$ to keep the process oxygen free is vital to the production of nanomagnetite. The aerobic condition can critically affect the physical and chemical properties of the nanosized magnetic particles. Bubbling $N_2$ gas through the solution limits the oxidation of the magnetite and reduces the particle size (Gupta and Curtis, 2004; Kim *et al*., 2001). According to the thermodynamics of co-precipitation, the pH value of $Fe_3O_4$ precipitate should be between pH 9 and 14 in an inert atom. Otherwise, $Fe_3O_4$ can also be oxidized as $Fe(OH)_3$. The overall reaction may be written as Reaction 4-1, which is under an oxygen free environment. Otherwise, $Fe_3O_4$ might also be oxidized in oxidizing environment, as shown in Reaction 4-2 (Gupta and Gupta, 2005).

$$Fe^{2+} + 2\,Fe^{3+} + 8\,OH^- \rightarrow Fe_3O_4 + 4\,H_2O \qquad \text{Reaction 4-1}$$

$$Fe_3O_4 + \frac{1}{4}O_2 + \frac{9}{2}H_2O \rightarrow 3\,Fe(OH)_3 \qquad \text{Reaction 4-2}$$

## Surface modifications of magnetite nanoparticles

Weak intermolecular interactions include hydrogen bonds, coordination bonds in ligands and complexes, ionic interactions, dipolar interactions, van der Waals forces, and hydrophobic interactions (Hamley, 2003). Magnetite iron oxide nanoparticles have hydrophobic surfaces with a large surface area to volume ratio. Consequently as a hydrophobic interaction, these particles agglomerate and form large clusters with an increase in overall particle size. The clusters display strong dipolar attractions to other particles and exhibit ferromagnetic behaviour (Gupta and Gupt, 2005; Hamley, 2003). The flocculation properties are increased by a global magnetization caused from remnant magnetic particles adherent to each other (Gupta and Gupta, 2005).

Since magnetic attraction exists between particles, additional Van der Waals force result in the usual aggregations, and therefore surface modification for effective stabilization of iron oxide nanoparticles is indispensable (Gupta and Gupta, 2005). Moreover, for medical applications, the stabilised magnetite nanoparticles should be nontoxic, bio-compatible, injectable and have a high-level accumulation in the target tissue organ; thus functionalized nanomagnetite have been investigated by some researches (Ito *et al*., 2005).

Surface modification and functionalization of magnetite nanoparticles are achieved by coating materials onto the particle. The nanoparticle coating can be comprised of several materials for biomedical applications including organic, inorganic, polymeric and non-polymeric materials; e. g. polyethylene glycol (PEG), Dextran, polyvinylpyrrolidone (PVP), fatty acid, polyvinyl alcohol

(PVA), polyacrylic acid, polypeptides, phosphorylcholine, chitosan and gelatine (Gupta and Gupta, 2005).

## Surface stability of magnetite nanoparticles

Stable suspensions of magnetic nanoparticles in different polar solvents are essential for biomedical applications. Surface stability in organic solvents can occur by some possible binding schemes, for example, one or two oxygen atoms supply for ions binding onto the $Fe^{3+}$ surface (Sahoo *et al*., 2001). Lee and Harris attached oleic acid by ozonolysis onto the hydrophobic surface of magnetite and made it more lypophilic. The double bonds of the oleic acid were then oxidatively cleaved by ozone to form carbonyl and carboxyl groups on the nanoparticles surface. The alkene chain in the oleic acid reacts with the ozone to form the primary ozonide. Then the azelaic acid and 1-nonanal were formed from the unstable primary ozonide and resulted in shortened carbon chains with carboxyl and carbonyl groups. The oleate unit of the oleic acid and carboxylate unit of the modifier, betain·HCl, undergo a ligand exchange reaction on the magnetite particle surface. Finally, the interfacial ligand exchange of the capping molecules was applied to make the hydrophobic particle surface more hydrophilic. The addition of these alkyl chains led to miscibility in ethanol, resulting a stable nanoparticle suspension (Lee and Harris, 2006).

Polymeric coatings on magnetic nanoparticles have numerous of applications. Inorganic particles in a cross-linked polymer matrix or network of gel can often inhibit coagulations of particles and increase monodispersity (Berry *et al*., 2003). For drug delivery and exact site targeting

applications, internalization of nanoparticles into specific cells is a critical step and is limited by three factors: short blood half-life, non-specific targeting and low efficiency of internalization of endocytosed ligands grafted on to the particles (Gupta and Curtis, 2002). If nanoparticles agglomerate or are covered by adsorbed plasma proteins, the particles are quickly cleared by macrophages before reaching the target cells. A possible approach to increase the circulation time in the blood stream is to modify the surface by poly-(ethylene glycol) (Zhang *et al*., 2002). A PEG is non-immunogenic, non-antigenic and protein resistant (Zalipsky, 1995). Gupta and Curtis increased the blood circulation time of nanoparticles by modify the particles surfaces with hydrophilic polymers. The nanoparticles were coated by PEG and were incubated with human fibroblast for 24 hours. PEG coated magnetic nanoparticles showed no influence of cell adhesion in comparison to a control cell population. In addition, it was been demonstrated that particles with PEG-modified surface can cross the cell membrane in non-specific cellular uptake (Gupta and Curtis, 2002).

### 4.2.2 Properties of magnetite nanoparticles

Iron oxide nanoparticles have been interested in their fundamental properties caused by multivalent oxidation states, abundant polymorphism, and the mutual polymorphous changes in the nanophase. A narrow size distribution for uniform physical and chemical properties is desired for technology and clinical applications (Woo *et al*., 2004).

## Magnetism in nanoparticles

In a magnetic system, the magnetic clusters represent an ensemble of atoms which possess varying properties with each additional atom. By contrast, nanoparticles do not show significant changes of their magnetic properties if the number of atoms are changed by a few. Assuming soft magnetic materials without any anisotropy, a continuous vector field of the magnetization is expected. Neglecting any crystalline anisotropy a regular domain pattern can already be present only caused by the shape, which is due to the minimization of the stray field energy. The disappearance in charges of a magnetization vector field has some conditions: it has to be divergence-free, i.e. free of volume charges, oriented parallel to the edges of the nanoparticle and to the surface to avoid surface charges, and the magnitude of the magnetization vector must be constant (Getzlaff, 2008).

Superparamagnetism is the absence of residual magnetic force between particles upon removal of the magnetic field. Nanomagnetite exhibits this property such particles are so small, approximately below 15 nm, the cooperative phenomenon of ferromagnetism is no longer observed and no permanent magnetization remains after the particles have been subjected to an external magnetic field. However, the particles still display quite strong paramagnetic properties (hence the name of the phenomenon) with a very great susceptibility. (Sorensen, 1998) The superparamagnetism of nanomagnetite particles is useful for the biomedical field in the respect of magnetic localization and dispersion of actives. The nanoparticles are conveniently controlled by supplying an external magnetic field, Jeong *et al* reported for a series of nanoparticles diameter (Jeong *et al*., 2006). At room temperature, the aerated 5 nm particles were superparamagnetic

without interaction among the particles, whereas the 19 nm particles were ferrimagnetic. The 11 nm iron oxide nanoparticles were superparamagnetic with some interactions among the particles (Woo *et al*., 2004).

## The size and morphology of magnetite nanoparticles

Each application of nanomagnetite requires different material properties; theses can be thermal, chemical, colloidal stability, magnetic characteristics, particle shape and size, and non-toxicity. The co-precipitation process showed effects on the magnetic properties by concentration variation of shape and particle size. Nedkov et al 2006 studied the influence of an oxidizing solution and the time of the Oswalt ripening process on the particles shape and size. According to XRD and TEM results, the powders obtained were mono-phase $Fe_3O_4$ with different sizes, shapes and degrees of crystallinity. The shape passes from spherical through elliptical to cubic when the oxidizing quantity increases. Then, when the volume of the oxidation solution increases, the particle sizes increase and the shape passes from elliptical to cubic. The rate of spinel arrangement increases with rising oxidation solution amounts, but the possibility for spherical particles preparing decreases (Nedkov *et al*., 2006).

Different syntheses of iron oxide nanoparticles, such as aerosol/ vapour (pyrolysis) method, gas deposition, bulk solution, sol-gel and micro-emulsion methods, have effects on the properties of the particles produced and are shown in Table 4.1 (Chen, 1986). The range of nanomagnetite sizes are between 5 to 200 nm. Nanoparticles from the micro-emulsion method have a very narrow size distribution, 4-15 nm. In the result of bulk solution method, generally,

nanomagnetites have spherical morphology, some with porosity or cubic shapes and large aggregates appear. The nanomagnetite from aerosol/vapour and sol-gel methods has similar magnetization values, 10-50 emu/g; and the particles from the bulk solution and micro-emulsion methods show superparamagnetic behaviour. The magnetite nanoparticles formed by micro-emulsion method have especially a narrow size distribution, exhibit superparamagnetism and lack particle aggregation, however low yield rates and surfactant remove from the final product are acuse for concern. Both of the advantages and disadvantages are described below.

**Table 4.1 Comparison of different features of the iron oxide nanoparticles fabricated through different methods (Chen, 1986).**

| | Synthesis of iron oxide nanoparticles prepared by | | | | |
|---|---|---|---|---|---|
| **Characteristics of the iron oxide** | **Aerosol/ Vapour (pyrolysis) method** | **Gas deposition method** | **Bulk solution method** | **Sol-gel method** | **Micro-emulsion method** |
| Size and size distribution | about 5-60nm with broad distribution | about 5-50nm with narrow distribution | about 10-50nm with broad distribution | about 20-200nm with broad distribution | about 4-15nm with narrow distribution |
| Morphology | Spherical | Spherical | Spherical (large aggregates) | Spherical with high porosity | Cubic or Spherical (no aggregation) |
| Magnetization values | 10-50 emu/g with desired magnetic property | >20 emu/g | 20-50 emu/g with superparamagnetic behaviour | 10-40 emu/g with paramagnetic behaviour | Superparamagnetic behaviour |
| Advantages | High production rate | Useful for protective coating and thin film deposition | Large quantities can be synthesized | Particles of desired shape and length can be synthesized, hybrid nanoparticles | Uniform properties and also size of the nanoparticles can be modulated |
| Disadvantages | Large aggregates are formed | Requires very high temperature | Uncontrolled oxidation of magnetite to maghemite, diamagnetic contribution | Product usually contains sol-gel matrix components at their surfaces | Surfactants are difficult to remove, only a small quantities of iron oxide can be synthesized |

## 4.2.3 Application of nanomagnetite in medicine

The characters of functional magnetic nanoparticles can be applied to a wide range of fields like biomedicine (Pankhurst, 2003) and magnetic separation for wastewater treatment and computer storage (Nedkov *et al*., 2006). This work focuses on the nanomagnetite in medicine applications. In medicine and biology, magnetite nanoparticles show much attractive practicability. It can be

applied to gene technology, as a drug carrier, and cell or object targeting, gene sieve or cell separation and tumour therapy.

As mentioned above, magnetite nanoparticles have controllable sizes ranging from a few nanometres up to tens of nanometre. These dimensions are smaller than or comparable to those of a cell (10 to 100 ìm), a virus (20 to 450 nm), a protein (5 to 50 nm) or a gene (2 nm wide and 10 to 100 nm long). Thus nanomagnetite can 'get close' to a biological entity of interest. Furthermore, they can be coated with biological molecules which them enables to interact with or bind to a biological entity. It means that magnetite particles can be applied to 'tagging' or labelled by providing a controllable absorption. Moreover, the iron oxides nanoparticles are magnetic, which means that they obey Coulomb's law, and can be manipulated by an external magnetic field gradient. The possibility of action at a distance, combined with an intrinsic penetrability of magnetic fields in to human tissue provide many applications, such as the transport and/or immobilization of magnetic nanoparticles, or magnetically tagged biological entities.

As a result, magnetite nanoparticles can be produced for delivering an object, such as an anticancer drug, or a cohort of radionuclide atoms, to a targeted region of the body, like a tumour or trauma. In addition, the magnetic nanoparticles can be made resonantly responding to a time-varying magnetic field. This is related to the transfer of energy from the exciting field to the nanoparticles. For instance, the particle can generate heat which leads to their use as hyperthermia agents; delivering toxic amounts of thermal energy to targeted bodies such as tumours; or as chemotherapy and radiotherapy enhancement agents, where more effective

malignant cell destruction results from a moderate degree of tissue warming. Many other potential applications are made available in biomedicine because of the special physical properties of magnetic nanoparticles (Pankhurst, 2003).

## Magnetic separation

Specific molecule isolation and separation are used in a wide range of biosciences and biotechnology. Over the years, the attention to magnetic separation techniques has increased. For example, protein and peptide isolation of biosciences and biotechnology is usually performed using chromatograph, electrophoresis, ultra filtration and precipitation with affinity chromatography being one of the most important techniques. However, all of the standard column liquid chromatography procedures cannot cope with samples containing particulate materials; thus, they are not appropriate techniques to early stage purification or isolation processes in which samples within are suspended solids and fouling components. Magnetically stabilized fluidized beds or magnetically modified two-phase systems have shown their usefulness. The magnetic separation of protein can be performed using a concentrated protein concentration instead of large volumes of diluted protein solution by standard a chromatography. Generally, magnetic separation is extremely gentle to the target proteins or peptides, even to large protein complexes which tend to be broken up by traditional column chromatography techniques (Safarik and Safarikova, 2004). Magnetic separation is a two-step process, including tagging or labelling of the desired entity with magnetic materials and separation of these tagged entities through a fluid-based magnetic isolation device (Zhang and Misra, 2007).

Tagging ability of magnetic nanoparticles is made possible via chemical surface modifications. Such modifications include biocompatible dextran, PVA. The magnetically labelled materials are separated from their native solution by passing the fluid mixture via a region where a magnetic field gradient exists for immobilization by a magnetic force. The force has to overcome the hydrophobic drag force acting on the magnetic particles and there is also a buoyancy force affecting the motion (Pankhurst *et al*., 2003). Following an incubation period when the target compounds bind to the magnetic particles, the whole magnetic complex is easily and rapidly removed from the sample using an appropriate magnetic separator (Safarik and Safarikova, 2004).

## Drug delivery

Another possible application of magnetic nanoparticles is in drug delivery. Magnetically targeted drug delivery can control drug aggregation on trauma areas and as higher repair efficiency. It also can be used to reduce drug doses, the cost related with drug treatment and potential side effects on healthy tissues, liver or kidney (Weissleder *et al*., 1995; Dobson, 2006).

Ideally, nanomagnetite could bear on their surface or in the bulk surface a pharmaceutical drug that could be driven to the target organ and released there. For these applications, the size, charge and surface chemistry of magnetic particles are particularly important and are strongly affected on both the blood circulation time and biocompatibility (Chouly *et al*., 1996). Larger particles, 200nm, are usually sequestered by the spleen because of its mechanical filtration and are eventually removed through the phagocyte system, which leads to decreased blood circulation times. Whereas, smaller particles of 10nm or less which are rapidly removed through

extravasations and renal clearance. The diameters of particles from 10 to 100 nm are ideal for intravenous injection and exhibited the most prolonged blood circulation times (Gupta and Gupta, 2005).

Magnetite nanoparticles have been successfully designed as a novel magnetic targeting drug carrier with characteristics of controlled release. In the study, the surface of magnetite nanoparticles was functionalized by Fe-S covalent bonds, and cross-linked with a thermo sensitive polymer, which was encapsulated with doxorubicin. According to FTIR results, the doxorubicin was chemically conjugated to the surface of the functionalized magnetite. The smart stimuli-responsive polymer showed abilities of drug delivery and controlled release by operation at a lower critical solution temperature (LCST) and pH value. The system has lower drug release at conditions below the LCST; at a temperature higher or equal to the LCST the drug release was rapid for the initial 5h, followed by a sustained release for a longer duration (Zhang and Misra, 2007). Morever, some research preceded magnetic drug delivery by utilising external magnetic fields through changing fluid speeds, magnetic distance, magnetic saturation and solid contents (Asmatulu *et al*., 2005).

## Hyperthermia affects and Heating treatments

The application of magnetic materials to hyperthermia dates back to 1957 when Gilchrist et al heated various tissue samples with 20 to 100 nm size particles of $\gamma$ -$Fe_2O_3$ exposed to a 1.2 MHz magnetic field (Gilchrist *et al*., 1957). Generally, the method includes dispersing magnetic particles throughout the target tissue, and then applying an AC magnetic field of sufficient

strength and frequency to cause the particles to heat (Pankhurst *et al*., 2003; Wada *et al*., 2003). Magnetic induction hyperthermia is one of the therapies for cancer treatment; by exposing cancer tissues to an alternating magnetic field. The magnetic field is not absorbed by the living tissues and can be applied to deep regions in the living body. Heat is generated due to magnetic hysteresis loss when magnetic particles are subjected to a variable magnetic field (Gupta and Gupta, 2005).

Cancer cells can be destroyed at temperatures higher than 43 ℃ for 30 min or more, whereas the normal cells can survive at higher temperatures. The majority of hyperthermia devices are restricted in their utility because of unacceptable coincidental heating of healthy tissue. Magnetic particle hyperthermia is appealing because it offers a way to ensure only the intended target tissue is heated (Gupta and Gupta, 2005; Gordon *et al*., 1979). The size of the magnetite crystals should be sub-micrometric, so the powders or bulk of these biomaterials have comparable properties. These kinds of materials are not only biocompatible, but also bioactive and could be useful for bone tumours (Gordon *et al*., 1979). Iron oxides, magnetite ($Fe_3O_4$) and maghemite ($\gamma$ -$Fe_2O_3$) are the most studied to date result from the generally appropriate magnetic properties and biological compatibility. Particle sizes less than about 10μm are normally considered small enough for effectively delivery to the cancer, either via encapsulation in a larger moiety or suspension in some sort of carrier fluid (Pankhurst *et al*., 2003).

Ferrimagnetic particles possess hysteretic properties when exposed to a time-varying magnetic field, which gives rise to magnetically induced heating. Measurements of the heat generation

from magnetic particles are usually quoted in terms of the specific absorption rate (SAR) in units of $Wg^{-1}$. Superparamagnetic materials are capable of generating impressive levels of heating at lower fields (Gupta and Gupta, 2005). Two time constants exist during heating the Brownian mechanism of relaxation the magnetic moment is locked to the crystal axis and when the magnetic moment aligns with the field, the particle rotates as well. A second mechanism exists (Néel relaxation) in which the magnetic moment rotates within the crystal (Rosensweig, 2002).

There are several types of heating devices for varying requirements, such as capacitive plate applicators, intraluminal applicators, microwave antennas and phased-array heating strategy. The heating device of closed-loop feedback control of microwave heating using MRI temperature monitoring, is showed in Figure 4. Using a relatively simple one-dimensional dipole antenna array, control of both temporal and spatial temperatures and specific absorption rate values is possible. Developing this kind of feedback systems for human scale and integrating them with clinical MRI scanners, the efficacy of hyperthermia treatment for a number of different cancers can be further improved (Behnia *et al*., 2002).

Interstitial heating using magnetic nanoparticles is feasible in patients with previously irradiated and locally recurrent prostate cancer. Using computed tomography (CT), deposits of magnetite nanoparticles appear at a mean density of 450 HU and can be visualized in prostate tissue with a sensitivity of around 90 %. An alternating magnetic field applicator for use in humans, with operating and variable field strengths is shown in Figure 4.3. A fibrotic thermometry unit and a computer console with application software for online thermotherapy monitoring are connected to the applicator (Johannsen *et al*., 2007).

**Figure 4.3 Alternating magnetic field applicator for use in humans (MFH300F, Mag-Force Nanotechnologies AG, Berlin) operating at a frequency of 100 kHz and a variable field strength (0-18 kA/m) (Johannsen *et al*., 2007).**

Furthermore, two or more round capacitive plate applicators energized with radio frequency electric currents are one of the systems used to supply electromagnetic energy to cancer patients undergoing hyperthermia. A system with a smaller applicator on the side nearest the tumour can more effectively heat the tumour if the applicator can be located near the tumour, and if the path between the applicators and the tumour is not too obstructed by bone. Therefore, such a system could be more desirable than a large applicator system (Orcutt *et al.,* 1990).

## Tissue repair and tissue engineering

Iron oxide nanoparticles can be used for tissue repair through welding, apposing two tissue surfaces then heating the tissues sufficiently to join them, and through soldering, where protein or synthetic polymer-coated nanoparticles are placed between two tissue surfaces to enhance joining of the tissues (Gupta and Gupta, 2005). Nanoparticles that strongly absorb light corresponding to

the output of a laser are also useful for tissue-repairing procedures. This technique can minimize tissue damage through using the least harmful wavelengths of light or lower powered light sources. Superparamagnetic nanoparticles can couple to stem cells and used to target them at the desired position in the body. In addition, various proteins, growth factors, etc., can bind to superparamagnetic nanoparticles and be delivered at the damaged tissue, where they would assist tissue development. The use of stem cells in the form of cell-based therapies are known to offer tremendous potential for disease, treatment and cures for several diseases including diabetes, cancer, heart disease, Alzheimer's and Parkinson's. Central to this process would be the ability to target and activate these stem cells at required sites of injury and repair using magnetic particle technology (Bulte *et al*., 2001).

On the other hand, since magnetic nanoparticles labelled with cells can be manipulated by magnets. A novel tissue engineering methodology using magnetic force and functionalized magnetic nanoparticles has been proposed by A. Ito and colleagues; they developed a novel methodology to construct 3-D tissue analogues of *in vivo* tissues using magnetic nanoparticles and a magnetic force. These results suggest that magnetic force-based technology is a promising approach for tissue engineering (Ito, 2004).

## Magnetic resonance imaging

There has been an increase in interest regarding the use of magnetic nanoparticles as contrast agents in magnetic resonance imaging (MRI). The magnetic field distribution of the magnetic nanoparticles can be detected using the magneto impedance sensor. Furthermore, its distribution

indicated that the magnetic nanoparticles were localized only in the tumour. When these apparatuses are available for clinical use, the diagnosis of metastatic cancer with high sensitivity will be possible (Ito *et al*., 2005).

Moreover, magnetic nanoparticles have been used to detect apoptosis by MRI. The MRI technique can detect apoptosis at an early stage in the process which has advantages over other methods like magnetic resonance spectroscopy (MRS) and radionuclide techniques (Zhao *et al*., 2001). Biocompatible magnetic particles have been hypothesized to derivatized with similar sequences and that entire particles can be efficiently ferried into haematopoietic and neural progenitor cells in quantities up to 10-30 pg of Suerparamagnetic iron per cells (Lewin *et al*., 2000). In other research, iron incorporation did not affect the cell viability, differentiation, or proliferation of CD34+ cells. Following intravenous injection into immune deficient mice, 4% of magnetically CD34+ cells homed to bone marrow per gram of tissue, and single cells could be detected by MRI in tissue samples. In addition, magnetically labelled cells that had hoped to the bone marrow could be recovered by magnetic separation columns (Gupta and Gupta, 2005). Evidence has been presented that the expression can be visualized noninvasively by MRI *in vivo*. The transgenic was used conjugated human holo-transferrin with iron oxide nanoparticles and showed an increase in receptor levels at the cell surface that can cause considerable changes in MRI signals (Weissleder *et al*., 2000).

In magnetic resonance imaging, superparamagnetic particles made of iron oxide can be used as contrast agents, and strongly influence the relaxation times which depending strongly on the size and coating of the particles (Sorensen, 1998). In comparison to paramagnetic ions, super-

paramagnetic iron oxide particles have higher molar relaxivities, and offer advantages at low concentrations as being blood pool and tissue-specific agents (Saini *et al*., 1987). The superparamagnetic iron oxide nanoparticles (SPION) label is highly sensitive to magnetic resonance detection and is also relatively non-toxic. SPION has been approved for clinical use as a blood pool agent for MRI (Nunn *et al*., 1996). Because SPION has a large surface area to volume ratio, the magnetic nanoparticles tended to agglomerate and adsorb plasma proteins (Storm *et al*., 1995).

# Chapter 5 Applications of this work

The main aim of this thesis was to produce MP microspheres which could soften by the locally generated heat from the encapsulated magnetite nanoparticles. The work presented in this thesis has two fields of application followed by the production of MP particles, as a heating source to soften MP particles and as a drug release device.

## 5.1. The use of magnetite in heating PCL

To induce the heat generated by the magnetite nanoparticles, an alternating magnetic field is required. Scientists are still keen on the achievement of an alternating magnetic field with high efficiency of heating and varied power supply for different magnetic particles (Mornet *et al*, 2004). A modified magnetic field is employed to demonstrate the heat generation of magnetite and therefore softening of MP particles.

## 5.2. Drug release from MP microspheres

Magnetite nanoparticles have applications in drug delivery and cell targeting. Nanomagnetite within PCL microspheres can also be used for localised delivery of drugs to bone (Yang *et al*, 2006). The drug release from the resultant particles and the drug efficacy after release are evaluated in the final chapter.

# Chapter 6 Physiochemical characterisations and statistical analysis

For a newly synthesised material, it is important to determine physical and chemical properties to see that it is suitable for a particular application. Nanoparticles and microparticles are the two major products in this thesis and characterisation has focussed on determining their properties. The techniques below are standard methods for particle analysis of magnetite and PCL. There are three major parts of this chapter: size distribution, morphology and physiochemical characterizations. In addition, further specific methods are described in each results chapter.

## 6.1 Particle size distribution

Particle size distributions are conventionally measured by dynamic techniques. The motions of molecules in solution are determined by fluctuation and detected by an intensity autocorrelation function built into the equipment. (Placidi and Cannistraro, 1998). In light scattering systems, a laser strikes the particle and is diffracted. The nature of diffraction can then be used to determine particle size (Eshel *et al*., 2004). Electron microscopy also be employed to determine particles size distribution.

### 6.1.1 Nanoparticles

The magnetite nanoparticles were filtered through a 0.45 mm filter; to avoid deviations given by impurities. Subsequently, the magnetite nanoparticles were dispersed in distilled water in a cuvette and a High-Performance Particle Sizer (HPPS) (HPPS, Malvern Ltd., UK) was used to determine the particle size distribution (PSD). The size distribution can be depicted as signal intensity, volume/mass moment or number of objects. In the HPPS system, the mean value of

particle size shown as Z-average, which is the cumulative mean of the signal intensity. The Z-average, however, is only comparable if the sample is monomodal, spherical and monodisperse (Rawle, Malvern Instrument Ltd.). Therefore, the other two values, volume and number given from HPPS results, can be used to observe polydisperse samples or discuss the particles dispersion behaviour.

### 6.1.2 Microparticles

The particle size of the microspheres was determined by used laser diffraction (Mastersizer 2000, Malvern Ltd., UK). The resultant PCL microspheres were dispersed into distilled water and were consequently loaded into the water flow through the laser diffraction area. The statistics from Mastersizer give three percentile readings, $d_{0.1}$, $d_{0.5}$ and $d_{0.9}$. The values of $d_{0.1}$ and the $d_{0.9}$ are the size of particles, and indicate 10% and 90% of the sample below $d_{0.1}$ and the $d_{0.9}$ respectively. The $d_{0.5}$ value is that at which 50% of the sample is smaller and 50% is larger. The width of the size distribution is given by the measurement of the value of span, which is calculated from $d_{0.1}$, $d_{0.5}$ and $d_{0.9}$ (Malvern Ltd., UK).

### 6.1.3 Statistical analysis

The statistical analysis was determined using a one-way analysis of variance, ANOVA, and paired comparison by Tukey multiple range test (Brightstat.com).

## 6.2 Morphological observation

The morphologies of the nanoparticles and microparticles were captured by different types of electron microscope.

### 6.2.1 Transmission electron microscopy (TEM)

Transmission Electron Microscopy (TEM) is useful to determine particles morphologies on the nano-scale, and allows size determination from the resulting 2D micrographs. Concentrations of magnetite nanoparticles were diluted by toluene and ultrasonicated for 2 minutes, then followed by loading carefully onto a 400-mesh carbon film (Agar Scientific Ltd., UK) and left to air-dry for approximately one to two minutes before TEM (Philips TECHNAI F20, The Netherland) analysis (Woo *et al*, 2004).

Encapsulated microspheres were sectioned and then images were captured using TEM (JEOL 1200EX, JEOL Ltd., UK). Samples were first embedded in white resin and sealed in gelatine prior to sectioning. The resulting blocks were trimmed and sections cut using an ultramicrotome prior to observation by TEM (LR White, Agar Scientific Ltd., UK).

### 6.2.2 Environmental Scanning Electron Microscopy (ESEM)

Some particles were easily dehydrated in the vacuum system of SEM and other particles are sensitive to the electron bombardment of TEM. Lower pressure SEM has been developed especially for biological samples. In the ESEM system, the morphology and analysis of specimen can be investigated under a moist environment because the water can be condensed as well as

vaporised from the sample in a controlled manner (H. M. Ortner, 1999). Furthermore, ESEM can be applied to both wet and dry samples.

A conducting layer on the surface of specimen is required in SEM system, which allows the electron beam to be conducted through the specimen. Gold film was deposited onto the surfaces of PCL and MP particles with 8 to 10 mm in thickness. Then, the images were acquired using the ESEM (Philips XL30 ESEM-FEG, USA) under a spot size 4 and 10 mm and working distance and accelerating voltages of 10 or 15 kV. Particles were mounted onto aluminium stubs with a carbon tape before sputter coating.

## 6.3 Physiochemical Characterizations

### 6.3.1 Superconducting Quantum Interference Devices (SQUID)

The magnetometer, SQUID (S100, Cryogenic Ltd., UK), was using to determine the magnetic saturation of magnetite nanoparticles and MP microspheres. The SQUID magnetometer is a high sensitivity piece of equipment capable of measurement as low as $10^{-7}$ emu to $10^{-10}$ $Am^2$ and the measurements can be made over a range of fields and temperatures (Cullity and Graham, 2009). The Josephson junction is the key element of SQUID, which is built using a thin insulating layer between two superconductors and is connected to a superconducting loop for measuring the impedance. The change of the flux applied to the loop will cause the impedance of the loop, and the impedance becomes a periodic function of the magnetic flux threading the SQUID due to the phase difference across the junction. Therefore, a bias current of modulation signal is used with a detector to measure the impedance and linear relationship of the voltage and flux. Therefore, the

sensitive about voltage-to-flux can be used to undertake flaw characterization, magnetic property analysis of materials and evaluate corrosion (Wikswo, 1995; Jenks *et al*, 1996).

### 6.3.2 X-ray diffraction (XRD)

Structural phase identification was measured by X-ray diffraction (XRD) (D8, Bruker LTD., UK). The XRD peak under the Scherrer approximation was calculated for coherently diffracted domain size ($d_{xrd}$). The peak assumes the small crystallite size to be the cause of line broadening (Thapa *et al*., 2004). Research has shown a good agreement of particle size between XRD and magnetization measurements, and it indicated that XRD technique can be used to estimate saturation magnetization values (Mahadevan *et al*., 2007).

### 6.3.3 X-ray computed microtomography (Micro-CT)

Micro-CT has recently been employed to undertake 2D and 3D analysis of bone scaffolds. In a Micro-CT system, a sample is placed onto a rotating mount and irradiations from X-ray source and sample are captured by a detector. The X-ray path captured by the detector is calculated and the attenuation coefficients are derived to convert threshold values, which allow more correlate information collecting, such as 2-D and 3-D model, porosity and density of the sample (Ho and Hutmacher, 2006).

### 6.3.4 Differential scanning calorimeter (DSC)

The thermal transitions of PCL were measured by a differential scanning calorimeter (DSC) (Pyris 1 DSC, PerkinElmer, UK). For DSC measurements, a sample is sealed in an aluminium

pan, and the temperature and heat flow of sample are monitored during heating and cooling processes. One sealed empty aluminium pan is used as reference for computing calculation. The heating rate used in this thesis is 10℃ per minute and argon gas was chosen as carrying gas to provide a reducible and dry atmosphere (Hohne *et al*., 2003).

### 6.3.5 Thermogravimetric Analysis (TGA)

Thermogravimetric Analysis (TGA) (TG209 F1 Iris® , NETZSCH-Geraetebau GmbH, Germany) was used to measure mass change and the quantity of magnetite encapsulated into PCL. The mass variation is observed under a heating process with a controlled atmosphere in an enclosed system (Brown, 2001). For the TGA measurements in this thesis, the pressure of air and nitrogen was fixed at 25 mmHg, and the heating was set from 25 ℃ to 800 ℃ (50 ℃/min) with an end-point at 820 ℃.

### 6.3.6 Fourier Transform Infrared Spectroscopy (FTIR)

Fourier Transform Infrared Spectroscopy (FTIR) (Nicolet 380 FT-IR, Thermo Scientific, USA) was used to evaluate the functional groups present in the samples by collected spectra measured by the temporal coherence of a radiative source. The Fe-O and O-H peaks were used as indicators of magnetite particles (Arruebo, 2006)

### 6.3.7 Energy dispersive Spectrometer (EDS)

An ESEM fitted with an energy dispersive spectrometer (EDS) (INCA 300 EDS, Oxford Instruments, UK) was employed to undertake compositional analysis while evaluating MP

morphology. An X-ray detector is used for detecting and converting X-rays into electronic signals which will be measured by a pulse processor to determine the energy of the detected X-ray. Then, the data analyzer carries on the peaks identification and quantitative analysis (Oxford Instruments, 2005).

# Chapter 7 The influence of process conditions on the physicochemical properties of magnetite nanoparticles

## 7.1 Introduction

The formulation of nano-scale magnetite has received a large amount of attention, due to its attractive properties to the biomedical field. Several reports have focused on producing functionalised and nano-scale magnetite by chemical and surface modification methods (Lin *et al*, 2007). The chemical modification of magnetite might be harmful to bioactive materials because of the extra acid or other chemical agents that are used; and this might limit the range of magnetite applications *in vivo*. There is, however, significant scope for controlling size distributions by changing mixing conditions. Despite this, there is relatively little reported on this in the literature. In this chapter, to achieve a simple production method of control size, magnetite nanoparticles were formulated by systematically changing mixing conditions.

This section reports the influences of varying stirring rates, dropping rates and the concentration of hydrolysis agent on particle size distribution of magnetite nanoparticles. The resulting particles were characterised with respect to their morphology, electric charge, and magnetic saturation, crystalline and thermal stability.

## 7.2 Materials and methods

Magnetite particles were synthesised by a surfactant-free, oxidative alkaline hydrolysis process. The ferric and ferrous chlorides ($FeCl_3$/$FeCl_2$) were added in the molar ratio of 2:1 in the liquid. 5.2 g of $FeCl_3$ (BDH Chemicals Ltd.) and 2.0 g of $FeCl_2$ (BDH Chemicals Ltd.) were dissolved in 25 ml double distilled water containing 850 µl of a controlled concentration (1.5 M or 12 M) of HCl (Fisher Scientific). The reaction medium was stirred gently using a magnetic stirrer. The solution was then deoxygenated by bubbling $N_2$ gas for approximately 30 minutes. Following this, the solution was added drop-wise into 250 ml of 1.5 M NaOH (Riedel-de Haën) solution whilst stirring with an overhead impeller. The resulting precipitate was washed three times using double distilled water and was centrifuged at 3260 ×g for 15 minutes to separate it from the solution. Finally, 500 ml of 0.01 M HCl solution was added to the precipitate prior to re-centrifugation at 3260×g for 15 minutes (Kang *et al.*, 1996). A schematic of the process of magnetite production is shown in Figure 7.1:

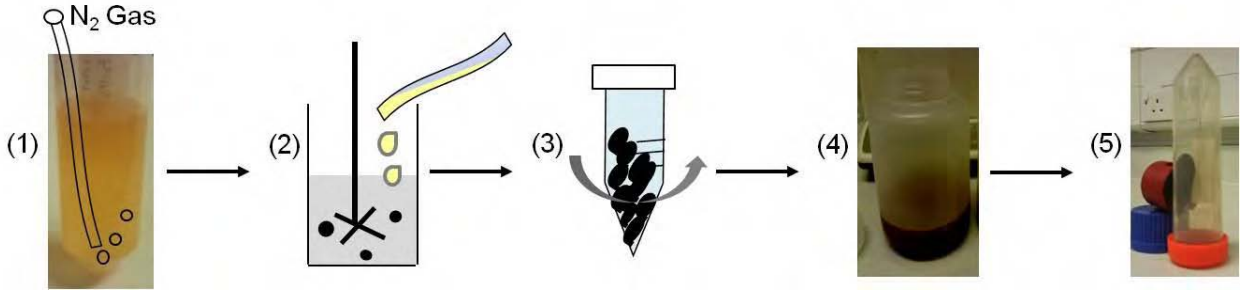


**Figure 7. 1 Schematic diagram illustrating the process of magnetite production by a surfactant-free hydrolysis method. Step (1) deoxygenated by nitrogen gas, (2) drop-wised addition into 1.5 M NaOH under a high-speed mixing, (3) washed and centrifuged 3 times, (4) precipitated and suspension drained prior to freeze-drying and (5) dried magnetite nanoparticles attracted by the attached magnet.**

To determine the influence of $FeCl_3/FeCl_2$ addition and agitation rate on particle size, precipitates were formed using different dropping rates and stirring rates, shown in Table 7.1. Samples A to E were intended to investigate the effects of changing the stirring rates. Samples F to M were prepared for identifying the effects of dropping rates. During particle formation, the hydrolysis step is the key factor that affects product size and crystallinity. Sample N and O were used to observe the size differences resulting from the acid hydrolysis step. Finally, these three controlled variables were combined and modified to synthesize magnetite nanoparticles of ideal size for further work shown as sample P to U. Further details will be illustrated in each section below.

**Table 7.1 List of magnetite samples for different variables.**

| | A | B | C | D | E | F | G | H | I | J | K | L | M |
|---|---|---|---|---|---|---|---|---|---|---|---|---|---|
| Stir ($N_p$) | 2.4 | 2.0 | 1.7 | 1.5 | 1.3 | ( ---------- 1.7 ---------- ) | | | | | | | |
| Drop (ml/sec) | ( ------ 0.44 ------ ) | | | | | 0.48 | 0.46 | 0.39 | 0.36 | 0.34 | 0.28 | 0.20 | 0.18 |
| HCl (N) | ( ------- 1.5 ------- ) | | | | | ( ---------- 1.5 ---------- ) | | | | | | | |

| | N | O | P | Q | R | S | T | U |
|---|---|---|---|---|---|---|---|---|
| Stir ($N_p$) | ( 1.7 ) | | ( ---------- 1.7 ---------- ) | | | | | |
| Drop (ml/sec) | ( 0.44 ) | | 0.44 | 0.40 | 0.36 | 0.32 | 0.28 | 0.24 |
| HCl (N) | 1.5 | 12 | ( ---------- 12 ---------- ) | | | | | |

### 7.2.1 The influence of stirring rate on particle size distribution

In order to obtain consistent mixing conditions, the stirring rates were controlled by an overhead impeller (Heidolph, type: RZR 1) at various speeds from 1700 rpm to 2100 rpm. The particles were produced at five different stirring rates at a constant dropping rate of 0.44 ml/s and measured by dynamic light scattering (HPPS). The stirring rates of sample A, B, C, D and E were 1700, 1800, 1900, 2000 and 2100 rpm, respectively, which are converted separately to a power number, $N_P$, by Formula 7-1 as shown in Table 7.1. In Formula 7-1, P is the power output of the machine; ρ is the fluid density, n is the rotation speed and d is the diameter of impeller. $N_P$ is a dimensionless value indicating the power drawn by the impeller (Green and Perry, 2007)

$$N_P = P/\rho n^3 d^5 = P\,(Watt) \,/\, \rho\ (Kg/m^3)\, n^3\,(rps)\, d^5\,(m) \qquad 7\text{-}1$$

### 7.2.2 The influence of dropping rate on particle size distribution

In this production method, a black precipitate formed when the iron solution was added drop-wise into the alkaline solution with vigorous stirring. The colour change of the solution indicated the formation of magnetite. In order to determine the effects of addition rate, the dropping rates were controlled by a peristaltic pump (Watson-Marlow, type 101U/R) to the values between 0.18 ml/sec and 0.48 ml/sec, as shown in Table 7.1.

### 7.2.3 The influence of acid concentration on particle size distribution

In a precipitation reaction, the nucleation and growth steps are critical in determining the size of the particles. The initial dissolution of the iron complex in acidic medium frees both $Fe^{2+}$ and

$Fe^{3+}$ for further reactions. The concentration of HCl plays an important role in this step (Jolivet *et al*., 1992, Jeong *et al*., 2006). Therefore, to investigate the effects of HCl dissolution, the iron complex was formed in two different HCl concentrations, 1.5 M and 12 M.

## 7.3 Results and Discussion

Magnetite nanoparticles were synthesized by combination of $Fe^{2+}$ and $Fe^{3+}$ solution in various mixing conditions. Then various devices were used for characterization and measurement of the particles. In this section, the influence of mixing conditions and HCl concentration on particle morphology, zeta potential, magnetism and composition are reported.

### 7.3.1 The influence of stirring rate on particle size distribution

Dynamic light scattering was employed to measure the magnetite nanoparticles, all reported values are the mean of five repeats. Figure 7.2 shows the size distribution of hydrodynamic diameter by number percentage for magnetite. To form sample A, B, C, D and E, iron aqueous solutions were dropped into NaOH at a constant speed with five different $N_P$. The results show that magnetite particles distributed mainly in between 98 nm and 167 nm under the initial 1.5 N HCl hydrolysis process. Over all, the five curves of particle size distributions presented by the number percentage, display a relatively narrow range; and show no significant difference in the size range.

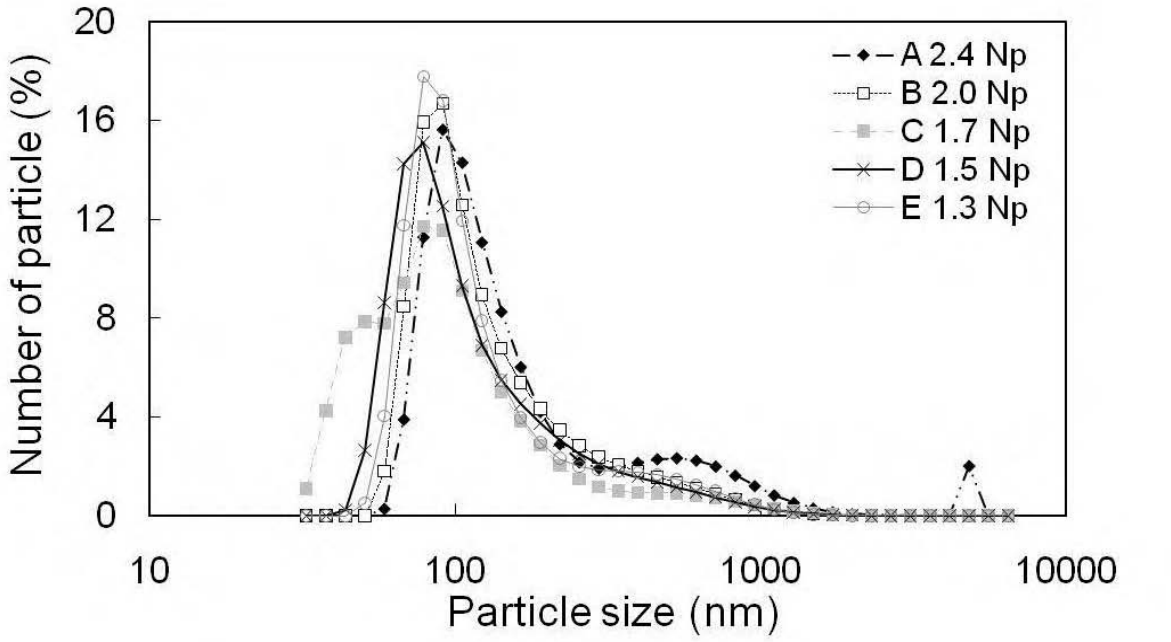


**Figure 7.2 Particle size distributions of magnetite obtained at different $N_P$.**

At different stirring rates, the fluid behaviour can be quantified by their relative power numbers, $N_P$; and Reynolds numbers, $Re_I$ (I indicates mixing by impeller). Table 7.2, presents the mixing conditions and the resultant particle sizes of the five specimens. The $N_P$ of sample A to E are from Table 7.1, Reynolds number ($Re_I$) and power (P) of the mixing conditions were calculated by Formulas 7-1 and 7-2 separately; and the mean size of particle distributions are shown in both intensity and number percentages. Formula 7-1 has been described in detail in section 7-2.1. In Formula 7-2, D is the diameter of impeller, N is the rotation speed, ρ means the liquid density and μ is the liquid viscosity. The $N_P$ of these magnetite fluids were between 1.3 and 2.4; and their $Re_I$ were in the range of $6.9\times10^4$ to $8.5\times10^4$.

Typically, the fluid is in a fully turbulent condition throughout the tank when the $Re_I > 10^4$. Otherwise, there is a wide transition region between laminar flow and turbulent flow, which occurs over the range $10 < Re_I < 10^4$. Turbulent flow is a velocity agitation and is the preferred flow regime for mixing (Green and Perry, 2007). The results of $Re_I$ and power of the stirring conditions have no significant variation; and indicates the fluid behaviours under fully turbulent flows with the five controlled $N_p$.

$$Re_I = D^2 N \rho/\mu = D^2\ (m)\ N\ (rps)\ \rho\ (kg/m^3)\ /\ \mu\ (kg/ms) \qquad 7\text{-}2$$

**Table 7.2 $N_p$, $Re_I$, P and particles size at different mixing conditions.**

| | Stirring rate (rpm) | Power Number ($N_p$) | Reynolds Number ($Re_I$) | Power (W) | Particle Size (nm) Intensity PSD | Number PSD |
|---|---|---|---|---|---|---|
| A | 1700 | 2.4 | $6.9 \times 10^4$ | 18.0 | 527.0 ± 28.4 | 140.0 ± 39.2 |
| B | 1800 | 2.0 | $7.3 \times 10^4$ | 18.0 | 306.0 ± 3.4 | 167.0 ± 6.0 |
| C | 1900 | 1.7 | $7.7 \times 10^4$ | 18.0 | 328.0 ± 5.2 | 97.8 ± 33.7 |
| D | 2000 | 1.5 | $8.1 \times 10^4$ | 18.0 | 297.0 ± 3.4 | 123.0 ± 51.1 |
| E | 2100 | 1.3 | $8.5 \times 10^4$ | 18.0 | 312.0 ± 3.3 | 144.0 ± 27.7 |

Size distributions of magnetite sample A to E are presented in Table 7.2. The mean particle size of sample A to E is varied from 297 nm to 527 nm. Particle size analysis can be demonstrated by different mathematical terms, which are fully explained in section 6.1.1 (Rawle). The particle size shown in the last columns is the mean value of particle size distribution (PSD) basis in number statistics and which is displayed as number PSD. The number PSD of sample A to E is in the

range of 80 % to 100 %, which means 80 % to 100 % of particles in the specimen are in the size value given by the number PSD. The number PSD is used to compare the value of intensity PSD and discuss the particle size distributions. Particle size values for sample A, B, C, D, and E were smaller when calculated by number PSD than when calculated by intensity PSD. The particle size calculated by number PSD were between 98 nm and 144 nm. Overall, the mean values of intensity PSD were almost 2 to 3 times of the mean values of number PSD ($P < 0.001$); it indicates a broad range of particle size dispersion. The polydispersion can be observed from the minor peaks of sample A and C. The other reasons for the differences between the two mathematic schemes will be discussed in following sections.

### 7.3.2 The influence of dropping rate on particle size distribution

The nano-magnetite particles were synthesised at different dropping rates with a 1.5 M HCl solution and with mixing at 2.4 $N_P$. Samples F to I and sample J to M are shown in Figure 7.3 (a) and (b), respectively. Dropping rate had a more significant on particle size distribution as shown in Figure 7.4. The particle size varied from approximately 100 to over 1000 nm; sample G had the smallest particle size of 92 nm and 330 nm in the number PSD and the intensity PSD separately; sample M has biggest size of 1225 nm and 2520 nm in the number PSD and intensity PSD separately. There were 90 to 100% of particles in the size range of the number PSD results of sample F to M. Figure 7.4 indicates a trend of small size fluctuation from changing the dropping rate between 0.34 ml/sec and 0.46 ml/sec (marked by a dashed line), and the same trend exists in both intensity PSD and the number PSD results. Larger particles sizes are seen in the dropping rate over 0.48 ml/sec. and less than 0.28 ml/sec. For samples F to M, the polydispersion

was also showed by the appearance of some minor peaks. In addition, the great differences between the intensity PSD and the number PSD values also refer to the wide range of dispersion ($P < 0.001$).

During the precipitation method, small amounts of iron liquid drop into bulk alkaline under vigorous mixing. The addition of the iron solution of $Fe^{2+}$ and $Fe^{3+}$ into alkaline under high-speed stirring is the key step for the production of magnetite. The particle size distributions show that dropping rates have a stronger influence on particle size than stirring speed. Observations suggest that the addition of the iron solution into the base by a peristaltic pump cause adjacent drops to be fused together when the pump was set at high speed, and the slower dropping speed produced a bigger drop size at the tip of the pipe. Therefore, bigger particles were produced in both high and low speeds of the dropping; this trend can be seen in Figure 7.4. The dropping rates can be controlled by manipulating the conditions such as the efficiency of the pump and the diameter of the pipe used. These factors can be changed and influenced particles size greatly. Alternatively, a rapid injection can be carry out in high temperature solution in a controlled manner to form smaller particle size (Hyeon, 2002).

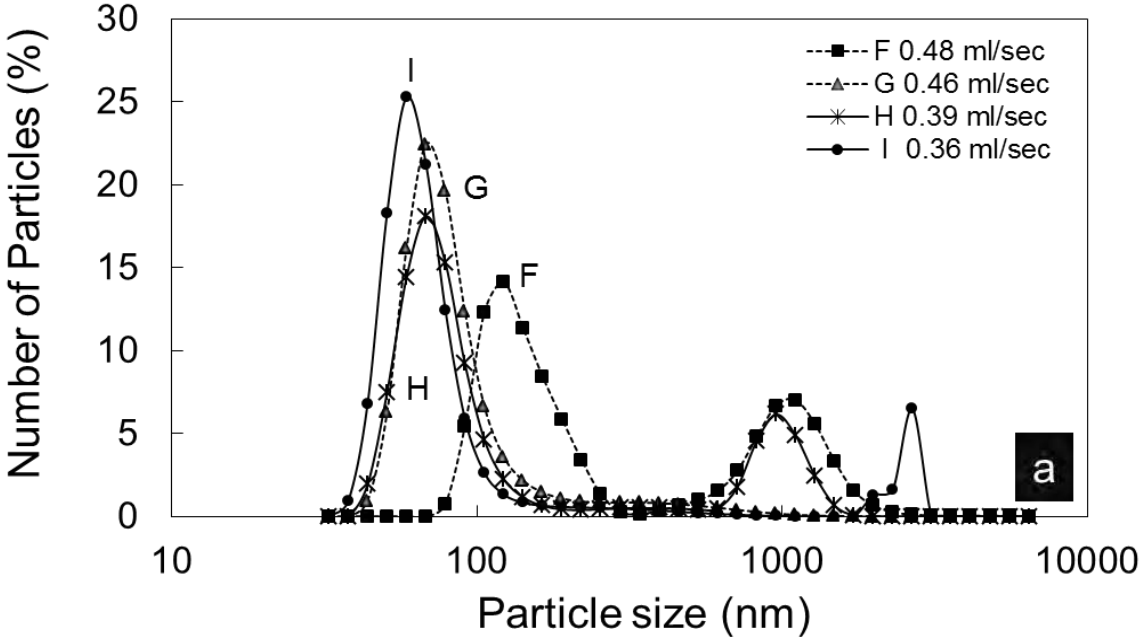


**Figure 7.3 Nano-magnetite particles at different dropping rates presents (a) sample F to I.**

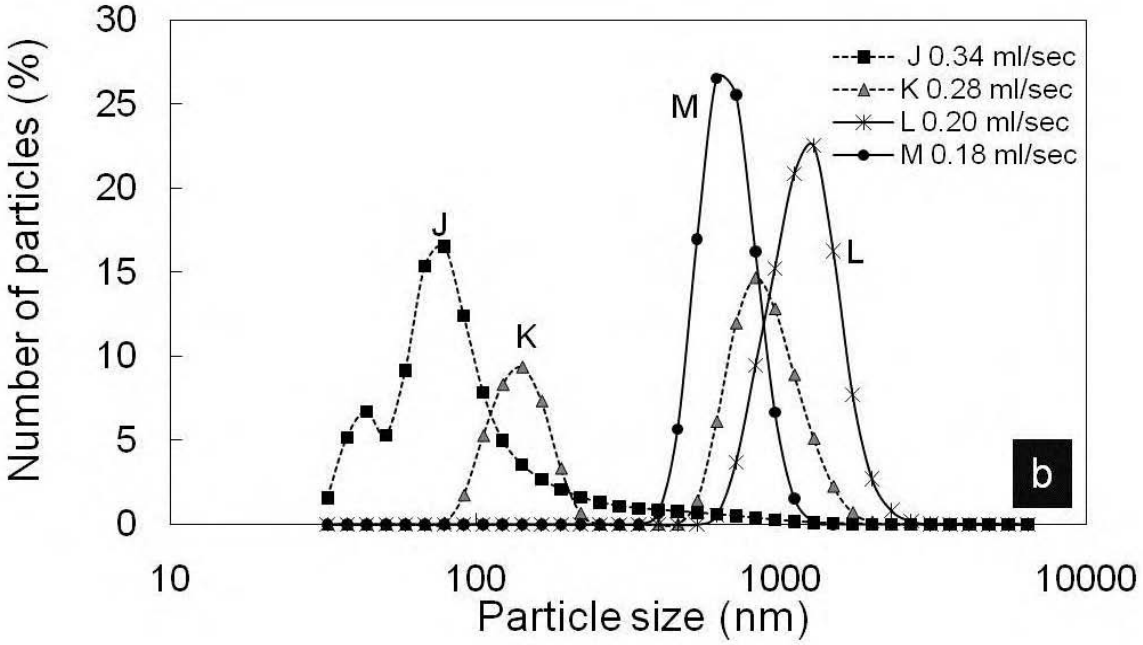


**Figure 7.3 Nanomagnetite particles at different dropping rates presents (b) sample J-M.**

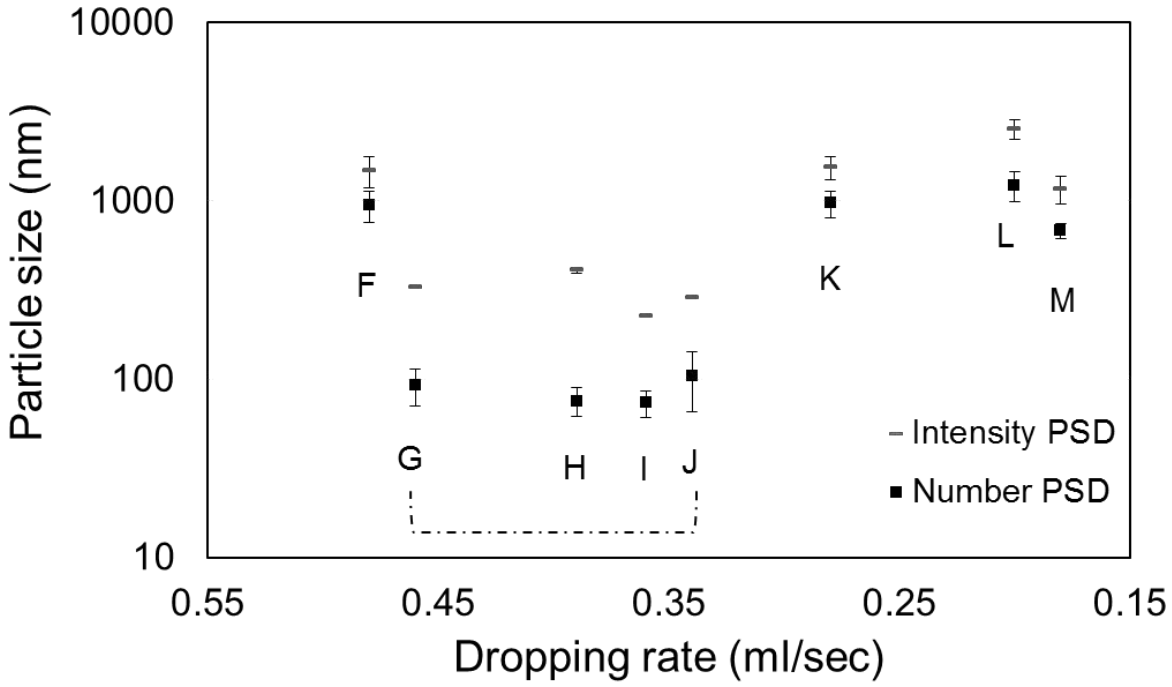


**Figure 7.4 Mean sizes of magnetite nanoparticles at different dropping rates.**

### 7.3.3 The influence of acid concentration on particle size distribution

In addition to mixing conditions, pH values play an important role in particle size distribution and stability (Tombacz *et al*., 2006). Magnetite nanoparticles were produced by a chemical method with acid solvents. At high and low acidic conditions, the size of magnetite can be significantly altered. Magnetite production is under 1.5 M and 12 M HCl, with constant mixing rates (dropped 0.44 ml/sec and stirred 1.7 $N_P$). The majority of particles (over 80 %) of sample N and sample O were distributed in the range of 59 nm to 91 nm and 14 nm to 24 nm, respectively, as the result obtained from the number PSD and show in Figure 7.5. The sizes of magnetite are smaller under a high acid environment and they become larger when the acid concentration is much lower.

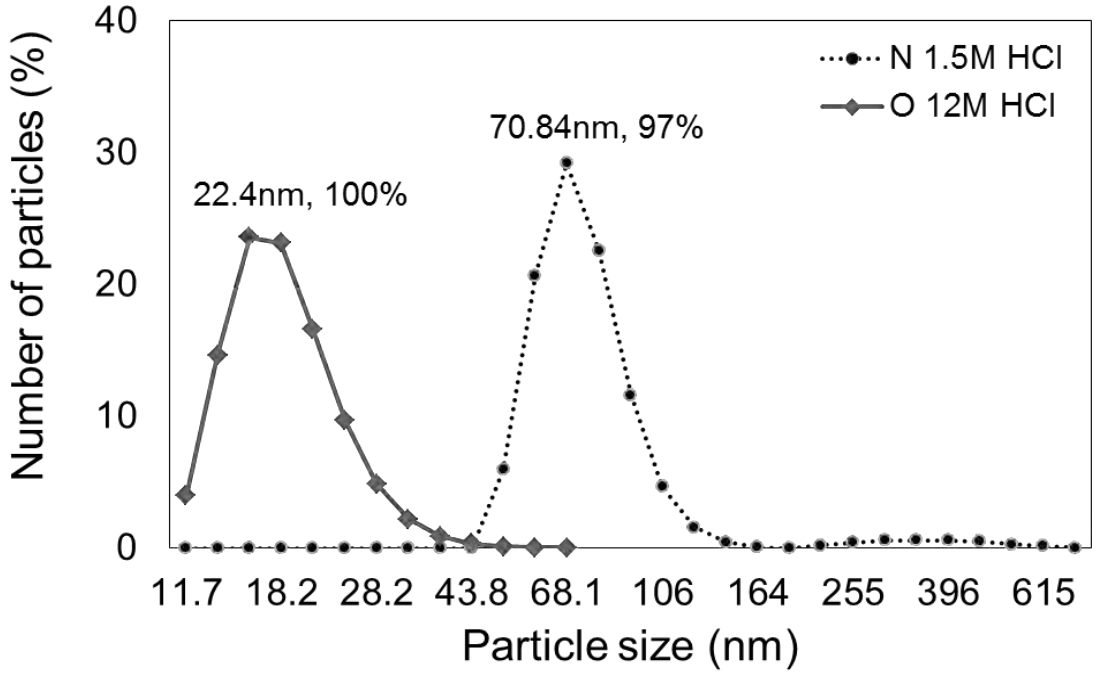


**Figure 7.5 Magnetite nanoparticles distribution under 1.5 M and 12 M HCl by number PSD.**

From the results obtained by light scattering, the particle size can be calculated by intensity, volume and number distribution of the same sample; this results in separate mean sizes. From previous work, aggregation and other certain bigger particles may disturb the results of the intensity PSD. Therefore, determination of both volume and the number statistics can be more accurate for size distribution. In the volume statistics, the minority of large particles may occupy higher ratios of the total results than the majority smaller particles. On the other hand, few big particles may be ignored in a number based calculation if they are less than 1 % of the total amount. The size distribution by the volume PSD is calculated by the mean of particle volume, and it will be disturbed by occasional bigger or smaller sized particles. The size distribution by the number PSD is calculated by the mean of particles number as mentioned in previous section.

Consequently, particle size distribution can be well understood by comparing volume PSD and number PSD. The size distribution from the volume PSD and the number PSD are similar as shown in Figure 7.6 and Table 7.3.

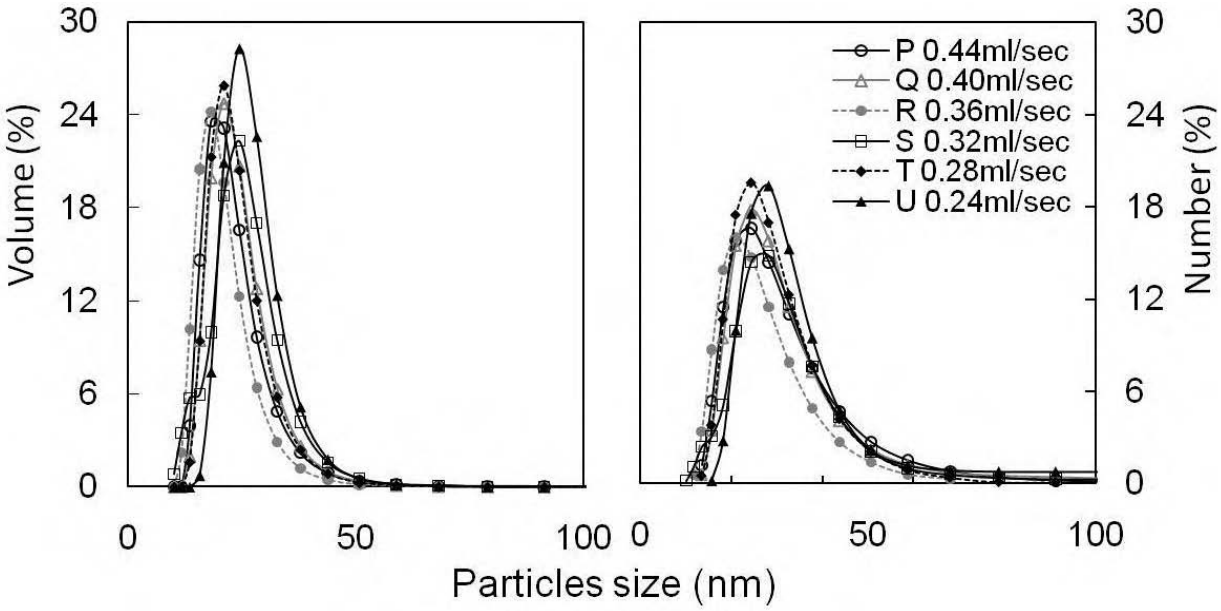


**Figure 7.6 Magnetite nanoparticles distribution under 12 M HCl (a) by number PSD, and (b) by volume PSD.**

**Table 7.3 Size distributions by volume PSD and number PSD of magnetite nanoparticles of Figure 7.6.**

| | Particles size (nm) | |
|---|---|---|
| | (volume PSD) | (number PSD) |
| P | 28.32±1.01 | 21.86±1.22 |
| Q | 28.90±1.64 | 23.00±2.13 |
| R | 24.92±0.96 | 19.84±1.40 |
| S | 29.10±3.93 | 24.00±5.07 |
| T | 27.52±0.87 | 22.72±1.22 |
| U | 31.60±0.70 | 26.42±1.41 |

Compared to Figure 7.3, the sizes of magnetite nanoparticles are smaller and the effects of the dropping rates change are significantly less as the results shown in Figure 7.6. The particle size for the dropping rates (0.18 ml/sec to 0.48 ml/sec) are from 75 nm to over 1000 nm for the lower acid concentration in Figure 7.3, and the range of 12 nm to 59 nm for higher acid concentration in Figure 7.6. The magnetite particles were under the same higher acid hydrolysis step during formulation; the effects from pH on particles size are stronger than from shear. In addition, there was enough acid for the hydrolysis process, and the particles can be synthesized in consistent size and with minimum in size variation, which shows a good agreement with the volume and the number distribution data. The magnetite nanoparticles formed by this method are monodisperse.

The size of magnetite nanoparticles can be affected by several factors, for example the relative oversaturation of solution, the appropriate hydrolysis condition controlling pH value and ionic strength (Tombacz *et al*., 2006). In the initial step of magnetite production, HCl was added to hydrolyse $Fe^{2+}$ and $Fe^{3+}$ salts; and in the final step washing within water and low concentrated HCl. In these two processes, the remaining acid has an effect on the pH value of the final products. Furthermore, before measuring the particle size by light scattering, samples have to dilute. The pH value of the dilution plays an important part in the particles dispersion and aggregation. Indeed, Figure 7.6 illustrates that the effects of pH on the size distribution, which have a greater influence much than the dropping rates shown in Figure 7.3. In addition, Nedkov reported that the sizes of magnetite particles are bigger when the volume of the oxidizing solution (used in the 2nd step for oxidizing $Fe^{2+}$ to $Fe^{3+}$) is increased, and the shape of magnetite passes from spherical through elliptical to cubic. They compared the two most widely quoted co-precipitation processes, with and without oxidizing solution; the results showed that there are

larger grain-size and more crystalline when using oxidizing solution initially and in contrast smaller sized and far worse crystallinity in the absents of the oxidizing solutions (Nedkov *et al*., 2006). The ratios of magnetite particle sizes in our study are similar to that in Nedkov's results, where the concentrations of oxidizing solution were varied. From the above research results, different regime of co-precipitation methods have been investigated; varying particle size and crystallization of magnetite nanoparticles can be put in use depending on different applications.

Another factor influencing the control of the size of the magnetite particles is particle aggregation. Nanoparticles have a large surface area and these results in Van der Waals attractions. As the aggregates become smaller during the de-aggregation, surface force become more important than mass forces and for aggregates smaller than 1 µm, surface force are more than one million times larger than mass force (Kendall and Staiton, 2001). The temperature and pH affects de-aggregation kinetics but do not alter the de-aggregation pattern. Increasing pH value at low temperature could speed up the de-aggregation, whilst increasing pH at high temperature slows down de-aggregation process (Pacek *et al*., 2007). Therefore, the sizes of magnetite obtained at different acid concentrations show diverseness as indicated Figure 7.5.

In addition, magnetite nanoparticles were synthesized through co-precipitation of $Fe^{2+}$ and $Fe^{3+}$ aqueous salt solution and the reaction should be carried out in an oxygen free environment (Gupta and Gupta, 2005) otherwise it is very easy to synthesize by-products, such as maghemite ($Fe_2O_3$). The $Fe_2O_3$ produced is known to interfere with the light scattering results. Passing nitrogen gas is a general method for creating oxygen free environment in the production of nanomagnetite; it not only protects critical oxidation of magnetite but also reduces the particles

size (Gupta and Curtis, 2004). However, the step of bubbling nitrogen gas through the solution is followed by a high speed stirring process for the formation of magnetite nanoparticles. The oxygen in the air would bind and break in the reaction with the iron oxides during the high speed mixing step and interfere with the results of particle size distributions as indicated in Table 7.2.

### 7.3.4 Morphology of nanomagnetite

A TEM image of magnetite is shown in Figure 7.7. Most of the particles are uniform in shape and are relatively small (approximately 10 nm), the dark areas indicate some particle aggregation. The magnetite particles have to be sprayed onto a copper film in liquid phase before TEM observation. The large surface area of nanoparticles result in the Van der waals attractions as mentioned in section 7.2, this is may be the reason of aggregation shown in the TEM image. The average hydrodynamic radii from dynamic light scattering tend to be bigger than those determined from TEM, because of particle aggregation and the angles of three-dimension particles interfering with the signal intensity.

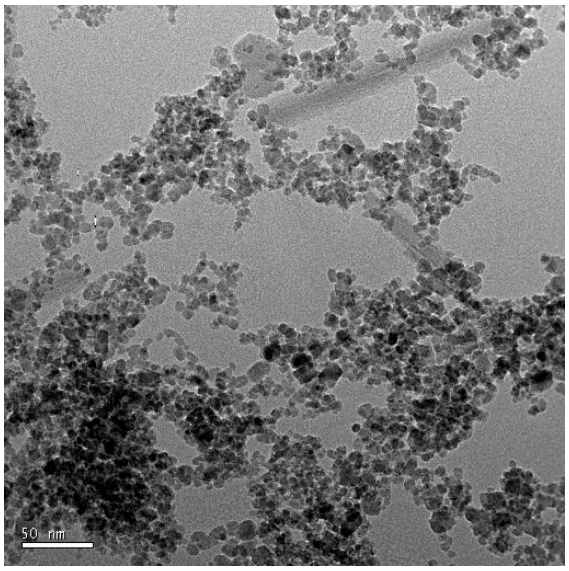


**Figure 7.7 Image of magnetite nanoparticles observed by TEM.**

The aggregation of nanoparticles is one of the main influencing factors of particle size. The image from the TEM result illustrates some darker areas of adjacent particles that aggregated and affects the results of particle size. As the results shown in Figure 7.2 and Table 7.2, the mean particle size of sample A 527 nm, which is obtained from the mean of signal intensity; but the major portion of particles exhibited particles size at 140 nm.

Also, some reports have demonstrated relatively smaller particles compared to this study (Hyeon, 2002; Pacek *et al*., 2007; Tombacz *et al*., 2006; Woo *et al*., 2004; Thapa *et al*., 2004; Matsura *et al*., 2004; Jeong *et al.*, 2006); they produced the magnetite particles under 10 nm by controlling the temperature, surfactants and surface coating. In a study by Hyeon's group, the final precipitate was aged for 30 min at 320 ℃ and dispersed by a surfactant afterwards. The resulting particle size produced were 2 nm in width and 11 nm in length; the length increased from 22 nm to 27 nm by an increasing concentration of surfactant (Hyeon, 2002). We approached the similar

particle size distributions to their work of approximately 18nm by altering the mixing rates while working at room temperature (20 ℃ to 25 ℃) instead of using chemical surfactants and long aging time at high temperature. The high temperature slows down de-aggregation process of nanoparticles in water suspensions (Pacek *et al*., 2007), and surfactants are required for stabilisation and to prevent the adhesion of colloidal particles. Altering mixing speed by controlling the dropping and stirring rates is relatively easy compared to controlling the amount of surfactants and considering the effects of temperature on aggregation.

### 7.3.5 Electric charge of nanomagnetite

The surface properties of magnetite are sensitive to pH variations, which affect the dispersion and coagulation of magnetite nanoparticles. Moreover, the stability of magnetite is also affected by pH value. The transformation of magnetite into maghemite was observed in an acidic environment (Jolivet and Elisabeth, 1988) (Sun *et al*., 1998). The electric charge demonstrated by Zeta potential can be used to characteristic the surfaces of magnetite nanoparticles. The point zero charge (PZC) of magnetite seems to be at pH 7.61 as shown, Table 7.4, and this value falls in the range as reported by Tombacz (Tombacz *et al*., 2006). The Zeta potentials of magnetite particles are negative when the environment in below pH 7.61. For all pH values, the relative narrow width of the peaks indicates that magnetite nanoparticles possess a narrow range of electric charge within the colloid fluid.

**Table 7.4 Zeta potential results shown for three pH values.**

| pH value | KCps | Zeta potential | Width |
|---|---|---|---|
| 7.61, 27.6 ℃ | 306.7 ± 50.1 | 0 ± 0 | 0 ± 0 |
| 7.14, 25.8 ℃ | 5347.0 ± 65.0 | -4.1 ± 0.8 | 6.9 ± 1.6 |
| 6.82, 24.6 ℃ | 2423.6 ± 34.1 | -12.2 ± 2.6 | 6.4 ± 0.0 |

### 7.3.6 Crystalline composition of nanomagnetite

The crystalline composition of the synthesized magnetite nanoparticles were determined using XRD (Figure 7.8). The result shows that the crystalline is most close to the $Fe_3O_4$ phase and indicates a monophase of the nanoparticles. The intensity of the peaks in the five characteristic peaks display at 2θ of 30.1, 35.5, 43.2, 57.0 and 62.8 degree, which corresponded to indices of 220, 311, 400, 511 and 440 respectively of magnetite (Hong *et al*., 2007). The diffraction patterns of maghemite, the most likely side product of magnetite formulation, are absent. Furthermore, the crystalline of magnetite is cubic structure indexed by XRD analysis. Superparamagnetism are exhibited in small (less than 100 nm) and single domain magnetic particles (Ma *et al*., 2004); therefore, the results of XRD and SQUID present the agreement of that the magnetite nanoparticles are of a single domain and exhibit superparamagnetism. Understanding the magnetism and crystalline purity is useful for defining the mechanism of heat generating by magnetite particle in chapter 9.

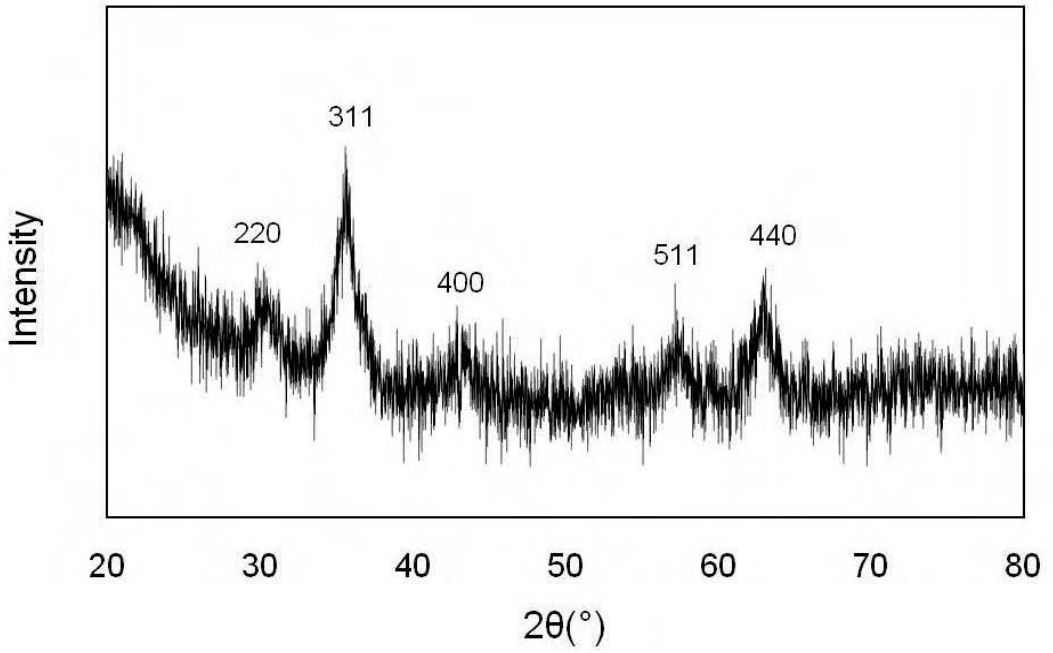


**Figure 7.8 X-ray diffraction patterns of magnetite nanoparticles.**

### 7.3.7 Magnetic saturation of nanomagnetite

The magnetic nature of the precipitation was confirmed using a rare earth magnet. Attaching a magnet at one side of the sample container, and the particles were attracted to the side with the magnet after a period of 1 hour. Figure 7.9 illustrates the Ferro-fluid from brown colour to clean by magnet attachment. Statistic magnetisation of magnetite nanoparticles were measured by superconducting quantum interference device (SQUID) in two experiments: at three steady temperatures (5 K, 300 K and 350 K) with varying magnetic field strengths and a steady magnetic field with temperatures sweep in the field. SQUID results shown in Figure 7.10 and Figure 7.11, the magnetisation curves are similar for magnetite particles while in 5 K, 300 K and 350 K measurements. Afterwards, the magnetite was placed in a 1000 Oe magnetic field for measurement with changing temperature.

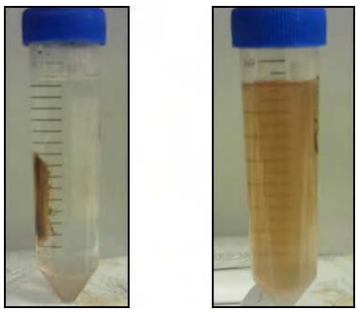

**Figure 7.9 Magnetization of magnetite nanoparticles by magnet attraction.**

The hysteresis curves of Figure 7.10 indicates superparamagnetic behaviour resulting from the coercivity and remanence values are not discernible at 5 K ,300 K and 350 K (Woo *et al*., 2004) (Hong *et al*., 2007). Furthermore, the magnetisation of magnetite nanoparticles decreased after heating by 90 K and keeping steady in a low magnetization state after the temperature reaches higher than approximately 270 K, shown in Figure 7.11. The decreases of magnetic saturation from 5 K to 300 K are less than 2 emu/g. The loss of magnetisation is comparatively low if it is taken into the nanoscale (Banert and Peuker, 2006). The magnetite particles produced by the non-surfactant method have superparamagnetic behaviour.

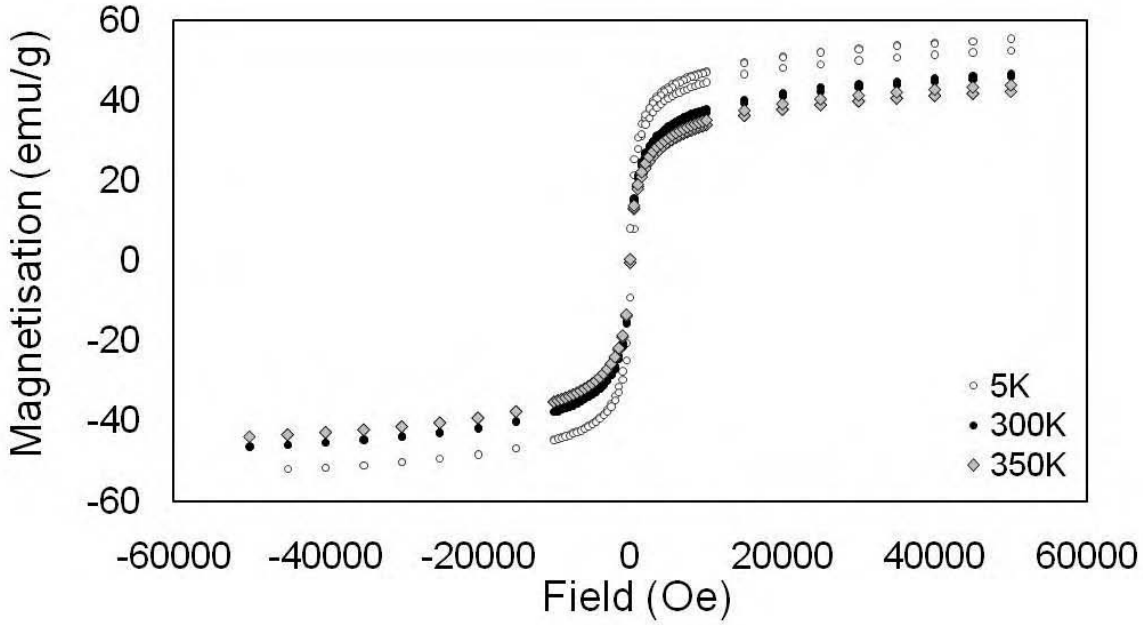


**Figure 7.10 Magnetization at three temperatures (5 K, 300 K and 350 K) with different magnetic field sweep by SQUID.**

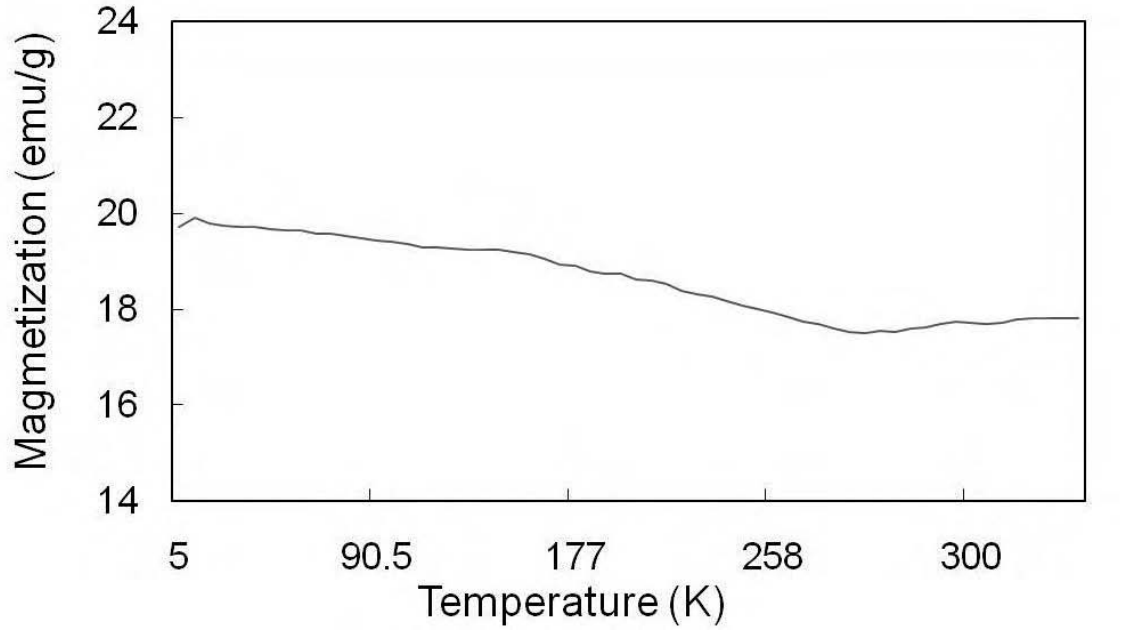


**Figure 7.11 Magnetization in 1000 Oe field strength and different magnetic temperature sweep.**

### 7.3.8 Thermal stability of nanomagnetite

Figure 7.12 show the DSC results of magnetite nanoparticles. There were three repeats for DSC measurements. According to the endothermic and exothermic curves, there is no obviously heat capacity change and phase transition occurring during either heating or cooling between 25 ℃ and 200 ℃. This indicates good stability of magnetite nanoparticles.

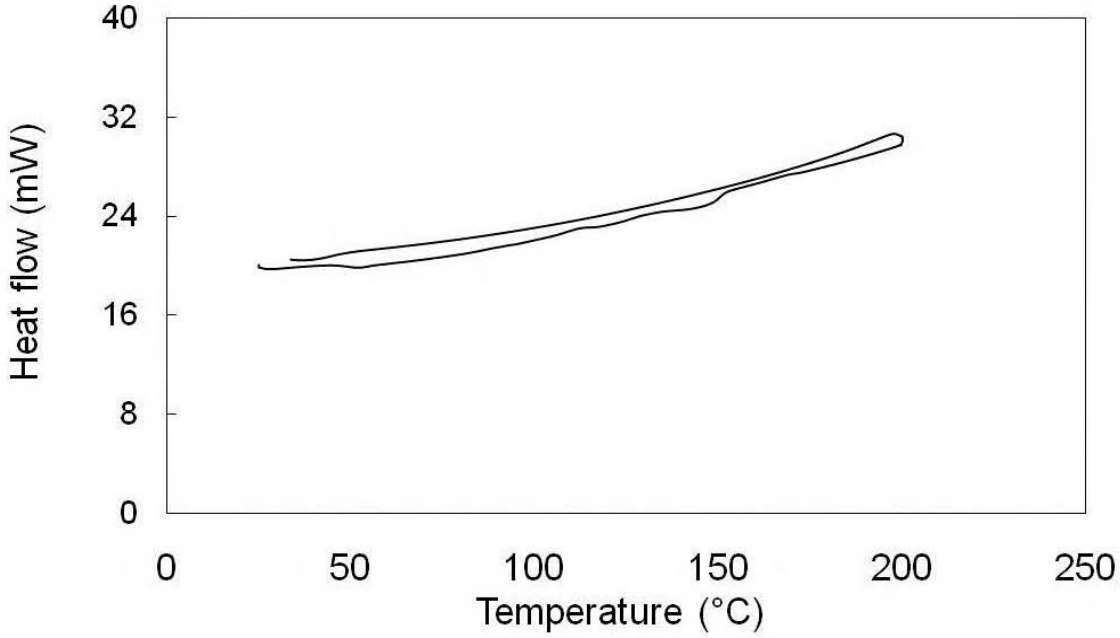


**Figure 7.12 Thermal analysis result of magnetite.**

## 7.4 Conclusion

Particle size control of magnetite nanoparticles can be accomplished by the co-precipitation method with various mixing speeds and acidic values. Formulation with different dropping rates indicated a trend of small size fluctuation from 0.35 ml/sec to 0.46 ml/sec. The pH value of the dilutions displayed a key factor of influencing particle size. A high acid environment enabled de-aggregation and good dispersion of the resultant magnetite nanoparticles. Both the number and the volume data demonstrated similar size distribution of magnetite nanoparticles synthesized with 12 M HCl hydrolysis. The magnetite nanoparticles in this thesis were formed in the room temperature without any heating procedures and chemical modification during the formulation, achieved great results of size-control, monophased and superparamagnetism at 5 K, 300 K and 350 K.

The magnetite nanoparticles formed in the identical conditions was engaged to the production of MP microspheres and further works.

# Chapter 8 Formulation and characterization of PCL and MP microspheres

## 8.1 Introduction

Biocompatible polymers have attracted a lot of interest for the production of biomaterials for implantation. As one of the most commonly used polyesters, PCL has been widely applied in the formation of different types of biomaterials; such as PCL based scaffolds for tissue engineering and PCL/hydroxyapatite composite for bone replacement (Ural *et al*., 2000; Boccaccini *et al*., 2010). The objective of the work reported in this chapter is to synthesize and characterize magnetite/PCL (MP) microspheres. In order to obtain ideal formulation conditions, PCL microspheres were formulated by emulsion at different speeds, and the size distribution and morphology of PCL particles were discussed. Thereafter, MP microspheres were synthesized using the magnetite nanoparticles under the identical condition from previous work (chapter 7), and the characterisation of MP particles was defined.

The results section reported the influence of changing mixing speed on size distribution of PCL microspheres and the physiochemical analysis of PCL and MP spheres. The property determinations of the resultant microspheres include morphologies and distribution of magnetite from sections. MP spheres were also characterised with respect to their composition and magnetisation and thermal properties.

## 8.2 Material and Method

Two different types of PCL, CAPA® 6100 and CAPA® 2201 (Perstorp, UK Ltd.), were chosen for the production of microspheres. Table 8.1 shows the general product description of the two types of PCL, the mean molecular weights were 10,000 and 2000. The melting points were 58 ℃ to 60 ℃ and 40 ℃ to 50 ℃, and the viscosities were 9300 mPa.s and 480 mPa.s, respectively. PCL CAPA® 6100, described as PCL6, is a linear polyester with high molecular weight derived from the caprolactone monomer. CAPA@ 2201, known as PCL2, is a standard grade linear polyester diol derived from caprolactone monomer terminated by primary hydroxyl groups, and is waxy in texture.

**Table 8.1 General product description of the PCL used in this thesis.**

| PCL | MMW | Melting Point | Viscosity | Physical Form |
|---|---|---|---|---|
| CAPA@ 6100 | 10,000 | 58-60 ℃ | 9300 mPa.s, at 100 ℃ | White Solid |
| CAPA@ 2201 | 2,000 | 40-50 ℃ | 480 mPa.s, at 60 ℃ | White Waxy Solid |

### 8.2.1 Formulation of PCL microspheres

The microspheres were prepared using an emulsion solvent extraction/evaporation technique (Perez *et al*., 2000). 300 mg of PCL was dissolved in 10 ml of dichloromethane (Sigma-Aldrich) during 1-minute of sonication. Subsequently the PCL solution was emulsified into 100 ml of 2 % w/v aqueous poly-vinyl alcohol (PVA) (Sigma-Aldrich) solution utilising a high speed blender (SILVERSON, machine serial No. V5100), using a high-speed emulsion rate for 3 minutes. The

emulsion was then gently agitated by a shaker at 200 rpm and 20 ℃ with addition of 50ml of distilled water for 3 h until the dichloromethane had completely evaporated. The emulsion was then centrifuged at 204 ×g for 5 minutes and washed with double distilled water three times before freeze drying (Barbato *et al*., 2001). The formulation of MP particles is roughly the same as the production of PCL microsphere. The process of PCL production is shown below, Figure 8.1.

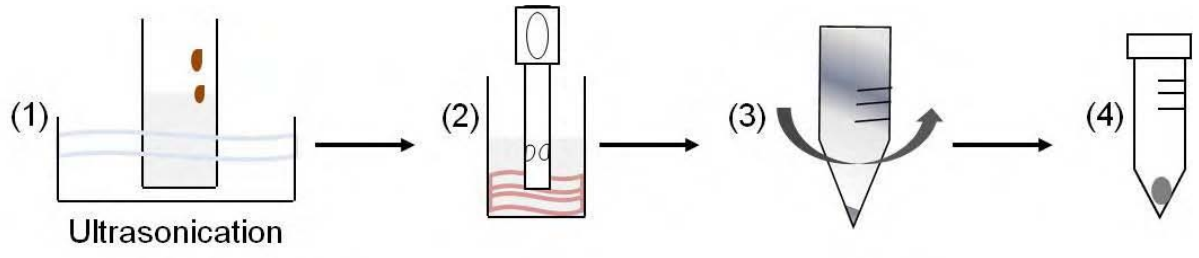


**Figure 8.1 Schematic illustrating the formulation of PCL and MP microspheres by an emulsion solvent evaporation technique. Step (1) dissolved PCL and magnetite mixing by ultra-sonication, (2) added into 2 % PVA solution at a high-speed emulsification, (3) agitated and centrifuged, (4) precipitated and suspension drained before freeze-drying.**

## 8.2.2 The influence of changing mixing speed on size distribution of PCL

The influence for PCL addition rate on particle size was determined by forming precipitates at different emulsification speeds, 6000, 5000, 4000 and 3000 rpm. To determine the flow behaviour during the emulsification process, the mixing speeds were converted to $N_P$ and Re, respectively (Formula 7-1, 7-2).

### 8.2.3 Formulation of MP microspheres

The optimum conditions for PCL and magnetite production were selected for preparing MP microspheres. The first step was the same as the preparation of PCL (as described in section 8.2.1); 300 mg of PCL was dissolved in 10 ml dichloromethane (Sigma-Aldrich) under gentle agitation. Different acquired amounts of magnetite particles were added into the PCL solution during sonication. Subsequently, the PCL and magnetite solution was emulsified into 100 ml of 2 % w/v aqueous poly-vinyl alcohol (PVA) solution utilising a high-speed blender at a high blending rate, 6000 rpm, for 3 minutes. The magnetite and PCL emulsion was gently agitated by a shaker at 200 rpm at 20℃ with the addition of 50 ml of distilled water for 3 hours until the dichloromethane had completely evaporated. After that, the emulsion was centrifuged at 204 ×g for 5 minutes and washed with double distilled water three times before freeze drying.

## 8.3 Results and Discussion

Magnetite encapsulated PCL was synthesized after the separate production of nanoscale magnetite and PCL particles. Different devices for the characterizations of the particles were used. Firstly, particles size distribution of all mixing rates. Then, the particle morphologies and compositions were determined. Following the production and characterisations of PCL microspheres, MP microspheres were synthesized and were exposed to thermal treatments and drug release investigations.

### 8.3.1 The influence of changing mixing speed on size distribution of PCL

Size-controlled studies are presented for both PCL2 and PCL6. The PCL2 microspheres, included samples A, B, C, and D prepared by using a homogenizer at 6000, 5000, 4000 and 3000 rpm respectively. Similarly, PCL6 microspheres, included samples E, F, G, and H, which were prepared at 6000, 5000, 4000 and 3000 rpm, respectively. The particle distributions of the PCL microspheres were determined by using light scattering at room temperature. The particle size distributions (PSD) of the PCL samples were obtained by solvent evaporation method shown on Figure 8.2 and Figure 8.3. The resultant data was present in volume statistics by the light scattering. The results of A to H are from the mass median diameter ($d_{0.5}$) of particles distribution.

The results in Figure 8.2 indicate that the size distributions of PCL2 fluctuated across the four mixing speeds. For PCL2 particles, there is no significant relationship between mixing speeds and resultant particle size. PCL2 particles were distributed between 14.7 μm and 55.6 μm ($P < 0.001$). As seen in Figure 8.3, particle growth was found to be greater when the mixing speed was slower. The PCL6 particle size was slightly lower than PCL2, ranging from 43.6 μm to 4.4 μm when the mixing speed rose from 3000 rpm to 6000 rpm. It can be seen that when the mixing rate was reduced to 3000rpm, the size range was almost 10 times larger than the smallest sample, E ($P < 0.001$). In addition, the flow behaviours and mixing efficiencies can be seen in $N_P$ and Re, in Table 8.2.

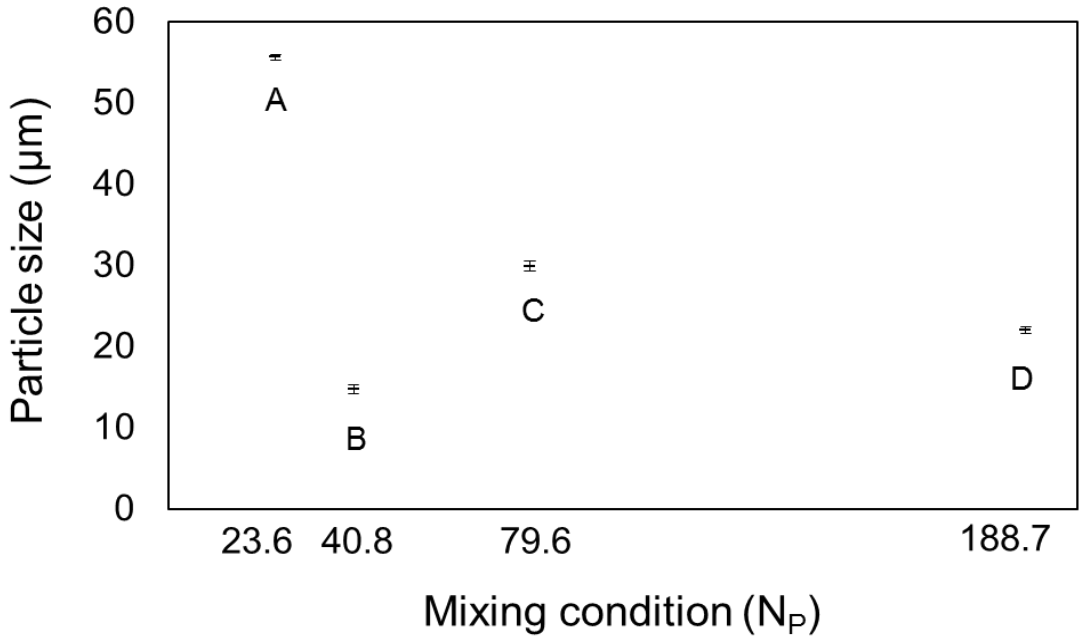


**Figure 8.2 PSD of PCL2 microspheres ($d_{0.5}$) by varying mixing rates.**

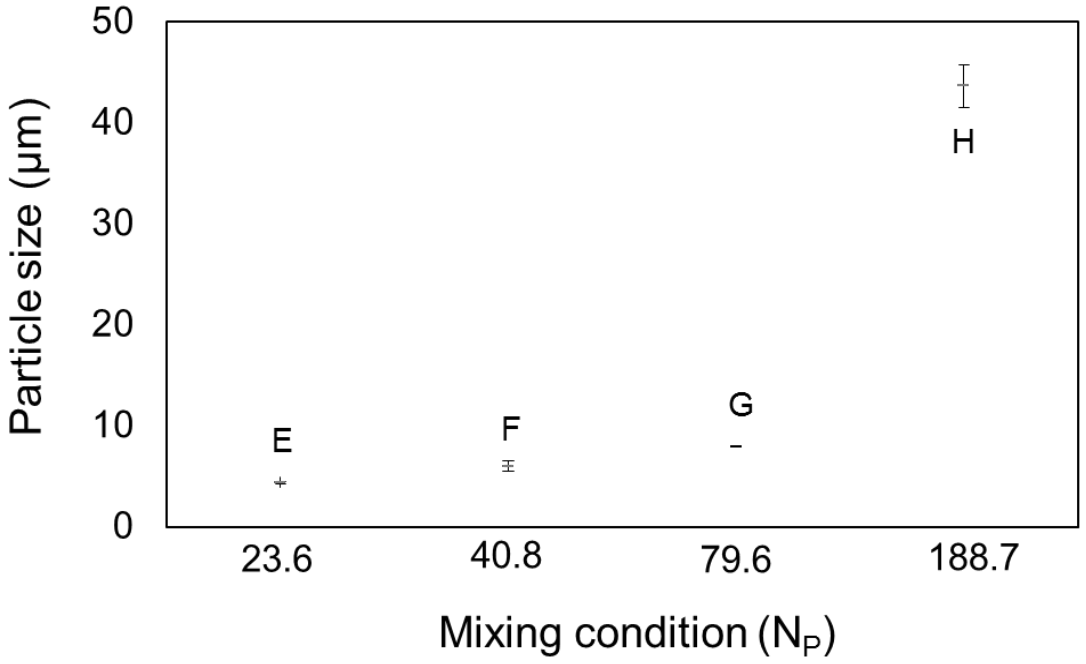


**Figure 8.3 PSD of PCL6 microspheres ($d_{0.5}$) by varying mixing rates.**

**Table 8.2 Particle size distributions of the two types of PCL microspheres at different mixing speeds (3000 rpm to 6000 rpm).**

| Mixing speed (rpm) | | 6000 | | | | 5000 | | | | 4000 | | | | 3000 | | | |
|---|---|---|---|---|---|---|---|---|---|---|---|---|---|---|---|---|---|
| $N_P$ | | 23.6 | | | | 40.8 | | | | 79.6 | | | | 188.7 | | | |
| Re | | $71.8\times10^4$ | | | | $59.8\times10^4$ | | | | $47.9\times10^4$ | | | | $35.9\times10^4$ | | | |
| | | $d_{0.1}$ | $d_{0.5}$ | $d_{0.9}$ | $S^*$ | $d_{0.1}$ | $d_{0.5}$ | $d_{0.9}$ | $S^*$ | $d_{0.1}$ | $d_{0.5}$ | $d_{0.9}$ | $S^*$ | $d_{0.1}$ | $d_{0.5}$ | $d_{0.9}$ | $S^*$ |
| size (μm) | PCL2 | 7 | 56 | 143 | 2 | 4 | 15 | 73 | 5 | 7 | 30 | 101 | 3 | 4 | 22 | 62 | 3 |
| | PCL6 | 1 | 4 | 74 | 17 | 1 | 6 | 52 | 9 | 3 | 8 | 38 | 4 | 12 | 44 | 184 | 4 |

$S^*$: Span = $(d_{0.9}-d_{0.1})/d_{0.5}$; n=3

In Table 8.2, $N_P$ and Re were obtained from Formula 7-1 and 7-2 (Green and Perry, 2007). The power number was between 23.6 and 188.7 for this range of mixing. Re values are over $10^4$, which is in the range indicating fully turbulent flow as discussed in chapter 7. The $N_P$ of the flow increased irregularly as the mixing speed decreased from 6000 rpm to 3000 rpm. Notably, the $N_P$ was higher than doubled when the speed was reduced from 4000 rpm to 3000 rpm. The size distributions of PCL2 and PCL6 microspheres were illustrated by $d_{0.1}$, $d_{0.5}$ and $d_{0.9}$, and the width of distributions were converted and reported in the values, span. Each value was obtained from three repeats of every sample (n =3). The particles sizes of PCL6 have relative smaller particle size under high speed mixing ($P \leq 0.3$), but increase significantly at lowest speeds, of 3000 rpm. The size distributions of PCL2 microspheres did not show a strong relationship with emulsion methods, but the smallest size distribution also exhibited at higher speed mixing, 5000 rpm. However, the span values varied from 2 to 17 while PCL2 and PCL6 microspheres were formed

at the four mixing speeds, which indicated the polydisplersion of the resultant microspheres (Malvern Ltd., UK).

As mentioned in chapter 7, $N_P$ is the dimensionless value of power drawn by impeller. Theoretically, the power generated by the machine is 18W; however, it may be varied by different flow conditions, such as viscosity of fluid and mixing speed. Consequently, flow behaviour and flow efficiency are indentified by discussion of $N_P$ and Re. Form the Formula 7-1, the relationship between $N_P$ and power is an inverse relationship. According to the resultant size distribution of PCL6, $N_P$ exhibited effects on particles size. On the other hand, particles size of PCL2 did not show significant dependence on the variation of $N_P$. Nevertheless, the smallest particles of PCL2 and PCL6 are both displayed when lower $N_P$ is using (40.8 and 23.6 respectively).

The other factor effecting the size distribution of PCL particles is the stabilisers used during PCL formulation. A report that the preparation of PCL microparticles with different stabilizers indicated that depending on the different stabilizer used, different particle size, particle size distribution and morphology of microparticles could be produced. Authors suggested that the use of gelatine as a stabilizer for PCL gives a narrow particle size distribution and more uniform particles. The hydrogen bond of gelatine balances the hydrophilic/hydrophobic effect in the emulsion system. According to their results, which compared the ability of gelatine and PVA to act as stabiliser, gelatine is effective at preventing aggregation of the emulsion microdroplets, whereas PVA is more hydrophilic and could not effectively protect the emulsion microdroplets

from coagulation (Chen *et al*., 2000). Therefore, the polydispersion of PCL microspheres could be attributed to the using of PVA.

### 8.3.2 Morphology of PCL microspheres

The images of two types of PCL made at a $N_P$ of 23.6 were captured by ESEM as shown in Figure 8.4 and Figure 8.5. In Figure 8.4, a collection of PCL2 particles is present at (a) and (b), while (c) is a single particle of PCL2. PCL6 particles shown in Figure 8.5, (a) are collections of particles which are zoomed in to the single P6 particle in (b). Both PCL6 and PCL2 are spherical in shape and well dispersed. The PCL6 particles are approximately 4 μm in diameter under 23.6 $N_P$ mixing process, which refers to the results in Table 8.3.

On the other hand, images of collections and single PCL2 particles are all much smaller than the results from light scattering; they are approximately 4 μm to 10 μm according to the particle sizes in Figure 8.4. In Figure 8.4 (b), the micrograph shows the wide dispersion of PCL2 sizes, which may explain the results given by light scattering. The data were obtained from volume statistics, a larger particle occupied higher volume than a smaller particle; therefore, the resultant sizes tend to be bigger than actual particle shown by ESEM. Moreover, some particles did not disperse properly and were actually bound to each other as seen in Figure 8.4 (b); this may result from the waxy property of PCL2 and lead to increased size values due to the fusion of particles. The other factor leading to polydispersity or aggregation is the concentration and viscosity of stabilizer. Increasing the PVA concentration resulted in smaller and uniform droplet size and leading to the formation of low polydispersity (Sahoo *et al*., 2002; Zambaux *et al*., 1998)

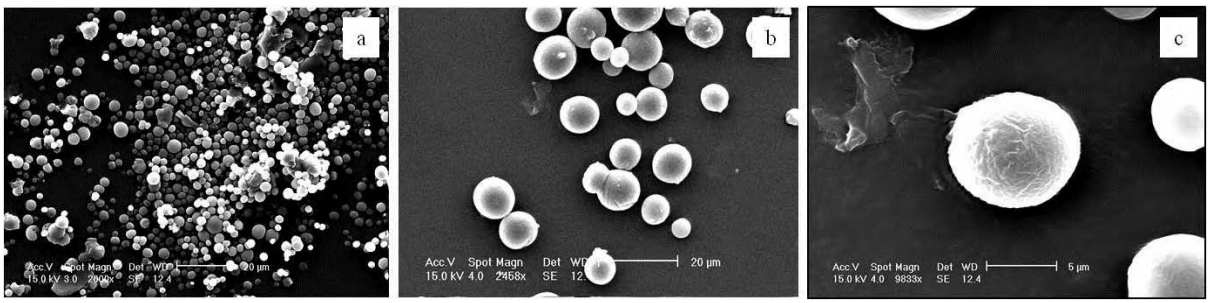


**Figure 8.4 Micrographs of PCL2 microspheres: (a) and (b) are the collection of microspheres and (c) is the single domain.**

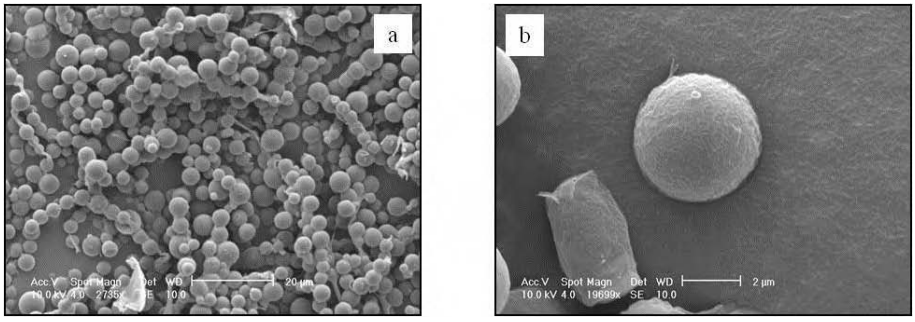


**Figure 8.5 Micrographs of PCL6 microspheres: (a) is the collection of microspheres and (b) is the single domain.**

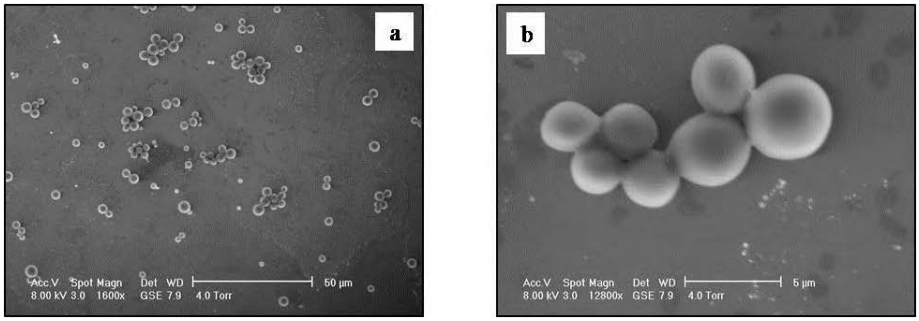


**Figure 8.6 Micrographs of PCL microspheres at wet condition (a) and magnification into (b).**

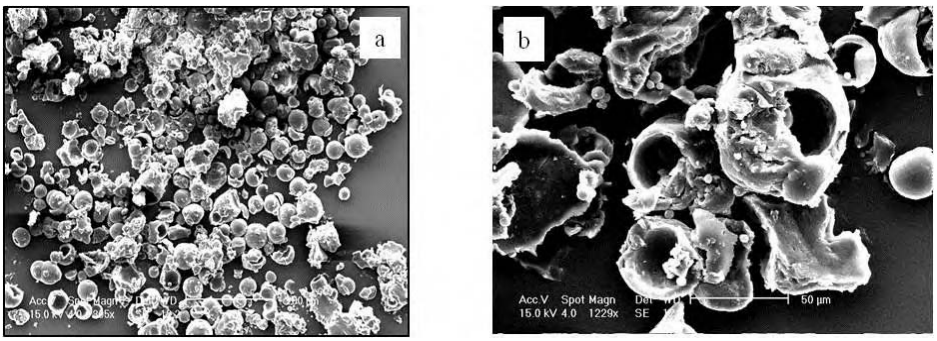


**Figure 8.7 Micrographs of PCL microspheres crushed by a toothpick on the stub (a) and magnification into (b).**

PCL particles displayed spherical shapes when in the dry storage condition as previous images showed, and PCL were also observed at wet and broken conditions. PCL6 particles were stored in distilled water and captured by ESEM as shown in Figure 8.6. Some of the particles showed aggregation with nearby PCL, as displayed in Figure 8.6 (a). The surfaces of PCL here are smoother than in dry conditions and exhibit a slight swelling from absorbing the surrounding moisture in (b). Technically, the surfaces of PCL particles are hydrophobic and less able to interact with water. Sahoo and colleagues reported that the residential PVA may affect the physical properties of polymer. In their report, there is an increase of the association between residual PVA and nanoparticles when the solvent miscibility with water is relative high. The miscibility of dichloromethane in water is relative high compared to other organic solvent in their work. Therefore, more PVA might intrude into the polymer phase and result in more miscibility with the aqueous phase (Sahoo *et al*., 2002).

PCL2 encapsulated magnetite (MP2) microspheres were crushed by a toothpick to observe the morphology of broken particles. Under ESEM observation, parts of MP2 particles are still intact

and spherical as shown in previous ESEM result, and some of the samples exhibit the expected breaches and fractures after cracking in Figure 8.7 (a) and magnification, (b). From the broken particles, the inner shells demonstrated regular hollow structures. The thickness of the shells of the PCL microspheres was around 1/10 to 1/8 the diameter of the spheres (measured by Image-J software). The swelling of the PCL in water (shown in Figure 8.6) was less than 1/5 (2 x 1/10) of the diameter of the original spheres and could be attributed to the residual of PVA on the surface of the spheres.

### 8.3.3Morphology and property analysis of MP microspheres

From section 8.2.1, power number is more stable at higher mixing speeds and PCL6 particles are relatively smaller at 23.6 $N_P$ mixing condition by homogenizer, which offers a relatively larger surface area for other applications. Consequently, the mixing condition, 6000 rpm with $N_P$ at 23.6, was chosen for MP formulation. Property analysis was undertaken following particle formation and morphology observation. Characterisations of MP microspheres were performed with an ESEM connected to an Energy Dispersive Spectrometer (EDS) are shown in Figure 8.8 and Table 8.3. The morphologies of MP2 and MP6 are displayed in Figure 8.8 (a) and (b). According to the results, MP2 and MP6 particles are well dispersed and stable in spherical shape. In Figure 8.8 (c), shows disruption on the particle surface when in a dry environment, which corresponds to the ESEM results.

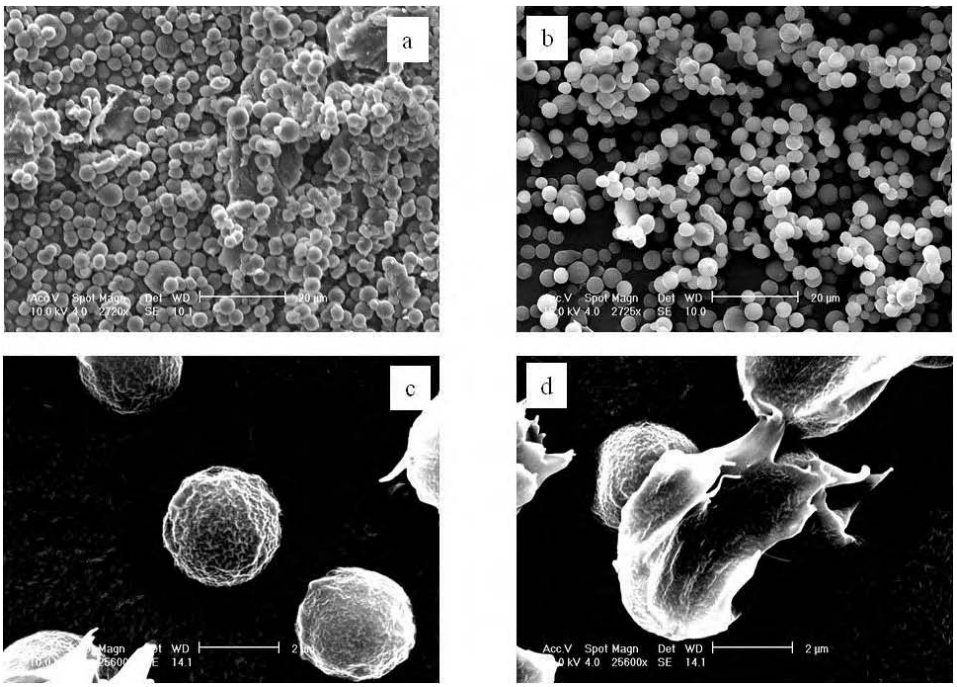


**Figure 8.8 Micrographs of (a) MP2, (b) MP6, (c) surface and (d) inner shell.**

**Table 8.3 Contents of MP particles observed by EDS analysis.**

| | C | O | Fe | Total Weight % |
|---|---|---|---|---|
| Spectrum 1 (c) | 89.3 | 10.7 | 0 | 100 |
| Spectrum 2 (d) | 91.7 | 7.6 | 0.7 | 100 |

MP6 was also crushed in Figure 8.8 (d) in order to collect spectra from the inner surface. The results show that there was no iron on the surface of MP particles in (c), but 0.7 % on the inner shell of the sample in (d). According to the EDS results, the majority of magnetite nanoparticles were assumed to be encapsulated inside PCL microspheres and only a small amount of magnetite appeared on the surfaces of the microspheres. In a report by Hamoudeh and Fessi, PCL-magnetite microparticles were formed by an emulsion evaporation method, similar to the formulation used

in this investigation, which confirmed the encapsulation of magnetite within PCL (Hamoudeh and Fessi, 2006). However, the elemental analysis by EDS is not quantitatively precise for element concentration especially elements with low atomic numbers (Buck *et al*., 2004). The electron beam was manually localized on the target area within the range of view reached from ESEM (Kutchko and Kim, 2006). Therefore, EDS can be used to identify the existence of the elements by presenting the peaks of different intensities, but the concentrations of elements should be confirmed by another means. Table 8.3, the EDS results show the success of magnetite encapsulation within PCL, and the spherical shape of PCL particles did not present a significant change in appearance following encapsulation work with magnetite, as shown by ESEM images.

After the elemental identification, schematic illustrations of MP particles are presented by cross-sections and the images were captured by TEM as shown in Figure 8.9. The micrographs illustrated that the magnetite nanoparticles were encapsulated within MP. MP particles are hollow in shape as shown in Figure 8. 8. Hollow shaped particles were crushed and some parts of the particle were squeezed to one side during the procedure of cutting. In the micrograph, (a) is MP2 and (b) is MP6 single particles captured by TEM. MP2 and MP6 became oval-shaped due to the pressure applied during crushing. The magnetite dispersion in the shell of PCL is clearer in (b); individual magnetite nanoparticles can be seen and were surrounded by PCL shell shown as light grey matrix. This is evidence that the magnetite nanoparticles were encapsulated inside PCL microspheres.

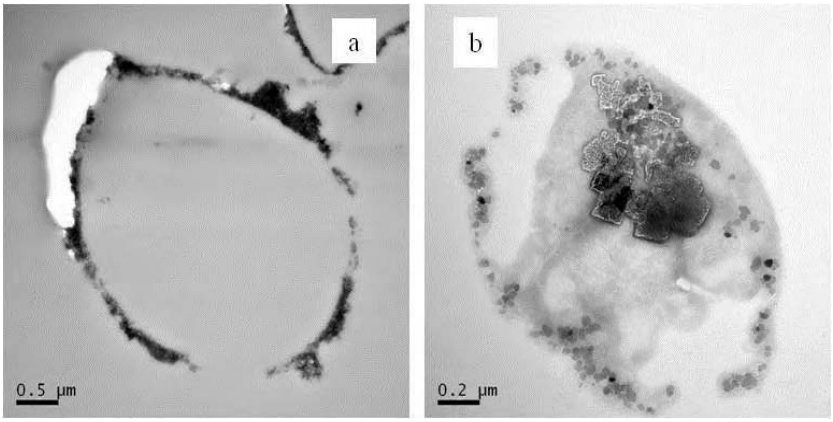


**Figure 8.9 Transmission electron microscope of cross section through (a) MP2 and (b) MP6.**

The encapsulation of magnetite with PCL was further confirmed by FTIR measurements. To compare the differences of IR spectra between MP and PCL, the FTIR results of MP and PCL are shown in (a) and (b) separately in Figure 8.10. As shown in the results, the low frequency IR spectra, at 400 $cm^{-1}$ to 1000 $cm^{-1}$, suggested the presence of magnetite due to the iron oxide structure (Yang *et al*., 2006). As the arrow indicated in (a), the bond of Fe-O at 582 $cm^{-1}$ was assigned to the naked $Fe_3O_4$ (Hong *et al*., 2007). The bulk $Fe_3O_4$, appeared by the band at 570 $cm^{-1}$ and shift between 520 $cm^{-1}$ to 610 $cm^{-1}$ depending on Fe(Π) content (Zaitsev *et al*., 1999). The carbon-oxygen bonds stretching in the region of 700 $cm^{-1}$ to 1500$cm^{-1}$ is from PCL components (Meerod *et al*., 2008); the bands of carbonyl, C=O, at 1722 $cm^{-1}$ and symmetric and asymmetric of $CH_2$, at 2865 $cm^{-1}$ and 2941 $cm^{-1}$ separately are also from the PCL (Elzin *et al*., 2004).

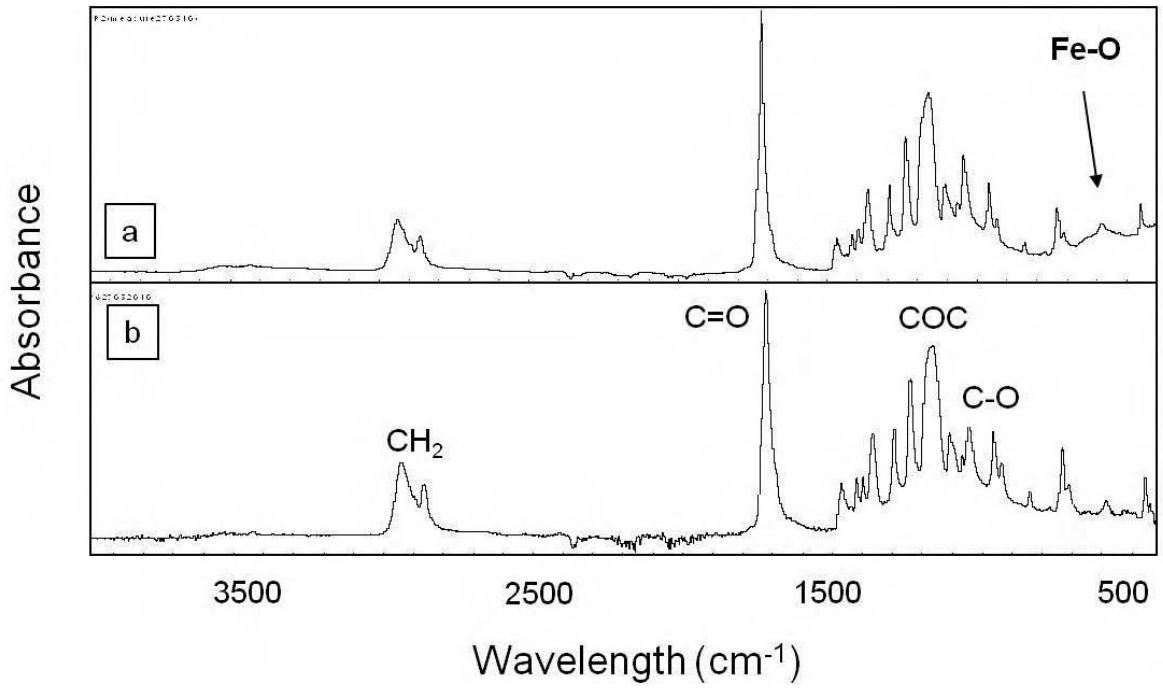


**Figure 8.10 Compound analyses of (a) MP and (b) PCL by FTIR.**

Following the compositional analysis, the crystalline phase of MP microspheres was identified by XRD at 2θ incident angle from 15 to 65 degrees scan. The PCL is indicated by two sharp peaks at 21 and 24, shown in Figure 8.11 (a). The subsidiary graph inside Figure 8.11 (b) was plotted in the range of only from 25 to 55. The peaks of magnetite were indicated by the stars and can be seen clearer in the subsidiary graph: magnetite produces peaks which are less clear than PCL due to the interference of metallic characteristics of magnetite with the X-ray beam. Nevertheless, the appearance of magnetite can still be identified from the subsidiary graph. According to magnetite diffraction patterns as shown previously, the 2θ value of magnetite peaks are mainly present between 25 to 65, which is shown magnified in Figure 8.11 (b). The X-ray may not be able to reach the magnetite particles encapsulated inside PCL, therefore the intensities of the peaks presenting magnetite are much weaker than PCL. It is also to do with the fact that magnetite is

nanocrystalline and therefore does not give a strong signal when characterised using XRD. The low loading rate of magnetite within PCL is the other reason of the presentation of weak signals of magnetite nanoparticles.

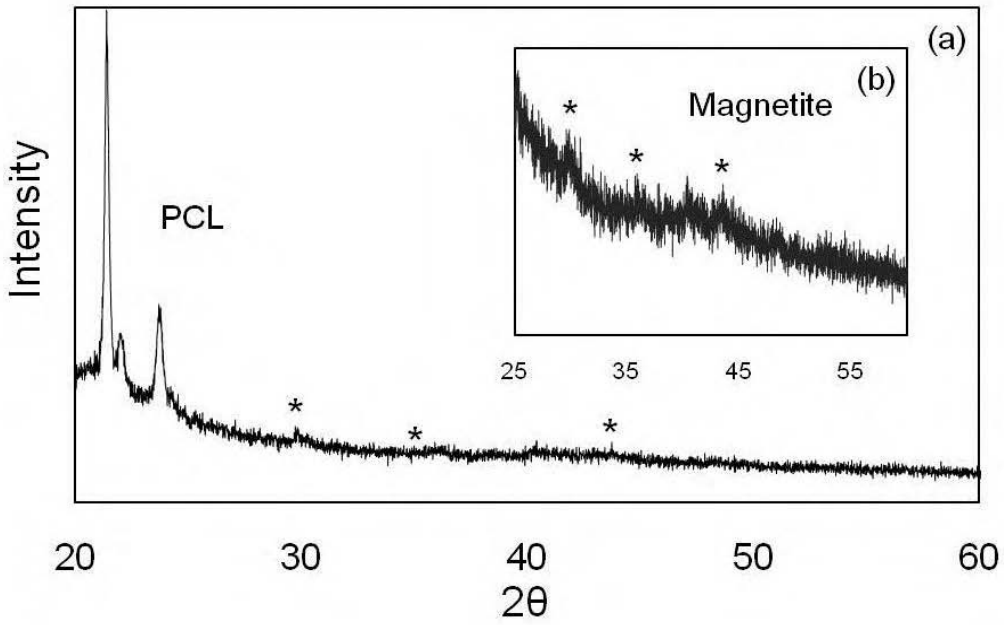


**Figure 8.11 XRD results of (a) MP6 microspheres and (b) subsidiary graph magnified for the peaks of magnetite nanoparticles.**

### 8.3.4 Magnetization of MP microspheres

Magnetizations of MP microspheres were measured by SQUID with a field sweep from -60,000 Oe to 60,000 Oe at 5 K and 300 K. The magnetization curves of MP microspheres indicated that the composites retain the superparamagnetic behaviour as shown in Figure 8.12. The magnetic saturation of MP at 5 K and 300 K were 1.22 emu/g and 0.8 emu/g, respectively, which were much lower than pure magnetite of 46.7 emu/g but still exhibits superparamagnetic behaviour.

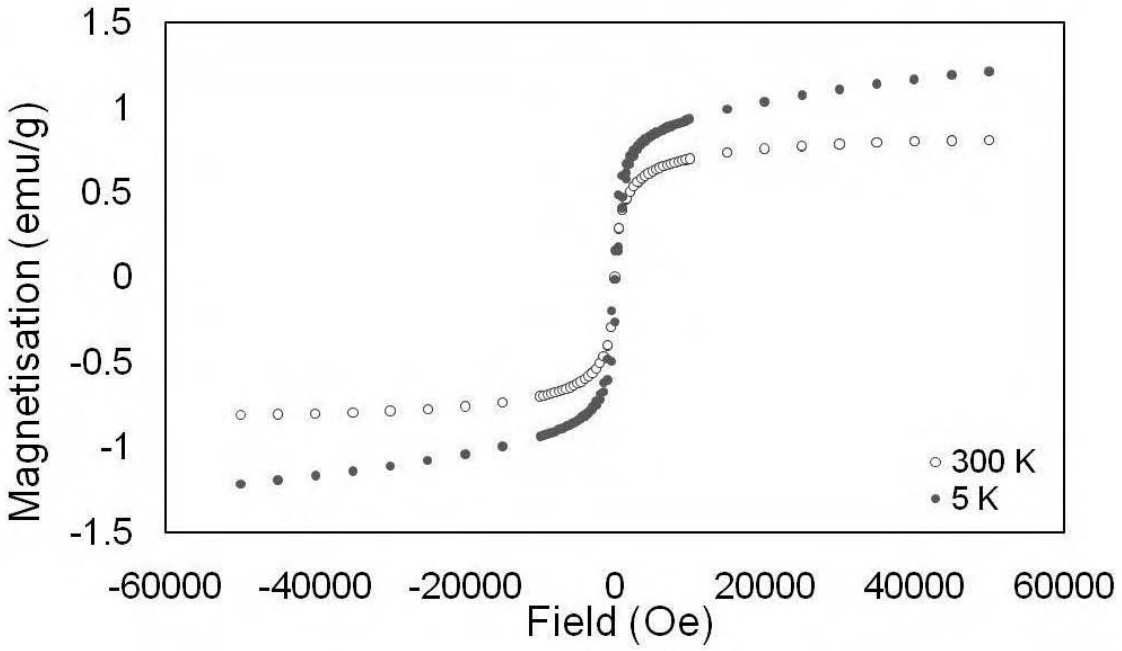


**Figure 8.12 Magnetization curves of MP microspheres at 5 K and 300 K with different magnetic field sweep by SQUID.**

Magnetic saturation of MP had a decrease when microspheres were at higher temperature, which was assumed to be affected by the encapsulated magnetite. The magnetic saturation of magnetite slightly decreased when in a relatively higher temperature environment as demonstrated in section 7.3.6. The experimental data can be compared with the calculated value from the encapsulation rate of magnetite. The mass fraction of magnetite inside MP is 2.68 %, which corresponds to 1.2 emu/g of MP magnetic saturation, which is not a significant difference between the experimental data. This indicates that the procedures of MP production caused no significant oxidisation of magnetite nanoparticles and maintained the superparamagnetism of MP microspheres (Banert and Peuker, 2006). Torcu and collegues reported that the magnetisation of ferrogels showed dependence on the amount of magnetite nanoparticles (Turcu *et al*., 2009).

### 8.3.5 Thermal behaviours of PCL and MP microspheres

DSC was engaged to investigate the thermal behaviours of MP and PCL polymers with a heating rate of 10 ℃/min and cooling down to original temperature after holding in the set highest temperature for one minute. Two heating up processes, due to the different melting ranges, carried on from 25 ℃ to 60 ℃ and 25 ℃ to 100 ℃ separately for PCL2 and PCL6 polymers and their encapsulated microspheres, MP2 and MP6. To observe the energy requirement and melting point occurrence, the results present by specific heat (J/g× ℃) and temperature (℃) dependence.

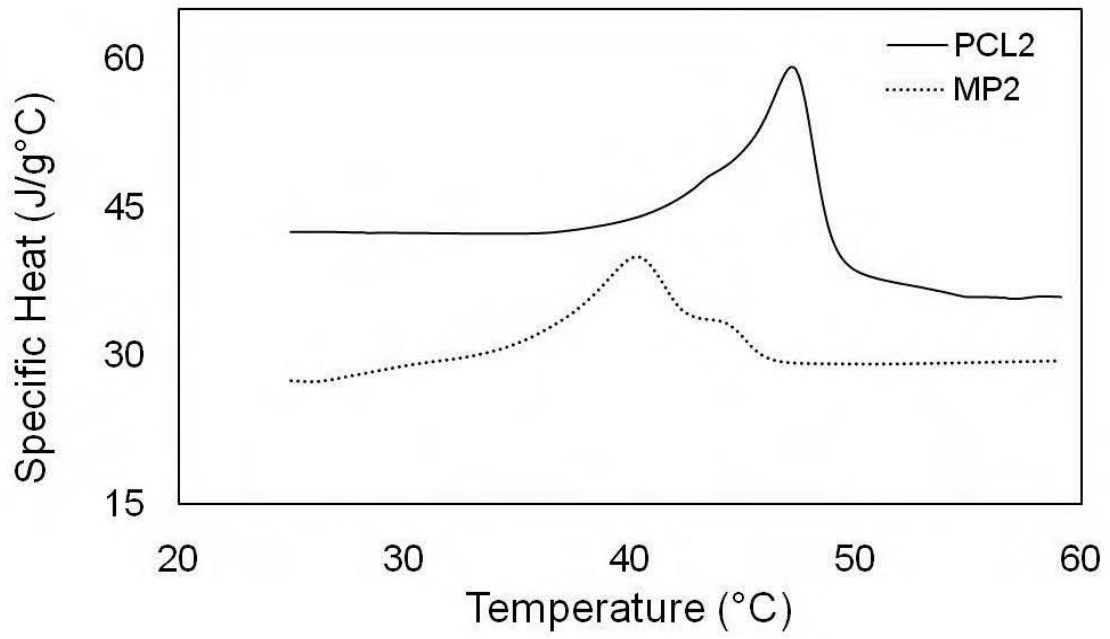


**Figure 8.13 The endothermic behaviour of PCL2 and MP2 microspheres.**

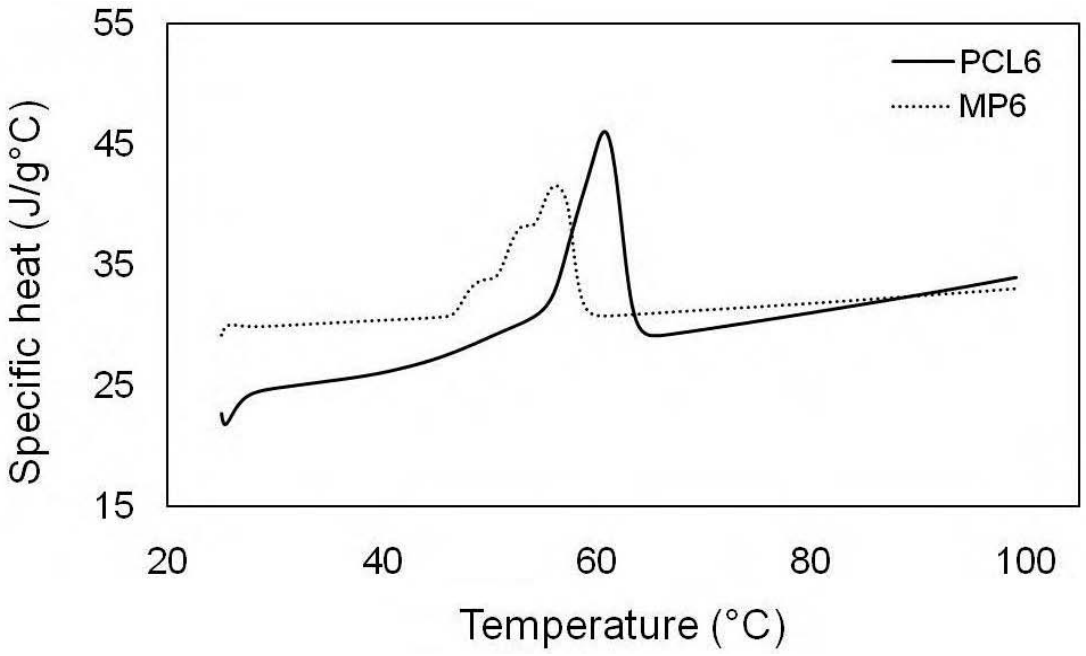


**Figure 8.14 The endothermic behaviours of PCL6 and MP6 particles.**

In Figure 8.13, the endothermic curves performed the melting behaviours of PCL2 and MP2 during the heating process. The melting points of PCL2 and MP2 particles appeared at 47 ℃ and 40 ℃, respectively. The other type of PCL also displayed the change of thermal behaviours by the encapsulated magnetite. The endothermic curves of PCL6 and MP6 polymers are shown in Figure 8.14. The significant melting transition peaks of PCL6 and MP6 were both present at before 60 ℃, but the melting point of MP6, 56 ℃, is slightly lower than melting point of PCL6, 58 ℃. Apparently, both MP2 and MP6 melting began with earlier stage than the PCL particles without loaded magnetite. The energy requirements (enthalpy) to achieve phase change of both MP2 and MP6 are relatively lower than PCL2 and PCL6, respectively. Furthermore, the curves of both MP2 and MP6 displayed small amounts of fluctuations indicating impurities, which were assumed to be from the encapsulated magnetite nanoparticles.

Iron oxides are well known of high stability and the oxidation reaction happens only above 500℃. Although particles at the nano-scale have a greater surface area, and therefore can be oxidised at much lower temperatures. The peak indicated oxidisation is higher than 200 ℃ (Sanders and Gallagher, 2003) (Redl *et al*., 2004). Furthermore, the DSC results of magnetite nanoparticles from chapter 7 performed a stable curve in the temperature sweep between 25 ℃ and 200 ℃. In addition, the peaks in the curves of MP2 and MP6 are relatively near the peaks of PCL2 and PCL6. For these reasons, the peak areas of MP2 and MP6 were assumed to be from PCL2 and PCL6, respectively. In the report by Weidenfeller *et al*, the thermal transport properties, heat capacity and density of polymer can be changed by additional metal and oxide particles. They especially noted that magnetite containing polymer shows relatively higher thermal conductivity. High thermal conductivity provides high thermal diffusivity, which is responsible for an efficient moulding process (Weidenfeller *et al*., 2004). This can explained the earlier stage of melting occurred in MP2 and MP6 than the melting of PCL2 and PCL6. Thermal properties of both PCL2 and PCL6 are affected by encapsulated magnetite nanoparticles. The appearances of magnetite in PCL lead to higher thermal conductivity and diffusivity therefore PCL melting can occur at lower temperatures, which can be advantageous for further thermal treatment manipulation of the product.

## 8.4 Conclusion

According to the electron micrographs, PCL2 and PCL6 are stable and exhibit few outward changes in both dry and wet conditions; this is advantageous for storage and further *in vitro/in vivo* applications. However, the particles sizes of PCL fluctuated with manufacturing conditions, which is assumed to be affected by the stabilisers used rather than by the mixing conditions. The PCL were hollow spheres and the presence of magnetite did not significantly change the morphology of microspheres.

The results from EDS, FTIR and XRD demonstrated the appearance of magnetite nanoparticles in the MP microspheres, which indicates the successful formulation of MP microspheres. The majority of the encapsulated magnetite nanoparticles are assumed to be encapsulated within the PCL shell, because of the weak peaks of magnetite displayed in the XRD results of MP microspheres. The micrographs of the cross sections of MP microparticles are another form of evidence of the full encapsulation of the magnetite particles. Therefore, the magnetic saturation of MP microspheres was measured by SQUID, and the result indicated MP particles possessed a superparamagnetic behaviour. The thermal properties of PCL2 and PCL6 have changed by the encapsulated magnetite nanoparticles. The existence of magnetite in MP particles lead to higher thermal conductivity and diffusivity and consequently left the PCL melting point at a lower temperature which brings a benefit of soft particles with less energy generation and becoming mouldable for bone fillers.

# Chapter 9 The influence of heat treatment on the thermal properties of MP microsphere

## 9.1 Introduction

When placed in an external altering magnetic field, magnetite (depending on size) causes a rise in temperature due to the hysteresis loss or relaxation. Consequently, magnetite has been used in fine particles for the localised treatment of tumours. (Neel, 1949, 1953; Morales *et al*., 1957). Two other papers were published on the loading of magnetite into polymers for drug delivery (Zaitsev *et al*., 1999; Yang *et al*., 2006).

The objective of this chapter is to use the heat from the encapsulated magnetite nanoparticles to soften the MP microsphere. In order to soften the MP microspheres *in situ*, MP microspheres were heated by an alternating magnetic field (AMF). A uniform field has to be produced before it can be used to soften the MP microspheres. Following AMF treatment, the physiochemical properties of the MP microspheres may be different as a result of the phase change induced by heating. Observations of morphology and thermal properties of the MP particles were undertaken after the AMF treatment. In addition, heating of the encapsulated magnetite in the polymeric matrix was demonstrated by a controllable source of energy, a microwave. Since magnetite produces heat when exposed to microwaves (Kirschvink, 1996), microwaves were used to control heating within the matrix.

## 9.2 Material and method

The MP particles were formed by the evaporation emulsion method as described in section 8.2 and were characterised according to the technology used in section 8.3. In comparison to PCL microparticles, the resultant MP particles have relatively low melting points due to the encapsulated magnetite providing a higher thermal conductivity. Heat treatments were carried out to soften the polymers using two heating devices; an AMF and a microwave. The thermal behaviour of MP microspheres was measured using DSC, and the results were converted to the crystallinity degree of PCL polymers. The altered crystallinity was used as an indication of the property change and therefore the heating of the encapsulated magnetite.

### 9.2.1 Heat treatment by AMF

Heat treatments for MP microspheres were undertaken with different concentrations of magnetite within PCL microspheres. The AMF device was specifically designed to generate a magnetic field at a low power and was applied to soften the MP microspheres. The schematic diagram of the AMF is shown in Appendix 1. In a joint project (undertaken by Mr. R. Dickerson and Dr. S. Hillmansen, School of Electronic, Electrical and Computer Engineering) a power supply inverter was modified to be capable of controlling the electric potential (voltages, V) and the resonance frequencies (Hertz, Hz). The power controlled and converted by the inverter was subsequently connected to a conductor to create a magnetic field. Different field densities (milli-tesla, mT) were generated by controlling the power and frequency. The magnetic field density of AMF was determined by a Gauss meter (for air gap field) (Fluke 289 True-RMS Logging Multimeter, Fluke

Co., USA). The current yield in the electric circuit can be observed and represent by mini-ampere (mA) from the oscilloscope (LeCroy 9304A, LeCroy Ltd. USA).

The sample was placed between the two cores of the conductor with the magnetic field. The distance between the two cores (described as the air gap) is one of the factors affecting the field density. Therefore, the effect of gap size on field density was investigated. An Infrared (IR) thermal sensor (Micro-Epsilon, UK Ltd.) and a thermocouple were employed to monitor the temperature of the samples and the conductor, respectively.

The AMF is capable of generating several field densities, which can subsequently soften MP microspheres without the additional heating equipment. The thermal property difference of the polymers before and after being exposed to the magnetic field was used to define the success of the AMF treatment.

### 9.2.2 Heat treatment by Mini-microwave

A mini-microwave (Discover, S class, CEM Co., US) was used to detect the temperature fluctuation during the heating treatments (infrared sensor, programmable from 0 ℃ to 300 ℃). This section focuses on the effects of magnetite quantity on altering temperature during the microwave heating procedures. Sample MP6 with various encapsulation percentages of the encapsulated magnetite were employed to demonstrate the temperature charge during the heating process. The heating processes were carried out using 20 watts (W) and 40 W for 20 seconds and 47 seconds respectively. The MP samples were dispersed in distilled water with the controlled

concentration of 5 mg/ml and the liquid was added into a glass tube containing distilled water for measurement.

## 9.3 Results and Discussions

The first part of this section is the results of field densities that were derived from the AMF with altered gap size, frequency and power. In the following parts are the thermal properties and the morphologies of the MP particles (before and after the heat treatment).

### 9.3.1 Field density of the AMF

The use of an alternating magnetic field generated by high power and frequency supply (up to mega Hz) for hyperthermia applications has been widely reported (Okawa *et al*, 2006; Hergt *et al*, 2004). The treatment by a strong AMF or heater may be harmful for neighbouring tissues. This study focuses on using an AMF generated by a limited power supply to soften particles, which offers a cheap and low power requirement method for polymer melting for bone replacement.

In order to obtain identical AMF conditions as a means of heating the MP particles, AMF was generated at different gap distances and various combinations of frequencies and power. Figure 9.1, shows the magnetic field generated under a steady electric potential of 80 V, and various frequencies with different gap size. At different gap sizes, the presence of the air gap had an effect on field density. The field densities, displayed a decrease with gap width (from 1 mm to 3.5 mm, respectively). Stronger field strength was generated when combing a lower frequency with a steady supply of electric potential. The four curves indicate that the greater the gap size,

the lower the field density. By comparison, in the weaker field densities derived from 200 Hz and 400Hz, the gap effect was less notable than in the greater field densities derived from 20 Hz and 100 Hz.

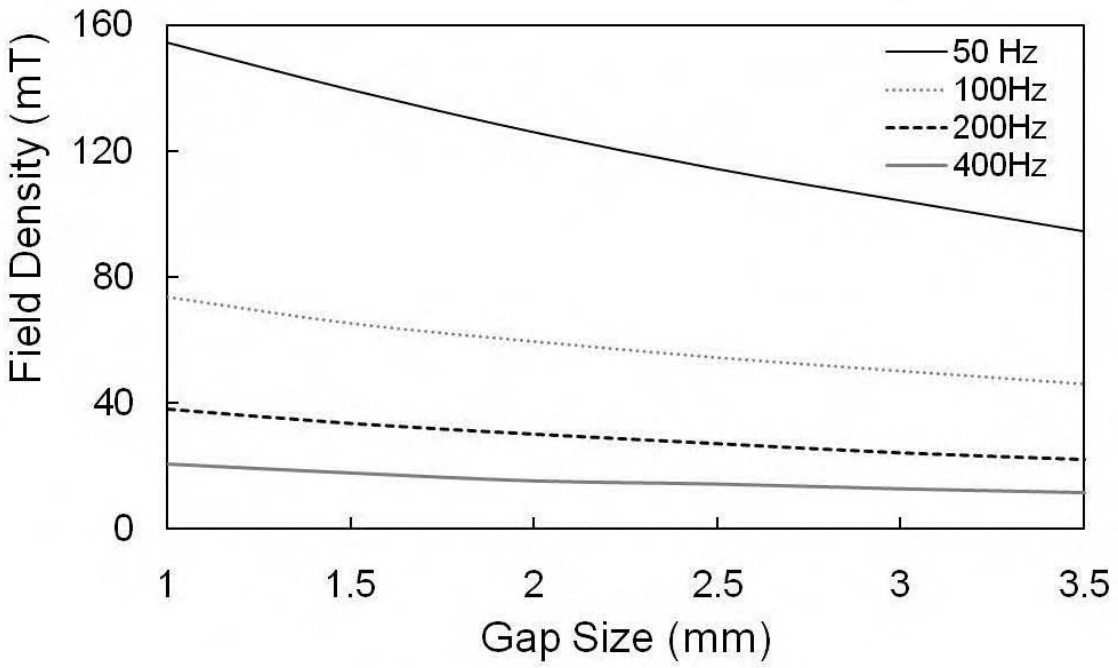


**Figure 9.1 Field densities at different gap distances at 80 V and various frequencies.**

In Figure 9.2, magnetic fields were generated by combining several of frequency and voltages generating. As the gap size of 1 mm was resulted from the sample volume, the smallest gap size that can be controlled in this device, 1.5 mm, was selected as a consistent air gap in Figure 9.2. A similar trend was observed to that can be seen in Figure 9.1, a stronger field density occurred when a lower frequency was combined with a steady supply of electric potential and the gap distance. Again, the trends are much more obvious in the low frequency curves. On the other hand, higher voltage inputs with a steady frequency gave higher field strength.

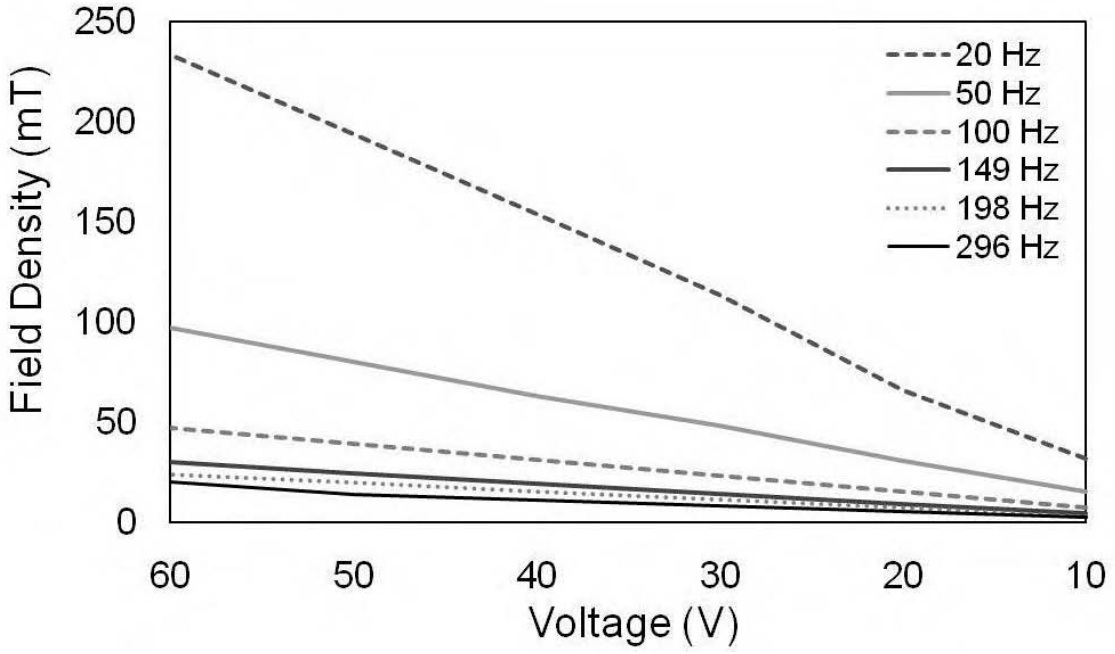


**Figure 9.2 Field densities at different voltage and frequency with a consistent gap of 1.5 mm.**

From Figure 9.1 and 9.2, it can be seen that higher field density results when reducing frequency. A fundamental of electromagnetic field is that high voltage leads to a stronger field density. By contrast, the field density is lower with a larger air gap at constant electric potential.

A smaller gap width generates a stronger magnetic field than a larger gap. However, higher electric potential derived electromotive currents, (shown in Figure 9.3) resulted in greater electrical resistance that leads to an undesired temperature rise in the coil (Yamaguchi et al, 2005). The temperature increase of the coil is harmful for devices located in the AMF, and more importantly will transport the heat to the conducted core and affect the results of thermal properties of MP microspheres.

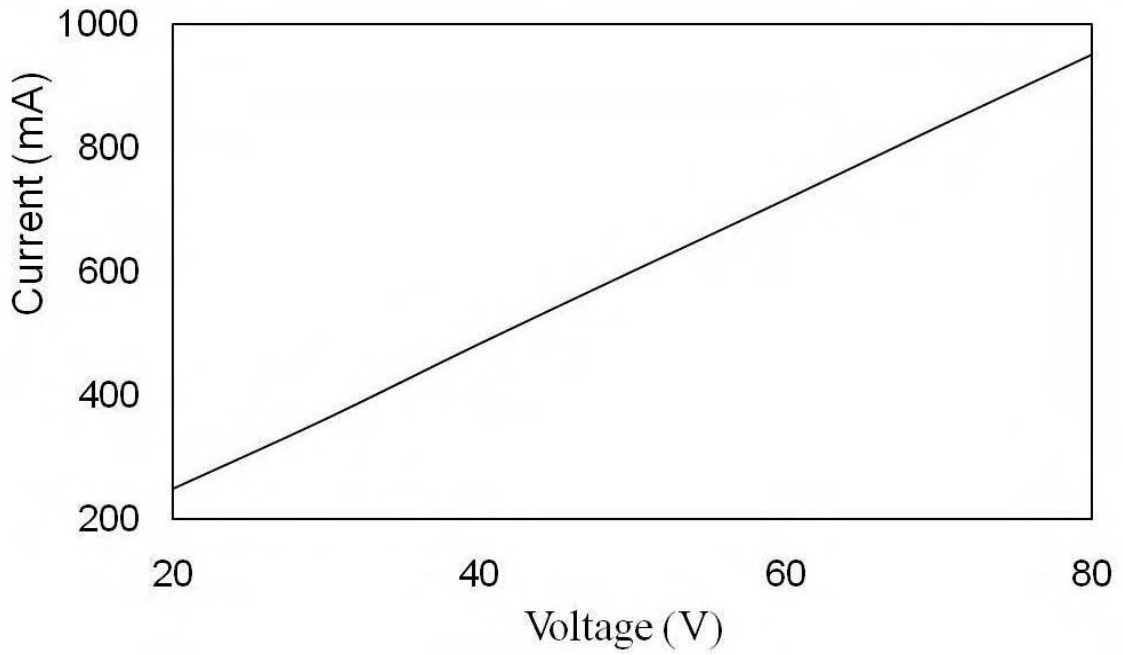


**Figure 9.3 Current recorded at 20 Hz and different voltage with a 1.5 mm gap.**

Demonstration of the temperature rise in the coil is shown in Figure 9.4. The increase of the coil temperature was evaluated using IR sensor, observed during the field generated by combing a high voltage and a low frequency (80 V and 20 Hz). The peak is an artefact of the equipment. The core showed a rise in temperature of 2 ℃ in ten minutes during the field generation. It should be noted that the field strength is relative stronger at 20 Hz according to Figure 9.1. Therefore, the temperature change of the conducted cores during the field was recorded by inverting the electric frequency at 20 Hz with the various voltages. In Table 9.1, the AMF was generated by inverting 20 Hz with 80 V, 30 V and 20 V, and the temperature of the conducted core was measured by a thermocouple.

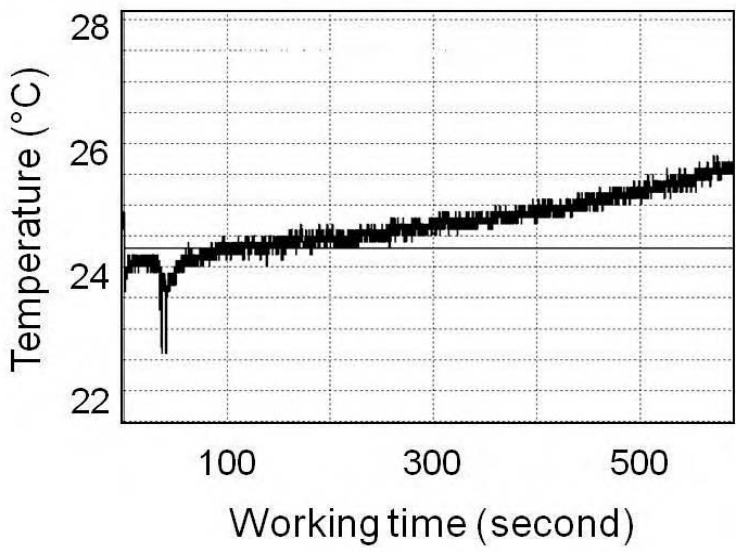


**Figure 9.4 IR sensor measured temperature at 20 Hz and 80 V.**

The MP6 particles were placed in between the cores of the AMF equipment and the sample volume gave a gap of 0.08 mm, which is under the minimum of the capable range of IR detection; therefore the sample temperature was measured by the IR sensor before and after AMF treatment. A. B and C are the result groups of the AMF generated at 80 V, 30 V and 20 V with a constant frequency, 20 Hz, as show in Table 9.1. The temperature of the cores increased in the AMF, and the temperature increase rates of the AMF at 80 V and 30 V are higher than the AMF at 20 V. The AMF generated at 80 V was used to observe the temperature increase without loading a sample. The result of sample B exhibited a similar temperature rise (0.17 ℃/min) and the sample temperature increase rate (0.15 ℃/min); which demonstrates a slight difference and indicates that the sample heating was affected by the warming core. On the other hand, the result of sample C exhibited a relative low temperature rising rate to that of the conducted core, and the final temperature of the sample (MP6) was higher (19 ℃ to 21.5 ℃) with a temperature rise rate of 0.025 ℃/min.

**Table 9.1 Temperature increase during AMF generation at 20 Hz.**

| | | A | B | C |
|---|---|---|---|---|
| Electric potential (V) | | 80 | 30 | 20 |
| Field density (mT) | | 325 | 114 | 74 |
| Temperature rise rate (°C/min) | Core | 0.2 | 0.17 | 0.003 |
| | Sample | - | 0.15 | 0.025 |

Therefore, the magnetic field generated by 20 Hz and 20 V demonstrated relatively ideal conditions, with less undesired heat from the warming coil and therefore the conducted cores; the air gap should be as small as possible for higher field strength (Figure 9.1). However, the volume of sample exhibits space between the conducted cores and resulted in an air gap in the magnetic field. The smallest gap of 0.8 mm, was a result of sandwiching the MP microspheres between two plastic slides and placing them onto the conducted core, and the smallest controlled air gap here is 1.5 mm in width. The field densities of the AMF was varying frequency at 20 V with gaps of 1.5 mm and 0.8 mm respectively are shown in Figure 9.5. As previous results shown (Figure 9.2), the field strength is stronger when a lower frequency is used, and the field observed at 20 V and 20 Hz is the relative ideal condition (Table 9.1). According to the results in Figure 9.5, the field density derived with the 0.8 mm gap is approximately 5 times greater than the field density derived with the 1.5 mm gap. Consequently, the ideal conditions for generating the AMF are combining the frequency at 20 Hz and the electric potential at 20 V with an air gap of 0.8 mm.

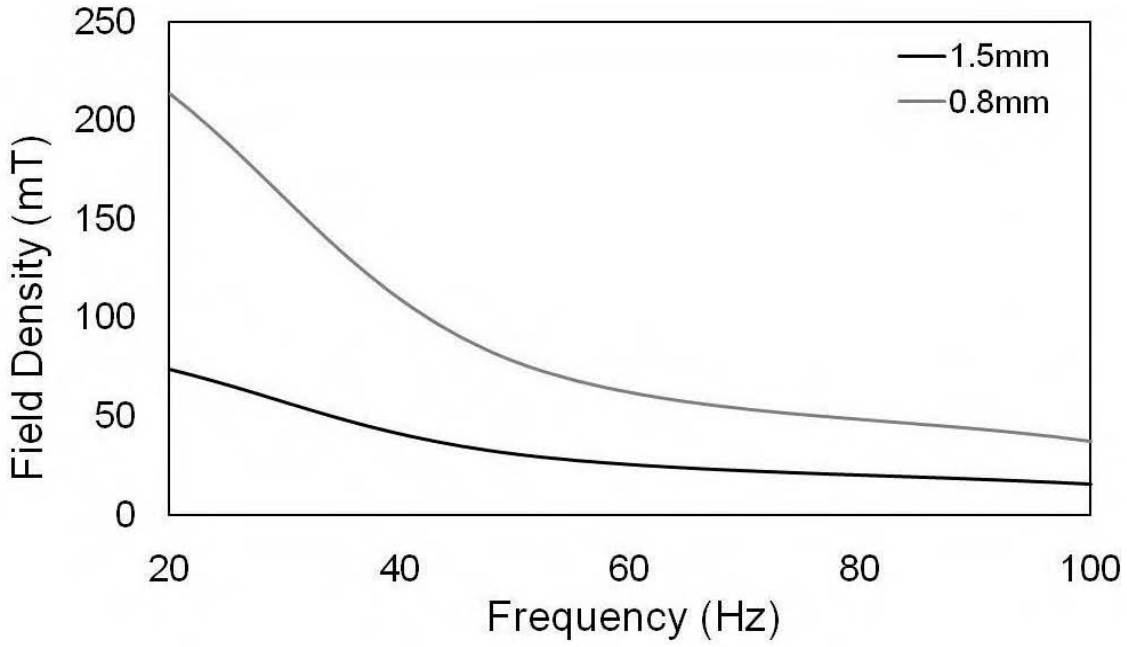


**Figure 9.5 Field strength yield at 20 V and varying frequency for the two air gaps, 1.5 mm and 0.8 mm.**

Collaborating with Electronic, Electrical and Computer Engineering, the AMF equipment was set up at 20 Hz and 20 V due to the relative high field strength and the minimisation of device coil warming. This set up was used for the following heat treatments and drug release research.

### 9.3.2 Morphology

The morphologies of the MP particles before and after AMF treatment were observed by loading the MP particles into an irregular shape (model of bone defect) and placing in the magnetic field. The macrographs in Figure 9.6, (a) to (e), illustrate the softening and melted particles filling the irregular cavities and importantly the polymer could be moulded into any shape. Figure 9.6 (a) and (b) are the macrographs of MP6 (a) before and (b) after AMF treatment and were attached to

a 2D-mold graph of bone defect to illustrate that the softened particles can fill the irregular trauma. Figure 9.6 (c) shows the 3D-mold shape of unlimited concave to allow filling of more particles, (d) demonstrates the loose particles that have been spread onto the model shape before AMF treatment; and Figure 9.6 (d) presents the polymers filling the pattern after the AMF treatment and after the model shape was removed. The resultant particles in (b) are brown agglomerates, which are different between the loose pale brown particles in (a). The resultant brown colour displayed in (b) is assumed from the encapsulated magnetite particles exposed after the PCL matrix fused together. Similar to Figure 9.6 (a), the particles were loosely dispersed in the shape shown in (d); and then after the AMF treatment, became the well-shaped pattern after the model template was removed, shown in (e). The resultant particles in (e) also displayed a darker brown colour.

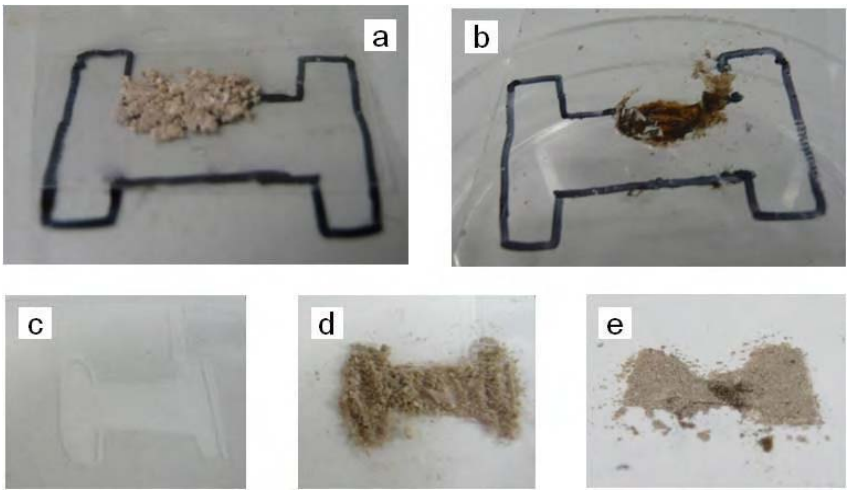


**Figure 9.6 Macrographs of MP6 before and after AMF treatment. (a) non-treated MP6 above a 2D-mold figure of bone defect, (b) AMF-treated MP6, (c) the 3D Perspex mould, (d) the loose particles spread onto the model shape before AMF treatment and (e) shaped pattern after AMF treatment and the removal from the mould.**

The dispersion of magnetite inside the MP microspheres was detected by Micro-CT before and after the AMF treatment. The 2D pixel of micro-CT was correlated to the material density and the resultant 2D map reveals the material phases within the specimen (Ho and Hutmacher, 2006). Magnetite nanoparticles were sprinkled around an agglomerate of PCL6 inside a container as shown in Figure 9.7 (a). The PCL and magnetite are seen as orange and purple, respectively, as a result of the two different densities within the particles. Figure 9.7 (a) was therefore used as the colour index for future images from the micro-CT. MP6 microspheres in Figure 9.7 (b) demonstrates the dispersed particles within the container, and (c) shows the micro-CT scan. The Micro-CT scan recorded the samples layer by layer, up to approximately 250 layers. Figure 9.7 (c) and (d) are the upper and lower layers of the sample, respectively. The two images display the orange and purple colours mentioned above. The presence of these colours indicated that the particles contain both PCL and magnetite. This indicates that magnetite nanoparticles are dispersed within the microspheres. The resolution of Micro-CT is about 5 microns and the present of nanomagnetite in MP maybe due to the porosity of MP agglomerates and the damaged MP after heat treatments.

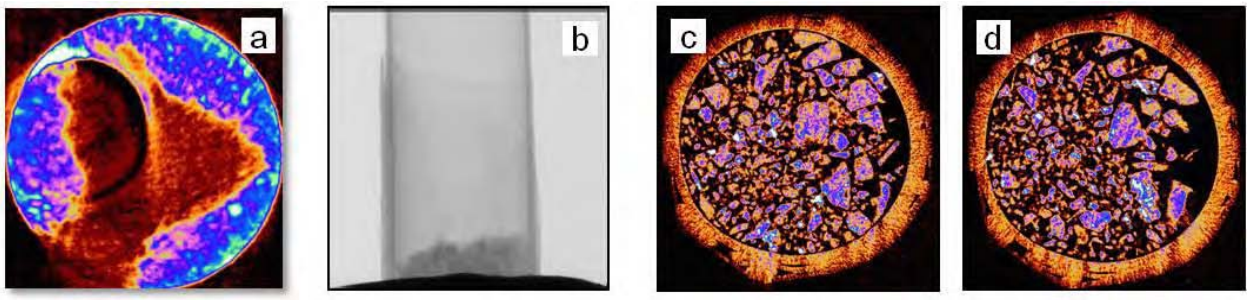


**Figure 9.7 (a) Magnetite and PCL separately; MP of (b) X-ray images and (c) from upper and (d) lower layers of MP6 microspheres.**

The AMF treated MP microspheres are shown in Figure 9.8. Figure 9.8 (a) shows the raw image of a section of fused MP agglomerate (hold by seal tape for micro-CT measurement) as demonstrated in Figure 9.6 (e). The loose particles cohered into agglomerate after AMF treatment in Figure 9.8 (b) and (c) (the upper and lower layers). These exhibited the two major colours, orange and purple, which indicates MP microspheres fused after softening during the AMF treatment. By contrast to previous loose particles (Figure 9.7 (c)), the orange area appears more dominant with purple spots representing partially assembled magnetite within the compound. The assembling of magnetite is assumed to be attributed to the attraction of the embedded magnetite particles exposed after the PCL particles softened and melted in the presence of the magnetic field. The melting and formation of agglomerating is a fundamental requirement in desired filling materials, and is evident here.

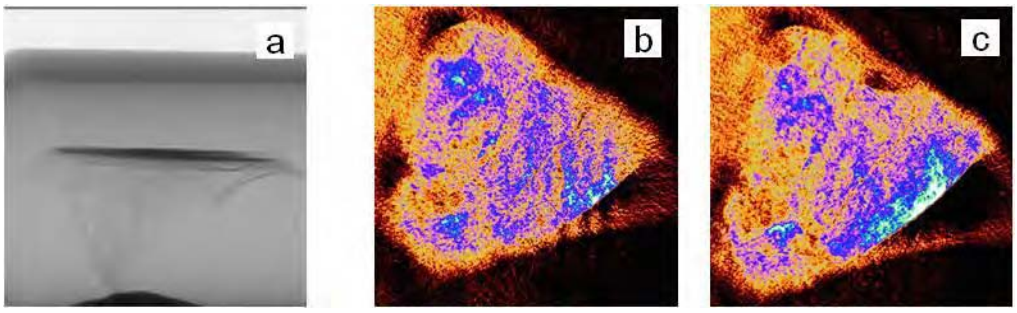


**Figure 9.8 (a) agglomerate (b) upper and (c) lower layer of AMF treated MP.**

From the macrographs and Micro-CT results, it can be assumed that the MP microspheres have been softened by the AMF treatments. Once softened, the solid phase and spherical shape of the MP microspheres were expected to change and ESEM images were used to illustrate this in

support for AMF-treated MP. Figure 9.9 shows (a) the whole agglomerate, (b) the fused area, (c) the melted MP with some un-melted particles, (d) a layered agglomerate, (e) disrupted MP6 microspheres, (f) disrupted MP2 particle microspheres, (g) cohered MP microspheres, (h) loose microspheres, (i) damaged microspheres, (j) magnification of (i), (k) a single domain of MP6 and (l) a damaged single domain of MP6. A red square indicates the disrupted area of the microspheres after AMF treatment.

Figure 9.9 (a) to (f) are treated by AMF and observed by ESEM individually. The final six images, Figure 9.9 (g) to (l), are from the same sample at different ESEM magnifications. AMF treated MP microspheres either cohered in agglomerates or damaged particles. The images exhibit disruptions to the surface of several microspheres in both MP6 (e) and MP2 (f) sample, which are not observed from the images of both MP2 and MP6 microspheres before AMF treatment (Figure 8.8). Images (g) to (l) were captured at varying magnifications to demonstrate clearer views of the structural defect on the microspheres. Image (g) shows the cohered particles; and (h) shows a few loose particles around the cohered agglomerate. Although the loose microspheres in (h) were not softened as the cohered counterparts, the surfaces shows disruption as a result of AMF heating. Image (k) is a single microsphere; the central of the surface displays a collapsed area. Additionally, images (i), (j) and (l) were captured from magnification of the cohered area of (g). The images illustrate damaged microspheres with the particle shells ruptured and becoming non-spherical in shape. These ruptured MP2 and MP6 microspheres are presumed to be damaged by the local heat generated from the embedded magnetite. These microspheres were softened, and therefore clustered into an irregular agglomerate upon cooling.

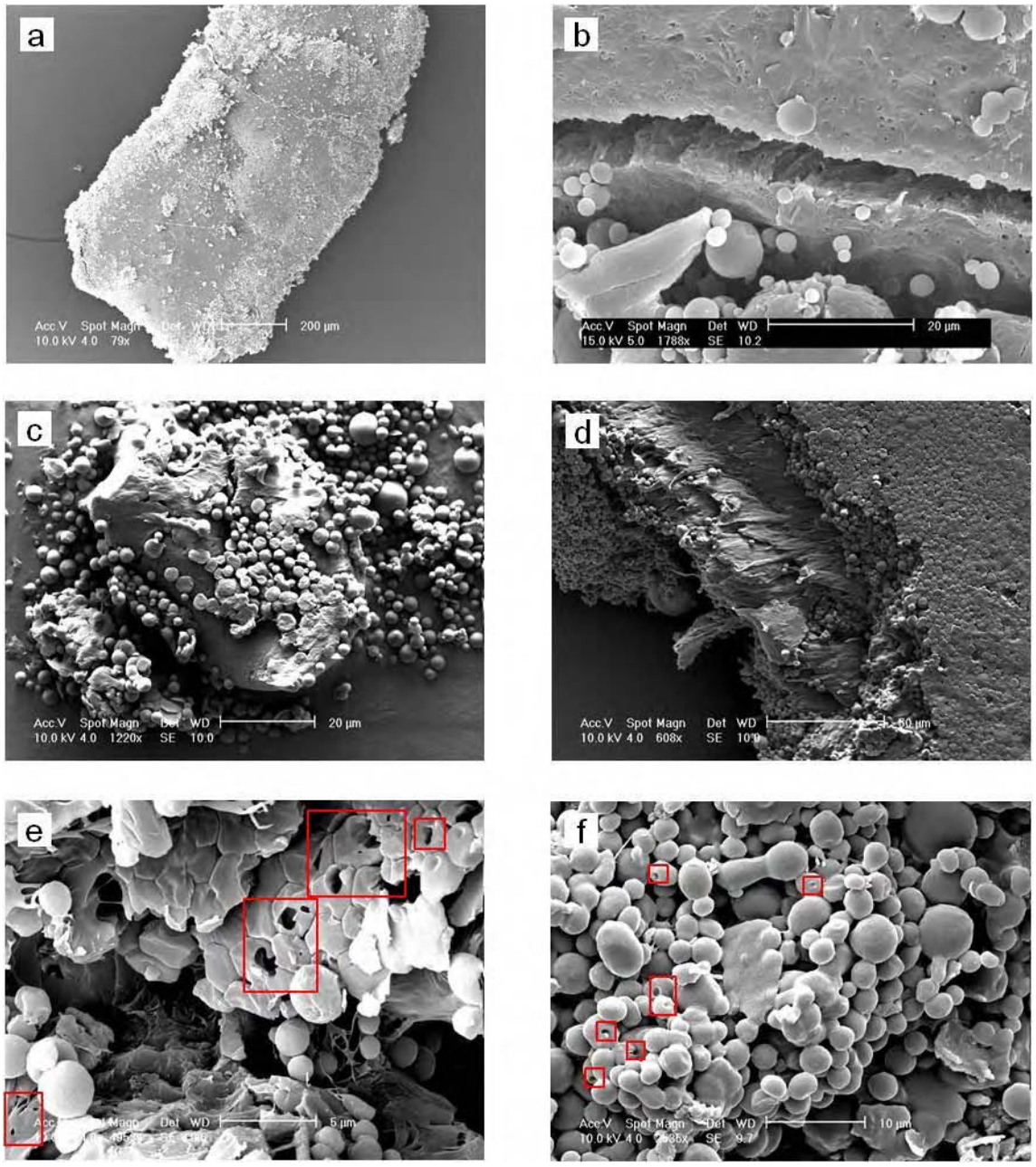


**Figure 9.9 Micrographs of MP microspheres after AMF treatment: (a) the whole agglomerate, (b) the fused area, (c) the melted MP with some un-melted microspheres, (d) a layered agglomerate, (e) disrupted MP6 microspheres, (f) disrupted MP2 microspheres.**

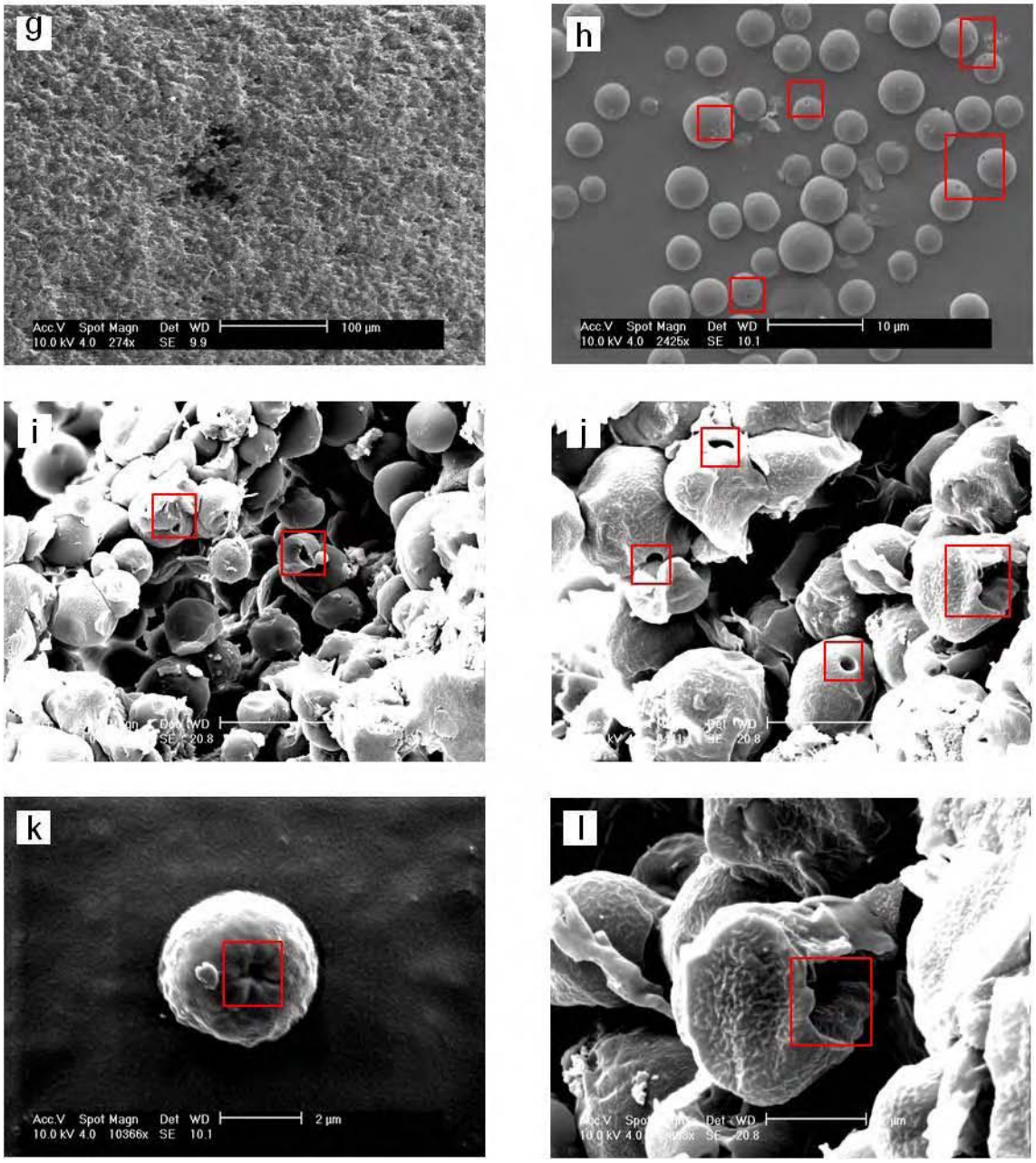


**Figure 9.9 Micrographs of MP particles after AMF treatment: (g) cohered MP microspheres, (h) loose microspheres, (i) damaged microspheres, (j) magnification of (i), (k) a single domain of MP6 and (l) a damaged single domain of MP6.**

In conclusion, the morphologies of MP microspheres from macrographs (Figure 9.6 and 9.8) and micrographs (Figure 9.9) indicated successful heating of the MP particle microspheres during AMF treatment. Further analysis of the thermal properties of the polymer can be used to define the difference between PCL (no loaded-magnetite) and MP after AMF treatments, and can therefore be used as an indicating of successful the heating caused by embedded magnetite.

### 9.3.3 Thermal property

The existence of magnetite within the microspheres may have introduced effects on the three-dimensional structure of the polymers, which can lead to polymer instability due to perturbations weakening of the van der Waals interaction between the polymer chains (Vijaya *et al*., 2000). The mechanical properties of the polymers can be determined in terms of the degree of crystallinity (Kong and Hay, 2002). Crystallinity degree is calculated from Equation 9-1, where $\Delta H_{PCL}$ is the thermodynamic melting enthalpy of 100% crystalline PCL and $\Delta H$ is the melting enthalpy of the sample (J/g). The value of $\Delta H_{PCL}$ is 136 J/g (Crescenzi *et al*., 1972; Saad *et al*., 2010).

$$\text{Crystallinity } \% = \Delta H / \Delta H_{PCL} \times 100\ \% \qquad 9\text{-}1$$

Figure 9.10 shows the change in crystallinity of PCL2 and MP2 particles before (grey bars) and after (dark grey bars) the AMF treatments, respectively. MP2 has 7.5 % of magnetite encapsulated in the microspheres (determined by TGA). Thermal properties of PCL2 and MP2 are shown in Table 9.2. In the case of non-AMF treatment, PCL2 (the first grey bar) exhibits a higher degree of crystallinity than MP2 (the second grey bar) where the crystallinity of PCL2 and MP2 are 66.6 % and 56.8 % respectively. The crystallinity is approximately 10 % lower after encapsulation of magnetite nanoparticles. The melting temperature of MP2, 40.4 ℃, is much lower than the melting point (47 ℃) of PCL2 after loading magnetite into the polymer, which is induced by the heat conductivity of magnetite as discussed in Chapter 8.

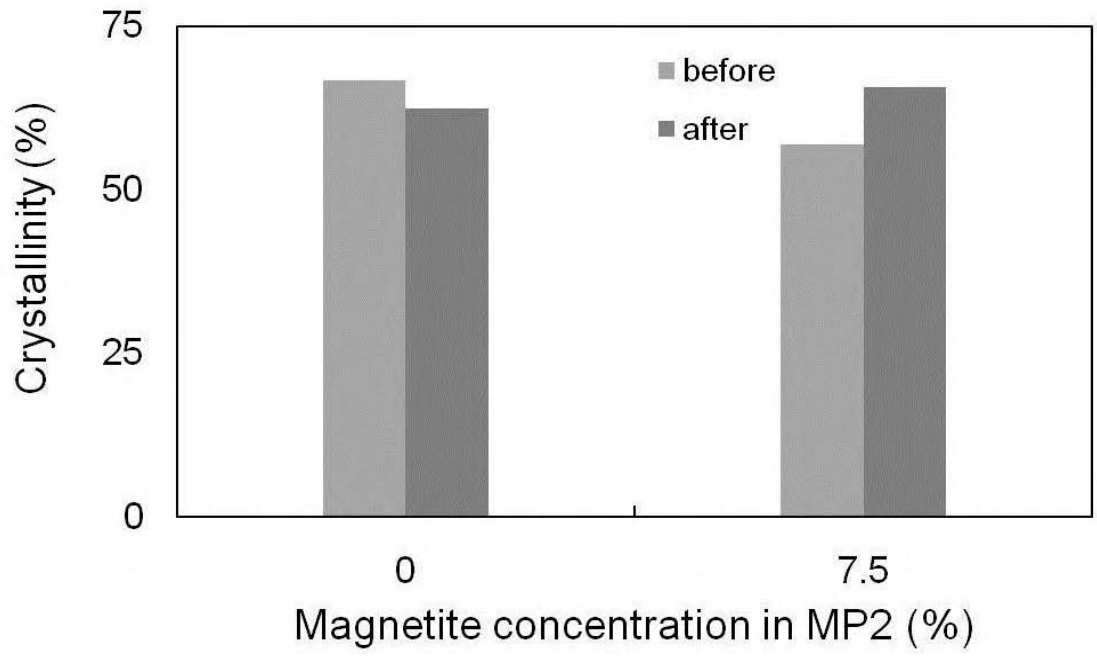


**Figure 9.10 Crystallinity changes of PCL2 and MP2 microspheres before and after AMF treatments.**

After AMF treatment, the crystallinity of PCL2 (the first two bars) falls slightly (by 6 %) after treatment by AMF, whereas MP2 (the last two bars) shows an increase of crystallinity. By contrast, the melting points of both PCL2 and MP2 after treatment by the AMF are 49.1 ℃ and 42.6 ℃ respectively, which have increased by approximately 2 ℃ for both PCL2 and MP2. The difference in crystallinity after treatment by AMF indicates a 6 % loss for PCL2 and a 15 % increase of MP2. The crystallinity change is obtained from Equation 9-2, where $C_{AMF}$ is the crystallinity of sample after treatment by AMF and the $C_{NO}$ is the crystallinity of sample without AMF treatment.

$$\text{Crystallinity change } \% = \frac{(C_{AMF} - C_{No})}{C_{No}} \times 100\ \% \qquad 9\text{-}2$$

**Table 9.2 Thermal properties of PCL2 and MP2 particles before and after AMF treatments.**

| MP (%) | $T_m$ (℃)* | | Crystallinity (%) | | Crystallinity change (%) |
|---|---|---|---|---|---|
| | No | AMF | No | AMF | |
| 0 | 47.3±0.1 | 49.1±0.3 | 66.6±1.3 | 62.3±0.4 | -6.4±2.4 |
| 7.5 | 40.4±1.5 | 42.6±0.6 | 56.8±0.7 | 65.7±1.3 | 15.8±0.2 |

$T_m$ (℃)*: recorded by DSC.

The thermal effects of AMF can be better understood by a comparison of the two types of PCL and MP microspheres. The mechanical properties affected by thermal fusion of PCL6 and MP6 particles after AMF treatment are also demonstrated.

In Figure 9.11, the degrees of crystallinity for magnetite encapsulation rates of MP6 (0 %, 3 % and 5 % respectively) are shown for before and after AMF treatments. The thermal properties and crystallinity change for PCL6 and MP6 are presented in Table 9.3.

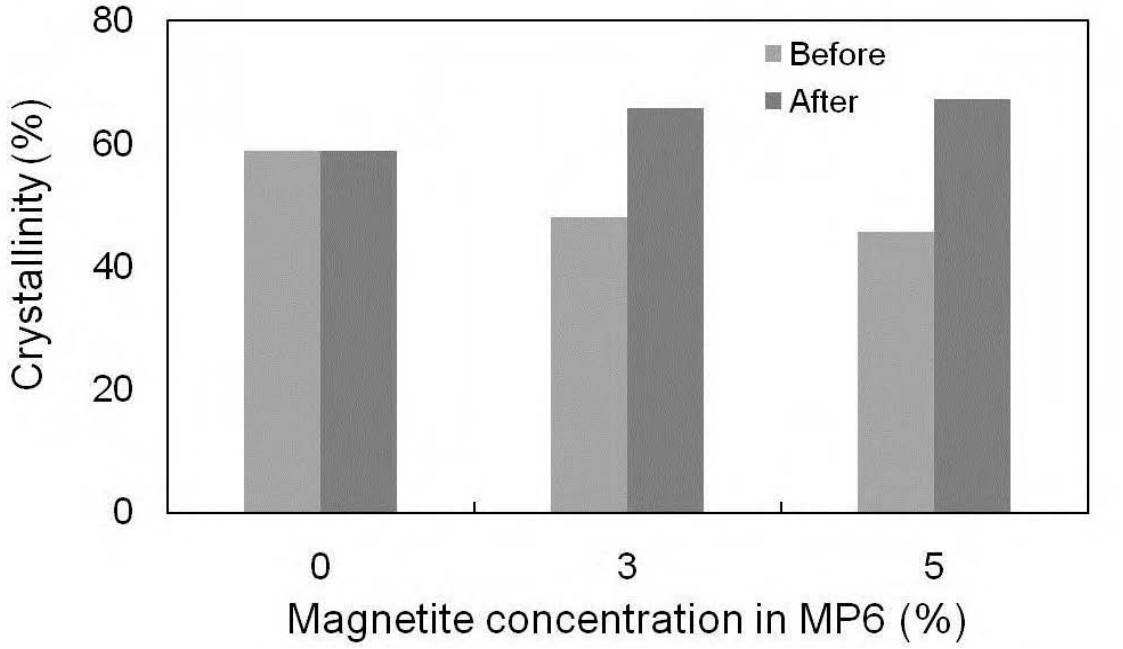


**Figure 9.11 Crystallinity changes of PCL6 and MP6 microspheres before and after AMF treatments.**

**Table 9.3 Thermal properties of PCL6 and MP6 microspheres before and after AMF treatments.**

| MP (%) | $T_m$ (°C) | | Crystallinity (%) | | Crystallinity change (%) |
|---|---|---|---|---|---|
| | No | AMF | No | AMF | |
| 0.0 | 58.1±0.3 | 58.1±0.3 | 58.9±0.2 | 58.9±0.2 | 0.0±0.0 |
| 3.0 | 53.9±0.8 | 58.0±0.6 | 48.1±1.8 | 65.9±7.7 | 37.0±15.0 |
| 5.0 | 56.3±0.8 | 62.1±0.4 | 45.6±2.1 | 67.2±0.3 | 47.4±6.1 |

Before the AMF treatment, the composite particles, 3 % and 5 % MP6, have a lower degree of crystallinity than the pure PCL6 demonstrated by the three light grey bars, shown in Figure 9.11. The degrees of crystallinity of the two MP6 samples (48.1 % and 45.6 % individually) are both lower than the degree of PCL6 (58.9 %). In addition, the melting point of two MP6 samples were 53.9 ℃ and 56.3 ℃ respectively, which are both lower than the melting point of PCL6 (58 ℃). This complies with the results for the MP2 microspheres were the heat conductivity of the encapsulated magnetite, which was improved and therefore leads to an earlier melting stage.

In Figure 9.11 and Table 9.3, the degree of crystallinity after treatment by the AMF exhibits marked differences in the results of 3 % and 5 % MP6, but not for the result of PCL6. The melting points and degrees of crystallinity of PCL6 (0.0 %) show a difference of less than 0.1 % between the AMF treated and non-treated samples. By contrast, after treatment by the AMF, there is a 37 % and 47.4 % increase in the crystallinity for the 3.0 % and 5.0 % MP6 samples, respectively. The increases are also apparent in the melting temperatures of the two MP6 specimens after the AMF treatment.

According to a report by a group of researchers, the highly ordered structures of polymers are strongly affected by thermal history and the crystallinity of PCL chains increases during heating (Hatakeyama *et al.*, 2000). An inference can be that there was a heating effect to the two types of MP particles during the AMF treatment. By contrast, the crystallinity of PCL6 shows no notable difference after the AMF treatment. The heat generated from the encapsulated magnetite can be linked to change in the thermal and crystal structure of the polymers.

The decrease in MP2 crystallinity after AMF treatment is assumed to be from the effects of conductor temperature. According to Figure 8.11 and Figure 8.12, the melting temperature of PCL2 particles is much lower than PCL6 particles. Although the melting point of PCL2 particles is 47 ℃, the melting process of polymer occurs in a relatively wide range compared to single domain materials (Kong and Hay, 2002). The earliest stage of PCL2 melting starts from 35 ℃ as seen in Figure 8.11, and the partial phase disturbance is assumed to have occurred earlier than the melting. Additionally, partially heated PCL2 can be observed after the AMF treatment even when the temperature of the conducted core is controlled at room temperature, as shown in Figure 9.12 (a). Figure 9.12 (b) shows no obvious morphological change in PCL6 particles after the AMF treatment. According to the recrystalline points of PCL2 and PCL6 (21 ℃ and 32 ℃ respectively) from DSC measurements (Figure 9.13), partially melted-PCL2 is not able to process the recrystallisation stage at room temperature over 22 ℃. This is possibly due to the crystallinity of PCL2 becoming lower after partially melting by the AMF treatment. The crystallinity of MP2 after AFM treatment has increased but which was not as high as the rising ratio of the two MP6 specimens (as compared Table 9.2 and Table 9.3). Therefore, the altered thermal properties of PCL2 after the AMF treatment indicate that the PCL2 has been affected by warming of the core.

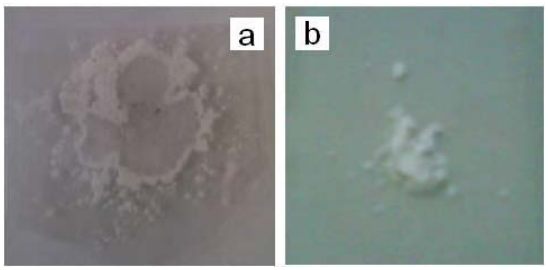


**Figure 9.12 Macrographs of the AMF treated (a) PCL2 and (b) PCL6.**

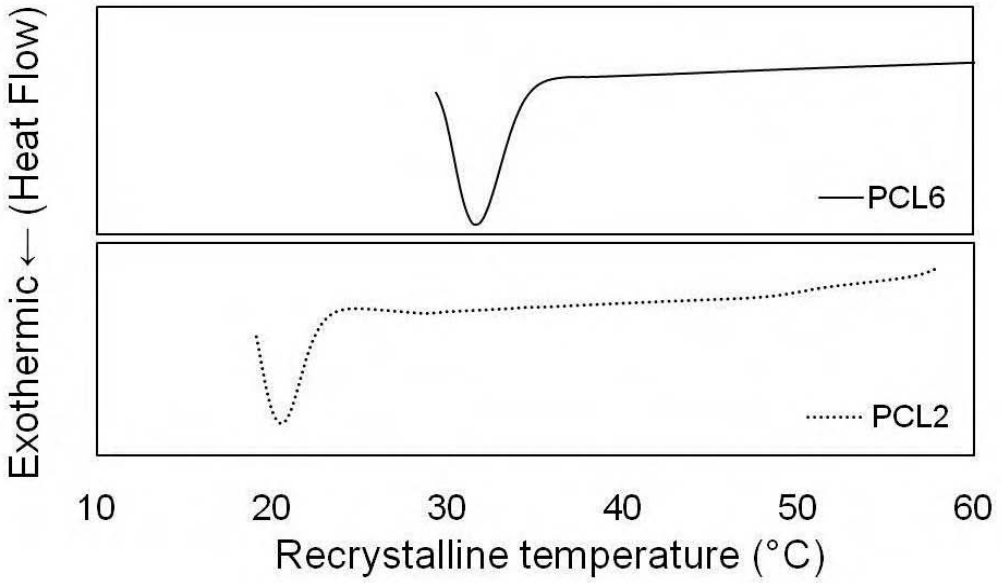


**Figure 9.13 Recrystallization of PCL2 and PCL6 during cooling process.**

In conclusion, a decrease in both the melting points and degrees of crystallinity, which was seen for exhibited in MP2 and MP6, respectively. These results are due to the encapsulation of magnetite nanoparticles in PCL, which change the thermal properties after loading the magnetite (Weidenfeller *et al*., 2002).

MP particles after heat treatment show morphological and crystallinity changes, which provide evidence of a phase change as a result of softened or melted structures. The main aim of this thesis is to produce softened PCL by the heat generated from the encapsulated magnetite by means of AMF treatment. The mechanism of heat generation by magnetite in AMF is still a point of scientific discussion. Hysteresis loss and relaxation loss are the two key factors of the heat generated by magnetite particles in an AC magnetic field (Hergt *et al*., 1998). The heating ability of larger magnetic particles (100 nm or larger) mainly results from hysteresis loss, which is

strongly size dependent (Kim *et al*., 2005). Ma and colleagues suggested that relaxation loss becomes more important for the heating from magnetite when the magnetite particle is smaller than 46 nm and has superparamagnetism (Ma *et al*., 2004). Larger magnetite particles (over 46 nm) exhibited size dependence on the hysteresis loss and therefore the temperature of magnetite particles. However, smaller magnetite particles (7.5 nm and 13 nm) exhibited very little hysteresis losses but higher temperature rising curves.

Néel relaxation and Brownian motion are the two phenomenon of energy loss of single domain particles, consequently resulting in particles heating. The magnetic moments of superparamagnetic particles rotate in an AC magnetic field, where the rotation of the particles overcome the energy barrier for reorientation. Therefore the energy is dispatched when the particle moment relaxes to its equilibrium orientation, which is known as Néel relaxation. Alternatively, the rotation of the entire magnetite particle in the AMF is called Brownian motion (Mornet *et al*., 2004). The heat generation in MP spheres is presumed to be from Néel relaxation rather than from Brownian motion because the magnetite was embedded in a solid phase with higher viscosity (compare to ferro-fluid), and subsequently, there was less space for particles to rotate (Kötitz *et al*., 1999). According to the report of Okawa, the heating ability of magnetite in agar gel is mainly from Néel relaxation and the Brownian relaxation is neglected due to the time of Brownian relaxation is much longer ($10^3$ times larger than the value of Néel relaxation) in the higher viscosity environment (Okawa *et al*., 2006).

### 9.3.4 Heat treatment by Mini-microwave

In order to show a change in temperature by the encapsulated magnetite particles during the heating process, the MP particles were heated by a mini-microwave. The relationship between the amount of encapsulated magnetite and the temperature difference was compared by observing the rising temperature by per unit of the specimen (mg). Figure 9.14 demonstrates the increase of temperature for PCL6 (0 %) and the two MP6 (3 % and 5 %) particles during the microwave heating process at 20 W for 20 seconds. The increasing rate of temperature of polymer is higher when more magnetite is encapsulated, for example, 0.5 ℃/mg, 0.7 ℃/mg and 1 ℃/mg for PCL6, 3 % MP6 and 5 % MP6, respectively.

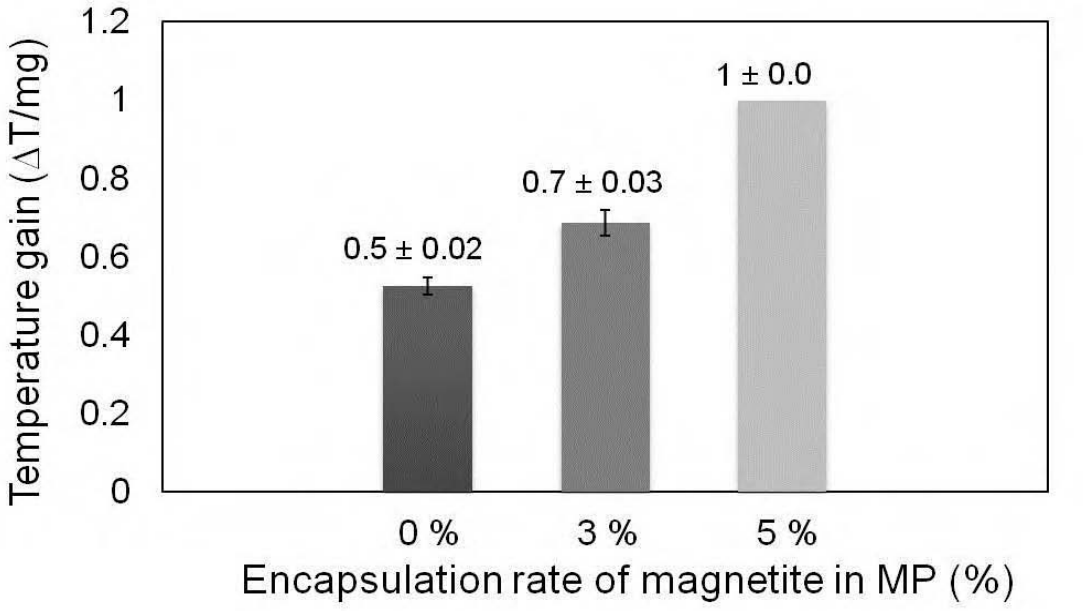


**Figure 9.14 Heating particles by mini-microwave at 20 W for 20 seconds.**

The heating effect of the encapsulated magnetite also exists in an altered power input in the mini-microwave. Figure 9.15 shows the change in temperature when the microwave was operated at 40 W for 47 seconds. The temperature increase with a higher power input was exhibited in all the specimens. By contrast, the two MP samples display an increase in temperature which was generally larger than the temperature increase of the PCL6 sample during the heating process. The rising temperature rates of PCL6, 3 % MP6 and 5 % MP6 are 6.6℃/mg, 6.1 ℃/mg and 8.1 ℃/mg, respectively. The temperature of MP spheres increased with the amount of encapsulated magnetite during the microwave heating. This phenomenon has been addressed in the literature as microwave absorption by iron compounds releases the energy to boost the heating process (Acierno *et al*., 2004). The microwave also offers an alternate method for melting polymers containing magnetite and the rise in temperature can be controlled by the mass of magnetite.

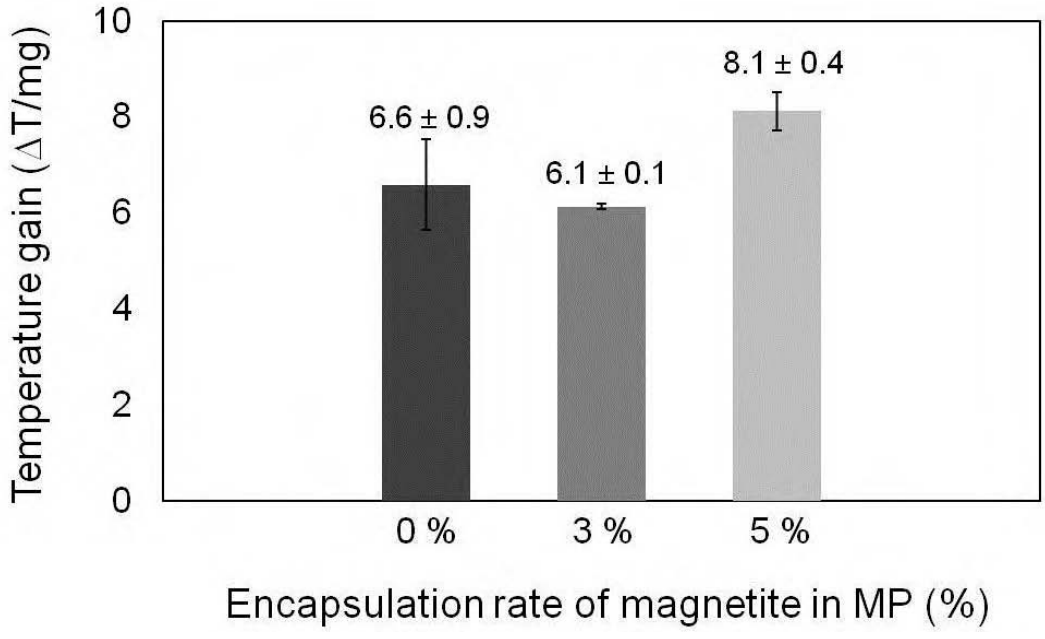


**Figure 9.15 Heating particles by mini-microwave at 40 W for 47 seconds.**

Figure 9.16 shows micro-CT images of the resultant polymers after the heating process by microwave; (a) shows the melted agglomerate of MP6 and (b) the two images from the layered scans. The microspheres melted and cohered after heat treatment by microwave. Figure 9.16 (b) shows the two major colours, orange and purple indicating PCL and magnetite, respectively (same colour index as Figure 9.7 (a)). This is similar to the results of AMF treated MP spheres in Figure 9.8, the orange area is more prominent than the non-heated particles (shown in Figure 9.7 (c)) and the purple spots gathered within the compounds.

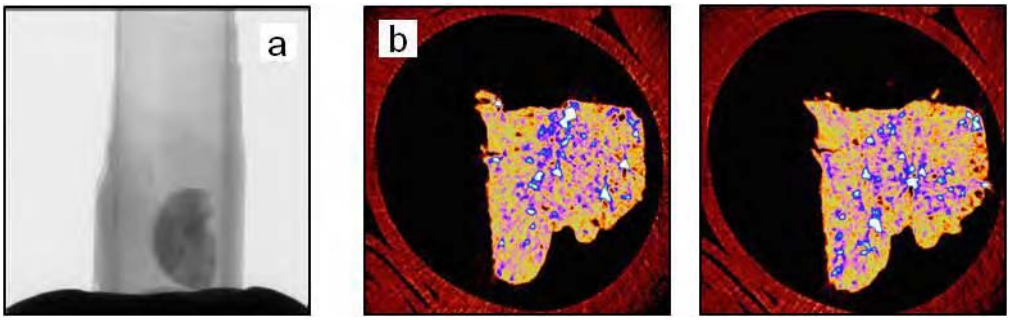


**Figure 9.16 MP microspheres after microwave heat treatment (a) agglomerate of MP, (b) upper and (c) lower layers of micro-CT scan.**

The Micro-CT images of MP6 particles treated by the mini-microwave and the AMF exhibited the same results that particles agglomerated due to the polymer melting. This is further evidence of demonstration that the MP particles have been successfully softened or melted during the AMF treatment.

## 9.4 Conclusion

The macrographs showed that the MP particles agglomerated after AMF treatment and that there was same structural disruption of MP particles. An altered thermal property of polymer is important evidence of melting and phase change in a polymer. After the formulation of MP microspheres, the decrease in melting point and the degree of crystallinity indicated the successful of encapsulation magnetite nanoparticles in PCL2 and PCL6, respectively. After AMF treatment, the altered thermal properties and the degree of crystallinity proved that there was a heating effect to MP2 and MP6 during the AMF treatment, and the heating is assumed to be from the embedded magnetite due to the comparisons of PCL2 and PCL6. The thermal property of PCL6 has no notable change after the AMF treatments, but the degree of crystallinity of PCL2 was slightly altered by the warming core, which can be observed from the image with partially phased change (as seen in Figure 9.12).

The uniform AMF (20 Hz, 20 V, 1 hour) successfully derived the magnetic field to induce the magnetite heating. The heating of magnetite nanoparticles in the AMF is suggested to be from Néel relaxation. Compared to the reported AMF with the sample space in a water-based area (Ma *et al*., 2004; Kim *et al*., 2005), the uniformed AMF in this thesis is advantageous in that magnetic materials can be treated in a dry environment, and therefore the melted polymers can be filled into a defect within a sufficient mouldable time. The other advantage of this AMF system is the low power requirement (20 Hz and 20 V), compared to devices that use power input up to kilo-Hz for penetrating depth *in vivo* (Ito *et al*., 2002; Asmatulu *et al*., 2005). The low power requirement AMF is beneficial for cost and for open injury, for example, bone trauma. To

conclude, MP microspheres can be used to soften PCL polymers by AMF and enable them to be potentially used as bone trauma filling.

# Chapter 10 Drug release of MP microspheres with/without AMF treatment and the microbiology activity after release

## 10.1 Introduction

The second objective of this thesis is to soften MP particles and release drugs from the MP microspheres, as described in Chapter 5. Therapeutic treatment using drug release of polymeric system, which reduce side effects and enhance efficacy is advantageous than the injection method and controllable dose and rate (Richardson *et al*., 2001). Polylactic acid derived polymer, for example, PCL, is interesting due to its biocompatibility and degradability, which has been well investigated of many types of scaffolds and biomaterials using as a drug carrier (Habraken *et al*., 2007, Wang, *et al*., 2007).

Hyperthermia combining drug release of magnetite composites have attracted interest and is under development by many research groups (Yang *et al*., 2006, Babincova *et al*., 2001). In addition, Gentamicin is one of the commonly used aminoglycosides as antibiotics in anticancer therapy, which is heat stable and is able to kill most of the gram-positive and some gram-negative bacteria (Yoshizawa *et al*., 1998, Casemore, 1967).

The uniform AMF was used to induce the polymer softening by the magnetite heating and consequently carrying out the release of the encapsulated gentamicin.

## 10.2 Materials and Methods

The first two parts of this section describe the preparation of drug-loaded particles and the drug evaluation method. This is followed by the gentamicin drug release with and without AMF treatments. The heat treatment by AMF is using the identical condition from Chapter 9. Finally, the microbiological activity of the gentamicin loaded spheres is used to illustrate the efficacy of the AMF -treated drug loaded MP spheres.

### 10.2.1 Preparation of gentamicin loading MP microspheres

The preparation of gentamicin loaded MP microspheres (GMP) is similar to the formulation of MP microspheres in section 8.2. A mixture of water dispersed magnetite and gentamicin sulphate (GS) (10 mg) (Sigma) was added into a solution of PCL dissolved in dichloromethane. The resultant liquid was sonicated for 5 minutes and followed by high speed mixing (23.6 Np) into 2 % PVA solution to form w/o/w emulsion. The rest of the procedures are same as described in section 8.2.

### 10.2.2 Evaluation of encapsulation rate and GS release of GS in GMP spheres

The fluorescence method is the most common assay for GS evaluation. The basic theory is to determine the UV absorption of a fluorescent isoindole resulting from the reaction between the amino groups in the gentamicin molecule and o-phthaldialdehyde (OPA) (Chang *et al*., 2006). Gubernator and colleagues have reported a simple and sensitive method for gentamicin evaluation, which was used to evaluate the GS released from GMP particles in this thesis (Gubernator *et al*., 2006). The first step in this assay is to prepare the OPA reagent; 0.5 ml of

methanol was used to dissolve 0.1 g of o-phthaldialdehyde (Sigma), and then 9.5 ml of 0.4 M boric buffer at pH 10.4 was added and mixed. 0.2 ml of 2-mercaptoethanole was added and the resultant solution was adjusted to pH 10.4 by neat potassium hydroxide (Sigma). The boric buffer was prepared by mixing 24.7 g of boric acid (Sigma) in 900 ml of distilled water, and kept at 4 ℃ after adjusting the pH to 10.4 by neat potassium hydroxide. The OPA reagent is stable at 4 ℃ for only 2 to 3 days, thus fresh OPA reagent was prepared every two days in this research.

Once the OPA reagent is ready to use the following procedures were undertaken. First, 0.85 ml of distilled water was used to form 1 ml aliquot with 0.15 ml of specimen and was followed by mixing with 0.6 ml of methanol. 0.1 ml of OPA reagent was added into the sample and vigorously mixed. The resultant solution was incubated for 10 minutes at room temperature before measurement. UV absorbances of samples were measured by a UV spectrophotometer (Uvikon 922, Kontron Instruments, Northstar Scientific) at 332 nm. A calibration curve was built using gradient concentrations from 0.5 μg to 4 μg of GS. The determination coefficient ($R^2$) of the calibration curve is 0.97 as shown in Appendix 12.2

To determine the encapsulated GS, 10 mg of GMP microspheres were dissolved in 5 ml dichloromethane and the drug was extracted by 10 ml of 0.01 M phosphate buffer solution (PBS, Sigma). The resultant liquid exhibited two phases following 5 minutes sonication, as shown in Figure 10.1. The upper layer was the aqueous phase of the extracted GS in the PBS solution, and the bottom layer was the organic solvent, dichloromethane, and the dissolved PCL. The magnetite nanoparticles represent brown colour at the interface, which also another provides evidence that the MP microspheres had been incorporated into the formulation. The aqueous

solution was collected from the upper layer liquids and was stored at 4 ℃ prior to the quantitative by OPA assay.

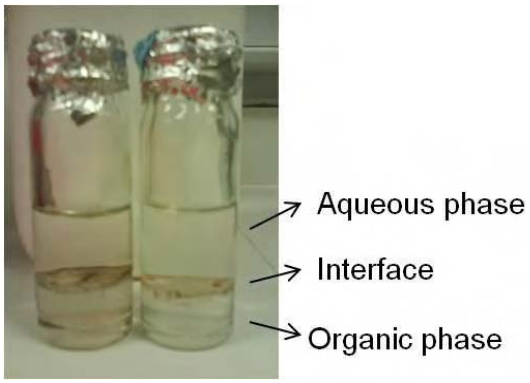


**Figure 10.1 GMP microspheres after dissolving in dichloromethane to evaluate the release of GS in PBS.**

### 10.2.3 GS release and heat treatment

The drug release from GMP loaded microspheres was assessed with and without AMF treatment. AMF treatments were undertaken at the identical conditions in Chapter 9, at 20 Hz and 20 V for one hour. The AMF-treated and non-treated GMP microspheres were immersed in 3.5 % (w/v %) PBS solution and were retained in a 37 ℃ shaker during the period of drug release. An immersed aliquot (150 μl) was taken for release evaluation at time intervals (24 hours) and refreshed using the same amount of PBS solution (Wang *et al*., 2007).

### 10.2.4 *In vitro* evaluation of microbiological activity of released gentamicin

One of the important factors of drug release work is the maintenance of the bioactive molecules entrapped in the polymeric matrix (Chang *et al*., 2007). *E. coli* (10,000 NCIMB Ltd., UK) was

selected as a pathogenic microorganism to demonstrate the antibacterial activity of the released gentamicin.

Using a sterile loop, *E. coli* was transferred into sterile nutrient broth (CM0067, Nutrient Broth No. 2, Oxoid Ltd., UK). The broth was incubated at 37 ℃ for 24 hours prior to being diluted of $10^{-4}$ times. 200 µl of the dilution culture was spread evenly onto a nutrient agar plate (BO0336, Oxoid Ltd., UK) and after 10 minutes setting time a GS-loaded paper disk (13 mm) was placed in the centre. The GS-loaded paper disc had been prepared from 30 µl of the immersed aliquot (section 10.2.3) which was allowed to soak onto the paper disk before being placed in the agar plate with *E. coli*. The drug release rate and antibacterial efficacy were compared for GS from non-treated and AMF-treated GMP microspheres on the first day of release. Drug free PBS solution was used as a control for the microbiological activity.

## 10.3 Results and Discussions

This result section includes four parts: the morphologies of the formulated GMP microspheres, the quantification of the encapsulated GS, the drug release measurement, and investigation of the antibacterial ability of the released GS.

### 10.3.1 Morphology of the GMP microspheres

The morphology of the GMP microspheres were assessed by ESEM and EDS for composition analysis. The GMP microspheres appeared spherical in shape. The GMP spheres in Figure 10.2 (a) shows in uniform shape and are similar size as MP microspheres (shown in Figure 8.8), (b)

shows a single sphere with rough surface. The GMP spheres exhibit polydispersion (seen Chapter 8) as seen in Figure 10. 2 (c), and the broken domain, (d), was used for compounds analysis by EDS.

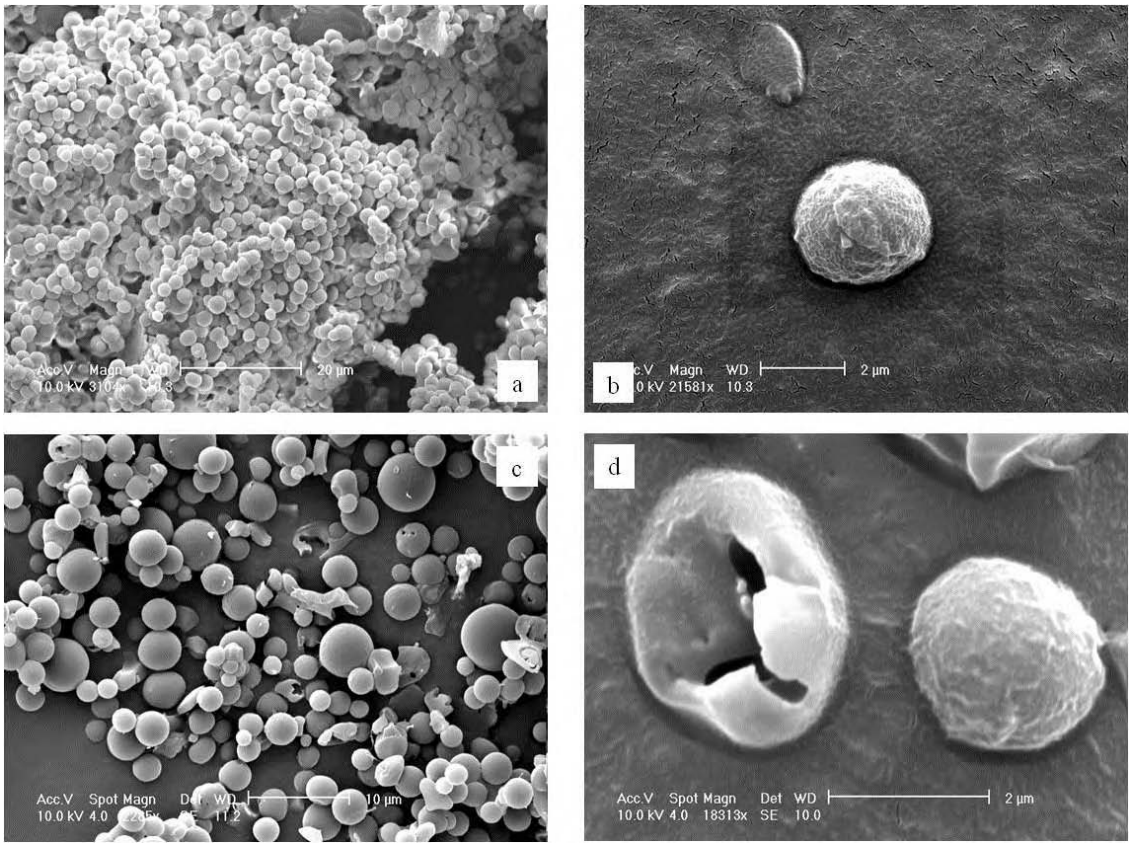


**Figure 10.2 Morphologies of GMP microspheres, (a) collection of GMP, (b) single GMP microspheres, (c) microspheres exhibit polydispersion and (d) broken microspheres for EDS measurement.**

Figure 10.3 show micrographs of spheres used for elemental analysis by EDS. 2.67 % of nitrogen and 0.56 % of iron was detected in (a), single GMP sphere; and 1.03% of nitrogen and 1.36 % of iron in the collection of GMP microspheres. The existence of nitrogen was assumed to be from the encapsulated gentamicin (formula of Gentamicin, $C_{21}H_{43}N_5O_7$). However, the elemental

analysis by EDS is not quantitatively precise as discussed in the section 8.3.4 (Buck *et al*., 2004). Nevertheless, the results of EDS display the presence of nitrogen from the encapsulated GS and iron from encapsulated magnetite. Further accurate composition analysis of GMP can be undertaken by chemical method, for example, OPA assay.

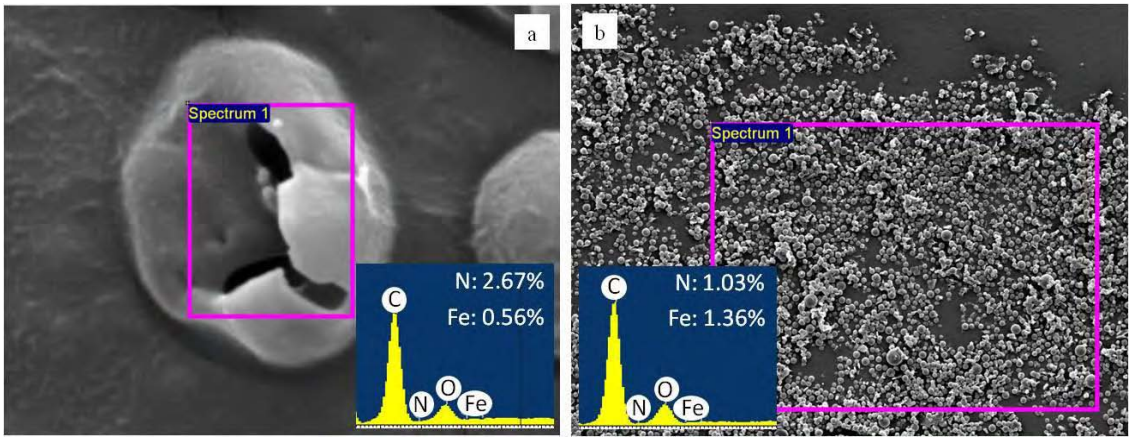


**Figure 10.3 Elemental results of GMP microspheres at (a) single sphere and (b) collections of microspheres.**

In conclusion, the resultant morphologies of GMP particles have no obvious difference between the drugs free MP and the PCL microspheres. All spheres are spherical in shape and have a slightly rough surface. In addition, the GMP particles exhibited a polydispersed size distribution, which similar to the polydispersed PCL microspheres in Chapter 8. As discussed in section 8.3.1, the stabilizer was suggested to be a key point of size effects, which was confirmed by other reports of gentamicin-loaded PCL particles. The concentration and type of stabilizer play an important role in the size distribution of PCL and PCL composites (Chang *et al*., 2006; Blanco-Prieto *et al*., 2002).

### 10.3.2 Encapsulation rate of gentamicin in GMP microsphere

Loading efficiency is one of the important criteria for the development of a drug delivery system. The encapsulation efficiency of GS in GMP particles and its release were assessed using OPA fluorometric assay as described in section 10.2.1 (Gubernator *et al*., 2006).

Table 10.1 shows the encapsulation loading and efficiency of GS within GMP microspheres. The concentration of PCL solution was obtained from the constant ratio (3 %) of the weight of PCL and the volume of dichloromethane. The initial loading rate of GS, 3.3 %, is calculated from the weight ratio of GS and PCL. To obtain the resultant GS loading rate, the formulated GMP particles were dissolved in dichloromethane and the encapsulated GS was extracted by PBS solution followed by determination by OPA assay. The weight ratio of encapsulated GS in the GMP microspheres was then calculated (fourth column in Table 10.1). The encapsulation efficiency was calculated by the weight ratio, which was the ratio that the actual encapsulated GS amounts and the initial loading GS amounts.

**Table 10.1 Drug loading efficiency of GS in GMP microspheres**

| | PCL solution concentration (% w/v) | Initial GS loading (% w/w) | Resultant GS loading (% w/w) | Encapsulation Efficiency (EE), (%) |
|---|---|---|---|---|
| GMP2 | 3 | 3.3 | 2.12 ± 0.36 | 63.66 ± 11.00 |
| GMP6 | 3 | 3.3 | 3.28 ± 0.85 | 98.50 ± 25.53 |

According to GS determination by OPA assay, the results in Table 10.1 indicated the successful of encapsulation of GS within the MP microspheres. GMP6 microspheres were found to have more GS loaded and therefore higher EE value than GMP2 microspheres. The production of GS loaded PCL relies on the sufficient adhesion offered by the polymer. Raising the viscosity of the polymer is necessary for to avoid phase separation under gravity, such as encountered in the centrifugation process (Chang *et al*., 2006[2]). The viscosity of PCL2 (480 mPas at 60 ℃) is approximately 20 times lower than the viscosity of PCL6 (9300 mPas at 100 ℃) as shown in Table 8.1. The relatively low EE rate of GMP2 was assumed to be from the lower viscosity of PCL2 which has less ability to entrap the drug during formulation. In addition, the highly hydrophilic GS tends to lead into the water phase during solvent evaporation in the GMP formulation (Naraharisetti *et al*., 2005). The combination of low viscosity of PCL2 and the hydrophilic GS leads to the relative low encapsulation rate of GS in GMP2.

### 10.3.3 AMF treatment and drug release

To the achievements that MP particle softened by magnetite heating in the uniformed AMF and the successfully synthesised GMP microsphere, inducing of drug release by the AMF treatment was carried out. The release of GS has three major release stages, burst release of rapid diffusion, swelling of shapes and hydrophilic behaviour of GS and finally, gradual release as a result of polymer degradation (Silva *et al*., 2007). The values of GS release were determined by the weight ratio (μg/mg) of GS to GMP, by the cumulative release rate and the release amount by daily evaluation. The GS release presented by weight ratio can be easily applied to dosage evaluation for *in vitro* and *in vivo* study in the future.

In Figure 10.4, the GS amounts released from GMP2, exhibit the burst release in the first three days after AMF treatment, the release amounts were approximately 80 μg/mg. After the burst release phase, the cumulative curve indicates an incremental release trend, between days 3 and 7, prior to reaching the plateau region, after 7 days maintained at 37 ℃. The GS release after one week, from days 8 to 10, is shown by plateau region of the cumulative release and implies was drug release.

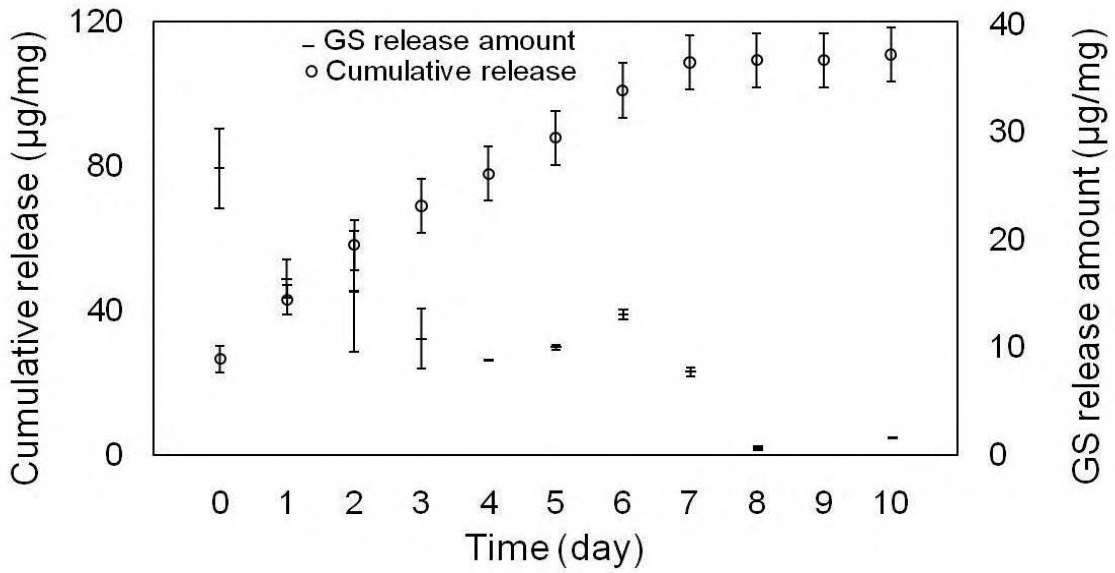


**Figure 10.4 GS release from GMP2 spheres after AMF treatment immersed in PBS at 37 ℃ for periods up to 10 days (n = 6, mean ± SD).**

The GS release from GMP6 is shown in Figure 10.5. Similar to the results of the GS released from GMP2, the amounts of the released GS in the first two days were relatively higher than the release amounts in the following week. By contrast, the first day release of GS from GMP6 was approximately 100 μg/mg which was much higher than the value of GMP2 (80 μg/mg). In addition, the cumulative release curve of GMP6 indicated that the first two release stages of

GMP6 tended to finish on day 8 but still showed higher values than the GS release from GMP2 released GS at that stage.

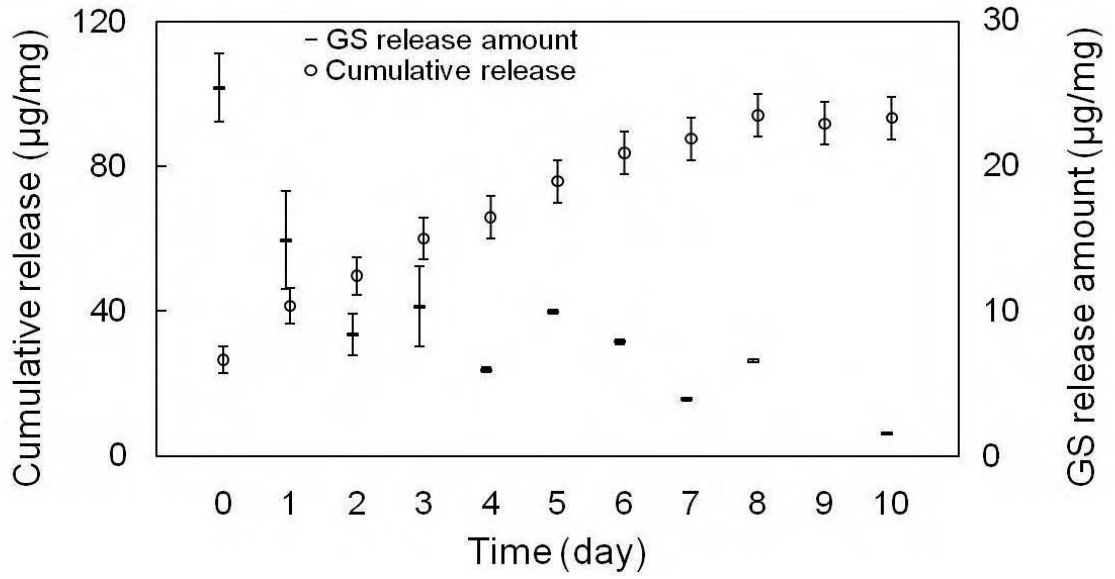


**Figure 10.5 GS release from GMP6 spheres after AMF treatment immersed in PBS at 37 °C for periods up to 10 days (n = 6, mean ± SD).**

A major burst release of GS from GMP2 and GMP6 can be observed in the first 3 days, as seen in Figure 10.4 and Figure 10.5, respectively. In comparison to the results of GMP2 microspheres, GMP6 microspheres released more GS in the initial burst state and at the end of the first two release stages. This assumed to be or the higher encapsulation rate of GS in resultant GMP6 particles (Blanco-Prieto *et al*., 2002; Virto *et al*., 2003).

To further understand of the influence of AMF on drug release profile, GS released from GMP2 and GMP6 microspheres without AMF treatment were investigated at 37 °C. In Figure 10.6, the first burst phase lasted the first two days for GMP2, which is similar to AMF-treated results, but

the value of burst release was much lower. There was 45 μg/mg of GS released on the day zero of the *in vitro* assay, which was almost half the value of the GS released from AMF-treated GMP2 and GMP6 (80 μg/mg and 100 μg/mg respectively). The release behavior displayed a gradual reduction in the amount of GS, which maintained prolonged release after 8 days and will still had a GS release value of approximately 18 μg/mg. The GS value for the plateau region was stable at 60 μg/mg as by, which is also almost half the value of the AMF-treated GMP2.

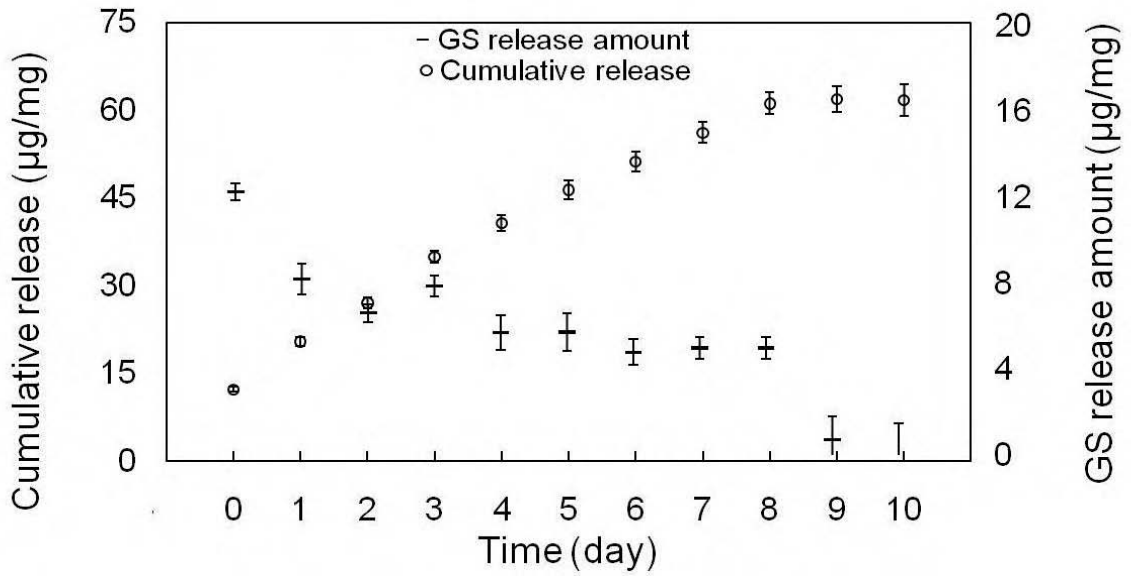


**Figure 10.6 GS release from GMP2 spheres and immersed in PBS at 37 °C for periods up to 10 days (n = 6, mean ± SD).**

GS release results for non-AMF treated GMP6 are shown in Figure 10.7. The first burst phase still occurred on the first two days, and the value of burst release stage was similar to the value of non-AMF treated GMP2 (Figure 10.6). The values of the cumulative release once the time period also indicated a slow release of GS, GMP6 microspheres still showed the ability to release GS

approximately 13 μg/mg after 9 days at 37 ℃ storage, which was higher than AMF-treated GMP6 and GMP2 and non-treated GMP2 particles at the same time point. The GS value of the plateau region (approximately 65 μg/mg) was slightly higher than the value of GMP2 (Figure 10.6), but was lower than the value of GS released from the AMF-treated GMP microspheres.

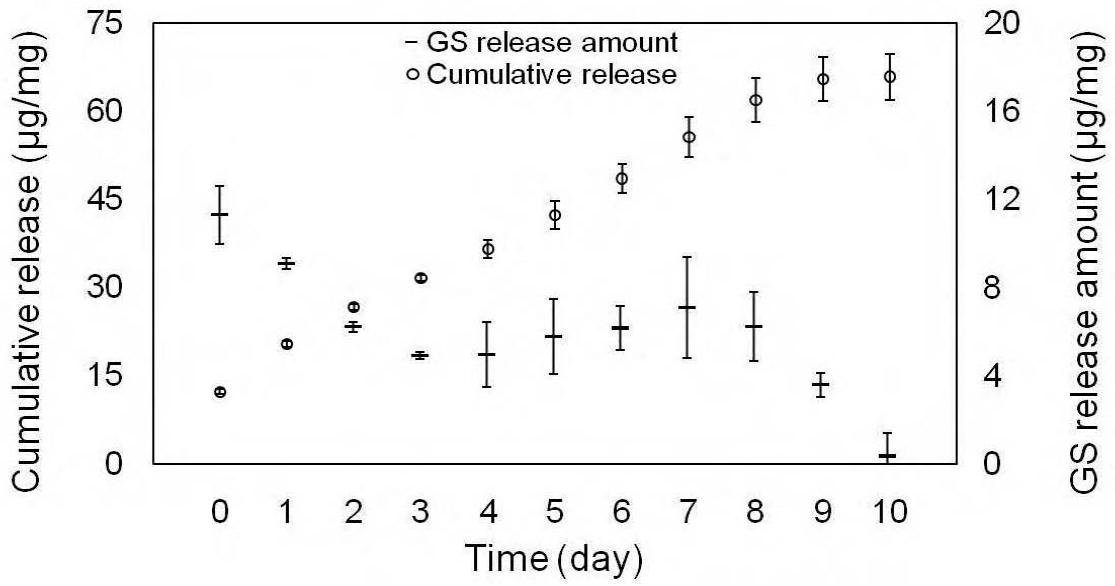


**Figure 10.7 GS release from GMP6 spheres immersed in PBS at 37 ℃ for periods up to 10 days (n = 6, mean ± SD).**

GMP microspheres with AMF treatments had more GS released in the burst stage, and the AMF-treated GMP6 microspheres released more GS than AMF-treated GMP2 microspheres due to the higher EE rate. It is interesting to note that the burst release value for GS from non-AMF treated GMP6 and GMP2 microspheres were similar, but in the slow release stage (the plateau region) GMP6 released more GS. By contrast to GMP2 microspheres, the GMP6 microspheres had greater GS encapsulation efficiency and exhibited more GS released during the first release stage

after AMF treatment, but the non-AMF treated GMP6 microspheres showed more GS release at in the second stage of release. This confirms that microspheres containing more drug resulted in higher release rates as shown in Figure 10.5.

To conclude, the increasing GS release prior to the plateau stage is suggested to be due to GS close to the polymer surface, which was extracted by water during phase immersion due to the hydrophilic nature of GS (Silva *et al*., 2007). The final release stage as a result of polymer degradation cannot be seen in the ten day period as the degradation time of PCL is relatively long, which can be from weeks up to years, as reviewed in Chapter 3. AMF treatment was assumed to increase the first stage of burst release and the rapid diffusion of GS to the PBS solution. AMF treatments caused damage to the polymer (as shown in Figure 9.9 and discussed in the section 9.3), as a result of by magnetite heating and resulted in a higher permeability of GS in the immersed solution.

There was no notable difference in the burst release of GS from non-AMF treated GMP2 and GMP6 microspheres. Virto *et al* have reported that for *in vitro* testing in a highly hydrophobic polymer, the entrapped antibiotics will not be entirely released out (Virto *et al*., 2003), therefore, the drug release induced by the magnetite heating in the AMF is advantageous for enhancing the release of encapsulated drugs.

### 10.3.4 Effects of storage at different temperature on the GS

The storage condition of GS is ather factor to consider to maintain the drug activity and remanence. The efficacies of GS were undertaken using the GS buckl solution (0.1 μg / ml) for two storage conditions, 4 ℃ and 37 ℃. The GS solution preserved at 4 ℃ maintained drug activity after storage for one month as shown in Figure 10.8, whereas the GS solution at 37 ℃, exhibited a reduction in activity after 5 days. Although, gentamicin is reported as a thermally stable antibiotic(Casemore, 1967), the drug activity decreased to half after 32 days at 4 ℃ and 6 days at 37 ℃. The activity reduction of GS can be another factor or the reduction of GS from both the AMF-treated and non-treated GMP microspheres after a week in the PBS solution at 37 ℃.

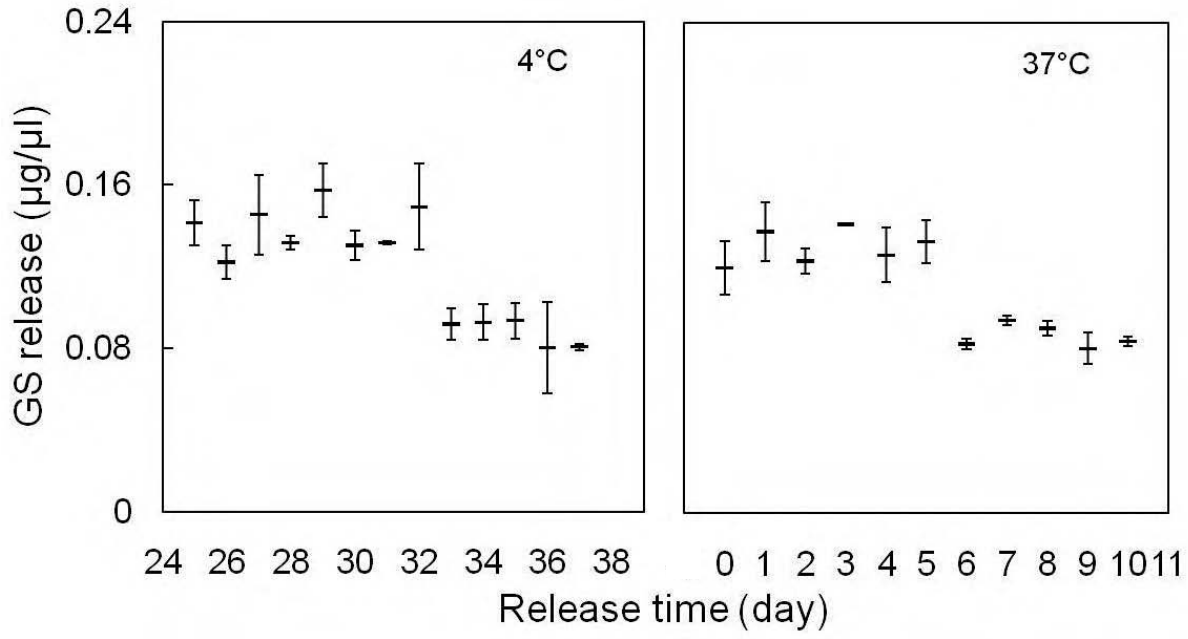


**Figure 10.8 Temperature effects on GS activities. Gentamicin concentration of 0.1 μg/ml PBS at 4 °C and 37 °C for 37 days and 10 days respectively.**

### 10.3.5 Microbiology activity test

The GMP loaded microspheres were shown to successful release of GS, and the efficacy of the GS was assessed on a bacterium. The first day release of GS from non-treated GMP microspheres and AMF-treated GMP microspheres was used to observe its effects on the inhibition zones formed by *E. coli*. The zone size of the control specimen (GS solution alone) was used as a standard for comparison. The zone size is the ratio of the diameter of the zone of inhibition and the diameter of the plate. In Formula 10-1, $D_C$ is the diameter of the inhibition zone of the control and $D_P$ is the diameter of the plate. The resultant zone areas of GMP microspheres with or without AMF treatments were compared. The zone size was the ratio of Zone diameter and $Zone_C$ as is calculated by Formula 10-2. All the diameters of the inhibition zones were measured by Image J software and the statistical values are shown in Table 10.2. Group A is for GS released from non-treated GMP microspheres using an *E. coli* culture concentration of 1.55 x $10^5$ CFU/ml. Group B and C are for he studies of the microbiological activities of the GS antibiotic for AMF-treated GMP microspheres. The concentration of *E. coli* culture for group B and group C were 1.3 x $10^4$ CFU/ml and 4 x $10^5$ CFU/ml, respectively.

$$\mathrm{Zone_C} = (D_C/D_P) \qquad 10\text{-}1$$

$$\text{Zone area} = \frac{(D_S/D_P)}{\mathrm{Zone_C}} \qquad 10\text{-}2$$

The control specimen (GS stock solution preserved at 4 ℃) represented the maximum antibacterial ability for all three groups. The ratio of inhibition zone size was almost constant at a value of approximately 10. In group A, the GS concentration of the control specimen was 0.7 μg /

μl, and both the GS release amount from GMP6 and GMP2 microspheres was 0.02 μg / μl, as shown in Table 10.2. The released GS from GMP6 microspheres exhibited drug activity and gave a zone size ratio of 4.4. However, the released GS from GMP2 microspheres had the same initial amount of GS but did not maintain drug activity. After the AMF treatments, the GS released from both GMP2 and GMP6 microspheres was slightly higher (0.04 μg/μl to 0.03 μg/μl) than non-AMF treated GMP microspheres as seen in the results for group B and group C.

Furthermore, GMP2-released GS displayed antibacterial activity and gave an inhibition zones a ratio of 3.5 for a bacterial culture with lower concentration (1.3 x $10^4$ CFU/ml). On the other hand, for the same concentration (0.04 μg / μl) of GS released from GMP2 microspheres the drug activity could not maintain for the higher concentration of bacterial culture (4 x $10^5$ CFU/ml). The GMP6-released GS exhibited drug efficacies and the inhibition zones of *E. coli* were demonstrated for the two concentrations of cell culture for 1.3 x $10^4$ CFU/ml and 4 x $10^5$ CFU/ml, respectively. The GS concentration released from the AMF-treated GMP6 (0.03 μg / μl and 0.04 μg / μl, group B and C) was almost half of the GS values of the control specimen (0.06 μg / μl), and therefore the inhibition zones obtained were approximately half of the ratio of the control.

**Table 10.2 Inhibition zones of GMP microspheres from with or without AMF treatment.**

| A | Non treatment / 1.55 x $10^5$ CFU/ml | | |
|---|---|---|---|
| | Control | GMP6 | GMP2 |
| GS (μg/μl) | 0.07 | 0.02 | 0.02 |
| Zone area (ratio) | 10 ± 0.1 | 4.4 ± 0.0 | 0.0 ± 0.0 |
| B | AMF Treated / 1.3 x $10^4$ CFU/ml | | |
| | Control | GMP6 | GMP2 |
| GS (μg/μl) | 0.06 | 0.03 | 0.03 |
| Zone area (ratio) | 10 ± 1.1 | 4.4 ± 0.2 | 3.5 ± 0.3 |
| C | AMF Treated / 4 x $10^5$ CFU/ml | | |
| | Control | GMP6 | GMP2 |
| GS (μg/μl) | 0.06 | 0.04 | 0.03 |
| Zone area (ratio) | 10 ± 1.4 | 4.9 ± 0.3 | 0.0 ± 0.0 |

The inhibition zones of *E. coli* at a cell concentration of $4x10^5$ CFU/ml exhibited after the incubation at 37 °C for 24 hours, shown in Figure 10.9. In Figure 10.9, (a) shows the inhibition zones obtained from the cell culture ($4x10^5$ CFU/ml) for the control specimen (0.06 μg/μl of GS), (b) shows the resultant inhibition zones (4.9, 0.04 μg/μl) for the AMF-treated GMP6 microspheres and (c) shows the inhibition zones (0, 0.03 μg/μl) from a *E. coli* culture (1.3 x $10^4$ CFU/ml) for the AMF-treated GMP2 microspheres.


**Figure 10.9 Inhibition zones of *E. coli* shown after 24 hours incubation by (a) 0.06 µg/µl Gentamicin (control specimen), (b) 0.03 µg/µl GMP6 microspheres and (c) 0.03 µg/µl GMP2microspheres.**

GS from the burst release phase of the GMP microspheres displayed bactericidal activity against *E. coli* and was concentration dependent on both the bacterial culture and the drug loading.

The effects of aminoglycoside antibiotics against microorganisms have been investigated. The clinically important aminoglycoside, gentamicin, is able to bind directly to ribosomal RNA and cause decrease in translation and inhibit translocation of the ribosome of bacterial (Yoshizawa *et al*., 1998, Casemore, 1967). For both AMF-treated and non-treated GMP microspheres, the inhibition zones of *E. coli* indicated the resultant GMP microspheres maintained the efficacy of the released GS.

## 10.4 Conclusion

According to the morphologies of the GMP particles, the loading GS did not exhibit significant effects on the shape and size of microspheres in the compares of MP particles. The results of elements analysis indicated the success of GS encapsulation in MP particles due to the presence of nitrogen (shown in Figure 10.3), and which was further confirmed by the evaluation of GS by the OPA assay, as seen in Table 10.1. Consequently, the formulated GMP microspheres were placed in the uniformed AMF with the identified condition (Chapter 9), which was followed by the study of drug release and morphology observation.

As expected, the AMF-treated specimen showed higher GS release rates then non-treated specimen, which were 80 μg/mg to100 μg/mg and 45 μg/mg of the release amounts on the day zero. Moreover, the encapsulation rate was suggested to be affected by the viscosity of polymers, which is expectably resulted in higher value of drug release (Chang *et al*., 2006). As discussed in the section 10.3.2, there were more GS encapsulated within the GMP6 (98.50 %) than the GMP2 (63.66 %) particles while the loading amount of GS is constant, and the viscosity of PCL6 is approximately 20 times higher than PCL2. Finally, the released GS demonstrated the drug efficacy by the inhibition zones formed by *E. coli*, shown in Figure 10.9. The AMF-treated magnetic polymers offer a new method for drug release of wound healing and cancer treatments.

# Chapter 11 Conclusion and Future work

Material and properties

This research is focused on two major sections, production of magnetite nanoparticles and MP microspheres; and the application of the latter to bone replacement. Both magnetite and PCL can be produced in different sizes ranges. Magnetite and PCL were successfully combined to form MP microspheres. The two types of PCL microspheres produce in a regular spherical shape at different mixing conditions. The micro-CT X-ray images show two major densities in the MP sample indicating that magnetite has been incorporated into the PCL microspheres. This will be used for further research into the rheology and magnetic properties of the melted MP compounds.

Coating agents bring some benefits for magnetite particles, like protection from particles adhesions, controlling pH values and ionic strength and functionalised (Tombacz *et al*., 2006). This may be a great idea, which can be implemented in this study, in the emulsification process of magnetite nanoparticles into PCL, and the particle of MP could be used in further applications such as drug delivery and target adhesions; however much more work would need to be done in this area. In addition, magnetic device for magnetite selecting could reduce the undesired particles, such as oxidised or lower magnetic saturation; which could guarantee uniform and narrow distribution of magnetic particles for further applications.

MP microspheres can be synthesized into different types of biomaterials by different formation methods with other polymers, such as sponges and scaffolds. Moreover, the research will investigate the incorporation of different bone materials, for instance, hydroxyapatite and β-TCP,

which enhance the architectural substitute. Polymer and ceramics composites with magnetite offer the degradable scaffold (polymer) for drug delivery and the sustained structure (ceramics) for bone replacements and tissue engineering. Magnetite containing brushite was reported having ability of hyperthermia of killing cancer cell and without normal cells damaging (Hou *et al*., 2009). Moreover, this ceramic composite has been used for drug delivery (Habraken *et al*., 2007)

In addition, multi-domain magnetic particles (not pure magnetite) shows greater rate of specific loss power, which has a result of much heating generated. This provides an efficient method for hyperthermia. For example, after AMF treatment for 15 minutes (at 7 mega Hz), the ferrite particles, $BaFe_{12}O_{19}$ and $SrFeO_{19}$ had temperature increasing rate ($\Delta T$) of 47.6 K and 62.7 K, both were higher than the $\Delta T$ of magnetite, 4.3 K (Kim *et al*., 2005).

Moreover, the thermal behaviour of magnetite nanoparticles and MP microspheres were measure by DSC with a heat rate of 10 ºC/min. Slowing done the heat rate from 10 ºC/min to 1 ºC/min might be an idea to the observation of thermal conductivity between nanomagnetite and surrounding PCL.

Thermal treatments with alternative magnetic fields

Because the magnetite nanoparticles can be encapsulated into PCL, which showed good dispersion inside the microspheres, it is expected to generate heat to surrounding PCL. Heating with a microwave indicated that heat can be transferred to the PCL which cause it to melt. That can supply magnetism to rotate the encapsulated magnetite inside the microspheres and induce melting. However, microwave is not the ideal treatment *in vivo* due to the well-known

harmfulness to normal cell and tissue. Therefore, heat treatment by an alternating magnetic is a growing need for the development of hyperthermia in clinics.

Most of the AMF for hyperthermia experiments were using laboratory-made generators with altered frequency and magnetic fields amplitudes. The frequency scan is technically tricky due to the terms of frequency-dependent effects and resistance of magnetic applicators (Mornet *et al*, 2004; Ohno *et al*., 2002). Full-szed human prototypes have been built (shown in Figure 4.3) is clinical using for hyperthermia. Isolating or vacuum system should be used upon AMF treatment to reduce the temperature diffusion in the ambient environment (Kim *et al*., 2005), which would bring benefits of efficient temperature monitoring during the process and heat conducting between particles for lower production cycle of soften MP. AMF is generated by a 3 loops coil and water cooling system. Power generator with high power and frequency (approximately 300 kHz) can be employed to soften larger amounts of MP particles and can perform a stronger field for trauma model in a wider air gap. The gap between metal cores was designed for loading more samples and bone defects model for the future work.

# Chapter 12 Appendix

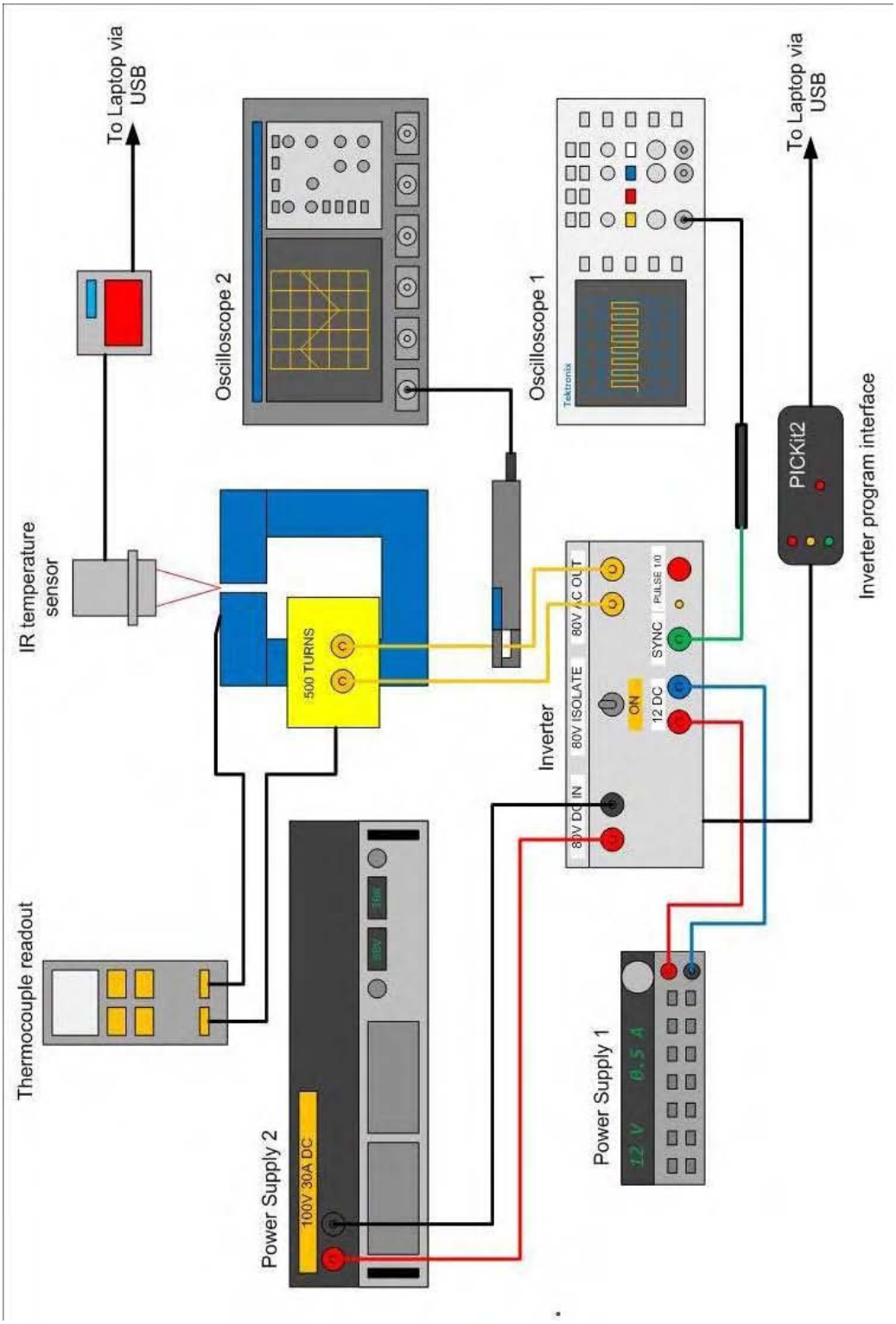


**Appendix 12.1 Schematic diagram demonstrates the AMF design (R. Dickerson).**

## Appendix 12.2 Details of the AMF (R. Dickerson)

Power Supply 2.

This is a high performance power supply. Its current is directed to the core via the inverter. It is capable of providing up to 30 A at 100 V DC, and it practiced is used up to 80 V. The refinement of the power supply has meant it is able to cope with the intermittent load provided by the set up.

Power Supply 1.

This provides a 12V DC source for the electronics in the inverter. It is regulated down to 5 V DC. It is easier to use an extra power supply than it is to reduce 100 V DC to 5 V DC.

Oscilloscope 1.

This is connected to the sync output of the inverter. The sync port provides a simpler square wave output at the same frequency as the core current. This allows the use of the frequency readout facility in 'scope 1 to quickly show the actually frequency of the inverter.

Oscilloscope 2.

This reads the output of a current clamp attached to one of the core cables. The clamp has no electrical contact, but can still read and plot the waveform of the current on 'scope 2. This is used to take RMS and peak current readings, and confirms the inverter is functioning properly.

Inverter

The inverter is a low cost solution which can be programmed to create AC voltages from Power Supply 1 by switching the polarity of its output at a frequency specified by the laptop. The voltage coming out of the inverter is dictated by Power Supply 1.The inverter is based around a microcontroller with a program embedded in it. The microcontroller control the switching of MOSFET transistors in an H-bridge configuration in order to create the AC. The frequency at which the inverter functions is dictated via the inverter's internal crystal (running at 10 MHz) and a variable embedded in the program. For simplicity of development, there is no facility for changing the frequency of the inverter without a programming interface and a copy of the original program.The PIC microcontroller contains a continuously running timer in the form of an incrementing number. Every time this number reaches that of the variable, the PIC steps through one of the four configurations the MOSFETs need to be in to create the AC waveform. The timer is then reset.

Laptop

The laptop is used to interface with the Inverter and IR temperature sensor. For the inverter, the laptop programs the frequency of the pulses. Downloading the new program and frequency onto the PIC microcontroller in the inverter requires a programming interface (PICKit2 in this case), the C18 compiler, a development environment (MPLAB in this case) and a copy of the original program. Once programmed, the inverter can work without the laptop. For the remainder of the experiment, the laptop is used to log data from the IR sensor.

Gauss Meter

The gauss meter reads the strength of the magnetic field. The probe itself is thin, allowing it to be inserted into the gap in the core. The meter gives the RMS value of the field in the core. This is used to ensure any voltage/frequency combination is not producing a field which is pointlessly small.

Thermocouple readout

This monitors the temperature of two thermocouples. Once is mounted on the core close to the sample, the other to the coil of wire. This is used to assess whether heat in the sample is coming from the AC magnetic field, or from resistive losses in the coil.

Inverter program interface

This small using is used to allow the laptop to program the PIC microcontroller in the inverter.

Resistor (not in figure)

A resistor capable of high power dissipation is used for the testing of the inverter. It has no inductive characteristics meaning the current flow is exactly the same as the voltage applied. This allows easy testing of the inverter during the development stages, but has no role in the actual MP experiments.

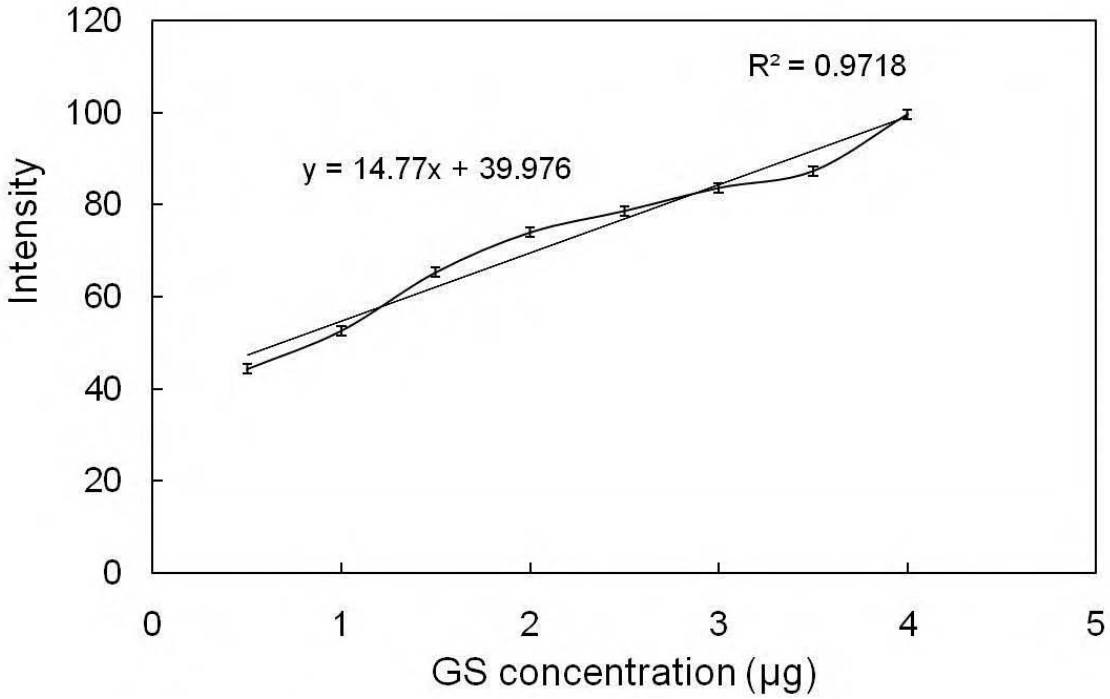


**Appendix 12.3 Calibration curve of Gentamicin release by OPA assay.**

# Chapter 13References

Abukawa, H., Papadaki, M., Abulikemu M., Vacanti, J. P., Kaban, L. B. and Troulis, M. J. 2006, "The engineering of craniofacial tissues in the laboratory: a review of biomaterials for scaffolds and implant coatings", *Dent Clin N Am*, vol. 50, pp. 205-216.

Ali, S. A. M., Zhong, S. P., Doherty, P. J. and Williams, D. F. 1993, "Mechanism of polymer degradation in implantable devices", *Biomaterials*, vol. 14, pp. 648-656.

Antunes, M. C. M. and Felisberti, M. I. 2005, "Blends of poly(hydroxybutyrate) and poly(ε-caprolactone) obtained from melting mixture", *Polímeros: Ciência e Tecnologia*, vol. 15, pp. 134-138, 2005.

Altavilla, C., Ciliberto E., Gatteschi, D. and Sangregorio, C. 2005, "A new route to fabricate monolayers of magnetite nanoparticles on silicon", *Advanced Materials*, vol. 17, no. 8, pp. 1084-1087.

Arruebo, M., Pacheco, R.F., Irusta, S., Arbiol, J., Ibarra, M.R. and Santamaría1, J. 2006, "Sustained release of doxorubicin from zeolite–magnetite nanocomposites prepared by mechanical activation", *Nanotechnology*, Vol. 17, pp. 4057-4064.

Asmatulu, R., Zalich, M. A., Claus, R. O. and Riffle, J. S. 2005, "Synthesis, characterization and targeting of biodegradable magnetic nanocomposite particles by external magnetic fields", *Journal of magnetism and magnetic materials*, vol. 292, pp. 108-119.

Babincova, M., Leszczynska, D., Sourivong, P., Cicmanec, P. and Babinec, P. 2001, "Super paramagnetic gel as a novel material for electromagnetically induced hyperthermia", *Journal of magnetism and magnetic materials*, vol. 225, pp. 109-112.

Banert, T. and Peuker, U. A. 2006, "Preparation of highly filled super-paramagnetic PMMA-magnetite nano composites using the solution method", *J Mater SCI*, vol. 41, pp. 3051-3056.

Behnia, B., Suthar, M. and Webb, A. G. 2002, "Closed-Loop Feedback Control of Phased-Array Microwave Heating Using Thermal Measurements from Magnetic Resonance Imaging", *Wiley Periodicals, Inc.*, vol. 15. pp. 101-110.

Berry, C. C., Wells, S., Charles, S. and Curtis, A. S. G. 2003, "Dextran and albumin derivatised iron oxide nanoparticles: influence on fibroblasts in vitro", *Biomaterial,*. vol. 24, pp. 4551-4557.

Bland, J. A. C. and Heinrich, B. 2005, "Ultrathin magnetic structures Ⅲ",Berlin Heidelberg, Springer-Verlag.

Bucka, B. J., Brocka, A. L., Johnsonb, W. H. and Uleryc, A. L. 2004, "Corrosion of Depleted Uranium in an Arid Environment: Soil-Geomorphology, SEM/EDS, XRD, and Electron Microprobe Analyses", *Soil and Sediment Contamination*, vol. 13, pp. 545-561.

Bucholz, R. W., 2002, "Nonallograft osteoconductive bone graft substitutes",*Clinical Orthopaedics and Related Research*, vol. 395, pp 44-52.

Bulte, J. W., Douglas, T., Witwer, B. 2001, "Magnetodendrimers allow endosomal magnetic labelling and in vivo tracking of stem cells", *Nat Biotechnol*, vol. 19, pp. 1141-1147.

Boccaccini, A. R., Erol, M., Stark, W. J., Mohn, D., Hong, Z. and Mano, J F. 2010, "Polymer/bioactive glass nanocomposites for biomedical applications: A review," *Composites Science and Technology*, vol. 70, pp. 1764–1776.

Braddock, M., Houston, P. and Campbell, C. 2001, "Ashcroft P. Born again bone: tissue engineering for bone repair", *News Physiol Sci*, vol. 16, pp. 208–13.

Brown, M.E. 2001, "Introduction to thermal analysis", 2nd ed. *Kluwer Academic Publishers*, pp. 19-52.

Burg, K. J.L., Porter, S. and Kellam, F. 2000, "Biomaterial developments for bone tissue engineering", *Biomaterial*, vol. 21, pp. 2347-2359.

Charles, S. W., 1991, "In Magnetic Properties of Fine Particles", J. L. Dormann and D. Fiorani (Eds.), North-Holland, Amsterdam.

Chang, H. I., Perrie, Y. and Coombes, A. G. A., 2006, "Delivery of the antibiotic gentamicin sulphate from precipitation cast matrices of polycaprolactone", *Journal of Controlled Release*, vol. 110, pp. 414-421.

Chen, C. 1986, "Magnetism and metallurgy of soft magnetic materials", New York: Dover Publications, Inc.

Chen, C. Y. 1993, "A study to produce magnetic fluid", Master Thesis, National Tsing Hua University, Taiwan.

Chen, C. 1986, "Magnetism and metallurgy of soft magnetic materials in chemistry", New York: Dover Publications, Inc.

Chen, D. R., Bei, J. Z. and Wang, S. G. 2000, "Polycaprolactone microparticles and their biodegradation", *Polymer Degradation and Stability*, vol. 67, pp. 455-459.

Chen, H. L., Li, L. J. and Lin, T. L. 1998, "Formation of segregation morphology in crystalline/amorphous polymer blends: molecular weight effect", *Macromolecules*, vol. 31, pp. 2255-2264.

Chouly, C., Pouliquen, D., Lucet, I., Jeune, P. and Pellet, J. J. 1996, "Development of superparamagnetic nanoparticles for MRI: effect of particles size, charge and surface nature on biodistribution", *Microencapsul*, vol. 13, pp. 245-255.

Chrischilles, E., Shireman, T. and Wallace, R. 1994, "Costs and health effects of osteoporostic fractures", *Bone*, vol. 15, pp. 377-386.

Coombes, A. G. A., Rizzi, S. C., Williamson, M., Barralet, J. E., Downes, S. And Wallace, W. A. 2004, "Precipitation casting of polycaprolactone for applications in tissue engineering and drug delivery", *Biomaterials*, vol. 25, pp. 315-325.

Crescenzi, V., Manzini, G., Calzolari, G. and Borri, C. 1972, "Thermodynamics of fusion of poly-β-propiolactone and poly-ε-caprolactone comparative analysis of the melting of aliphatic polylactone and polyester chains", *European Polymer Journal*, vol. 8, pp. 449-463.

Crowell, B. 2008, "Simple nature", Fullerton, California, www.lightandmatter.com.

Cunningham, C. H., Arai, T., Yang, P. C., McConnell, M. V., Pauly, J. M. and Conolly, S. M. 2005, "Positive contrast magnetic resonance imaging of cells labelled with magnetic nanoparticles", *Magnetic Resonance in Medicine*, vol. 53, pp. 999-1005.

Dediu V., Arisi E., Bergenti I., Riminucci A., Solzi M., Pernechele C. and Natali M. 2007, "Squid measurement of the Verwey transition on epitaxial (100) magnetite thin films", *Journal of magnetism and magnetite materials*, vol. 316, pp. 721-723.

De Julian Fernandez C., Sangregorio C., Mattei G., Saber A., Lo Russo S., Battaglin G., Catalano M. Cataruzza E. Gonella F., Gatteschi D. and Mazzoldi P. 2001, "Structure and magnetite properties of alloy-based nanoparticles silica composites prepared by ion-implantation and sol-gel techniques", *Materials Science and Engineering C*, vol. 15, pp. 59-61.

Dobson J. 2006, "Magnetic nanoparticles for drug delivery", *Drug development research*, vol. 67, pp. 55-60.

Drury J. L. and Mooney D. J. 2003, "Hydrogels for tissue engineering: scaffold design variables and applications", *Biomaterial*, vol. 24, pp. 4337- 4351.

Duffing W. J. 1990, "Electricity and magnetism", fourth edition, The McGraw-Hill International (UK) limited, University press, Cambridge.

Elliott S. R. 1998, "The physic and chemistry of solids", New York: Wiley.

Daculsi, G. and LeGeros, R. 2006, Biphasic Calcium Phosphate (BCP) Bioceramics: Chemical, Physical, and Biological Properties, *Encyclopedia of Biomaterials and Biomedical Engineering*.

Espicom Business Intelligence 2010, The global maeket for orthobiologic products, ISBN, 9781858223957.

Fields R. D., Rodriguez F. and Finn R. K. 1974, "Microbial degradation of polyesters: polycaprolactone degraded by P. pullulans", *Journal of Applied Polymer Science*, vol. 18, pp. 3571–3579.

Froum S., Cho S. C., Rosenberg E., Rohrer M. and Tarnow D. 2002, "Histological comparison of healing ectraction sockets implanted with bioactive glass or demineralized free dried bone allograft: a pilot study", *J. Periodontol*, vol. 73:1, pp. 94-102.

Fu L., Dravid V.P. and Johnson D.L. 2001, "Self-assembled(SA) bilayer molecular coating on magnetite nanoparticles", *Applied Surface Science*, vol. 181, pp. 173-178.

Getzlaff M. 2008, "Fundamentals of magnetism", Berlin Heidelberg, Springer-Verlag.

Gilchrist R. K., Medal R., Shorey W. D., Hanselman R. C., Parrott J. C. and Taylor C. B. 1957, "Selective inductive heating of lymph nodes", *Ann. Surg.*, vol. 146, pp. 596-606.

Gibson, I. R., Rehman, I., Best, S. M. and Bonfield, W. 2000, "Characterisation of the transformation from calcium-deficient apatite to β-tricalcium phosphate", *Journal of Materials Science: Materials In Medicine*, vol. 12, pp. 799-804.

Gordon R. T., Hines J. R. and Gordon D. 1979, "A biophysical approach to cancer treatment via intracellular temperature and biophysical alternations", *Med Hypothesis*, vol. 5, pp. 83-102.

Gross K. A. and Rodriguez-Lorenzo L. M. 2004, "Biodegradable composite scaffolds with an interconnected spherical network for bone tissue engineering", *Biomaterial*, vol. 25, pp. 4955-4962.

Grover L. M. 2005, "Cold setting properties of calcium phosphate-pyrophsphoric acid-water mixtures", PhD thesis, University of Birmingham.

Gubernator J., Drulis-Kawa Z. and Kozubek A. 2006, "A simply and sensitive fluorometric method for determination of gentamicin in liposomal suspensions", *International Journal of Pharmaceutics*, vol. 327, pp. 104–109.

Gupta A. K. and Gupta M. 2005, "Synthesis and surface engineering of iron oxide nanoparticles for biomaterial applications", *Biomaterials*, vol. 26, pp. 3995-4021.

Gupta A. K. and Curtis A. 2002, "Surface modification of superparamagnetic iron oxide nanoparticles and their intracellular uptake", *European cells and material*,. vol. 4, pp. 101-102.

Habraken, W. J. E. M., Wolke, J. G. C. and Jansen, J. A. 2007, "Ceramic composites as matrices and scaffolds for drug delivery in tissue engineering", *Advanced Drug Delivery Reviews*, vol. 59, pp. 234-248.

Hamley, I. W. 2003, "Nanotechnology with Soft Materials", *Angew. Chem. Int. Ed.* vol. 42, pp.1692 –1712.

Ho, S. T. and Hutmacher, D. W. 2006, "A comparison of micro CT with other techniques used in the characterization of scaffolds", *Biomaterials*, vol. 27, pp. 1362-1376.

Hohne, G.W.H., Hemminger, W.F. and Flammersheim, H. J. 2003, "Differential scanning calorimetry", second edition, Springer-Verlag Berlin Heidelberg.

Hollinger J. and Battistone G. C. 1986, "Biodegradable bone repair materials", *Clin Orthop Rel Res*, vol. 207, pp. 290-305.

Hyeon T. 2002, "Chemical synthesis of magnetite nanoparticles", *Chemical communications*, 1-18.

Hutmacher D. W. 2000, "Scaffolds in tissue engineering bone and cartilage", *Biomaterials*, vol. 21, pp. 2529-2543.

Hamoudeh M. and Fessi H. 2006, "Preparation, characterisation and surface study of poly-epsilon caprolactone magnetite microparticles", *Journal of Colloid and Interface Science*, vol. 300, pp. 584-590.

Hatch G. P. and Stelter R. E. 2001, "Magnetic design considerations for devices and particles used for biological high-gradient magnetic separation (HGMS) systems",*Journal of Magnetism and Magnetic Materials*, vol. 225. pp. 262-276.

Hergt G., Hiergeis R., Hilger I., Kaiser W. A. Lapatnikov Y., Margel S. and Richter U. 2004, "Maghemite nanoparticles with very high AC-losses for application in RF-magnetic hyperthermia", *Journal of Magnetism and Magnetic Materials*, vol. 270, pp. 345–357.

Hatakeyama H., Yoshida T. and Hatakeyama T. 2000, "The effects of side chain association on thermal and viscoelastic properties", *Journal of Thermal Analysis and Calorimetry*, vol. 59, pp. 157-168.

Huang, X. and Miao, X. 2007, "Novel porous hydroxyapatite prepared by combining H2O2 foaming with PU sponge and modified with PLGA and bioactive glass", *Journal of Biomaterials Applications*, vol. 21, pp. 351-374.

Hunt, N. C. and Grover, L. M. 2010, "Cell encapsulation using biopolymer gels for regenerative medicine", *Biotechnol Lett*, vol. 32, pp. 733–742.

Ikada Y. 2006, "Challenges in tissue engineering", *J. R. Soc. Interface*, vol. 3, pp. 589–601.

Ito A., Shinkai M., Honda H. and Kobayashi T. 2005, "Medical application of functionalized magnetic nanoparticles", *The society for biotechnology*, vol. 100, pp. 1-11.

Ito A., Hayashida M., Honda H., Hata K., Kagami H., Ueda M. and Kobayashi T. 2004, "Construction and harvest of multilayered keratinocyte sheets using magnetite nanoparticles and magnetic force", *Tissue Eng.*, vol. 10, pp. 873-880.

Jeong Y. K., Shin D. K., Lee H. J., Oh K. S., Lee J. H. and Riu D. H. 2006, "Nano magnetite particles prepared under the combined addition of urea and ammonia", *Key Engineering Materials*, vol. 317-318, pp. 203-206

Jolivet J. P., Belleville P., Tronc, E. and Livage J. 1992, "Influence of Fe(II) on the formatin of the spinel iron oxide in alkaline medium", *Clays and Clay Minerals*, vol. 40, pp. 531-539.

Johannsen M., Gneveckow U., Taymoorian K., ChoC. H., Thiesen B., Scholz R., Waldöfner N., Loening S. A., Wust P. and Jordan A. 2007, "Thermal therapy of prostate cancer using magnetic nanoparticles", *Actas Urol Esp.*, vol. 31, pp. 660-667.

Kang Y. S., Risbud S., Rabolt J. F. and Stroeve P. 1996, "Synthesis and characterization of nanometer-size $Fe_3O_4$ and $\gamma$–$Fe_2O_3$ particles", *Chem. Mater*., vol. 8, pp. 2209-2211.

Kawamura M. and Urist M. D. 1988, "Human Fibrin Is a Physiologic Delivery System for Bone Morphogenetic Protein", *Clinical Orthopaedics & Related Research*, Vol. 235, pp. 302-310.

Kendall K and Staiton C. 2001, "Adhesion and aggregation of fine particles", *Powder Technol.*, vol. 121, pp. 223-229.

Keohn, A., 2008, NuVasive acquires first stem cell bone graft substitute, Millennium Research Group, Thomson Reuters Ltd.

Kirby B.J. and Hasselbrink E.F. 2004, "Zeta potential of microfluidic substrates:
Theory, experimental techniques, and effects on separations", *Electrophoresis*. Vol. 25, pp. 187–202.

Kim D. H., Lee S. H., Kim K. N., Kim K. M., Shim I. B. and Lee Y. K. 2005, "Temperature change of various ferrite particles with alternating magnetic field for hyperthermia application", *Journal of magnetism and magnetic materials*, vol. 293, pp. 320-327.

Kim H. W., Knowles J. C. and Kim H. E. 2004, "Development of hydroxyapatite bone scaffold for controlled drug release via poly(ε-caprolactone) and hydroxyapatite hybrid coatings", *J. Biomed. Mate.r Res*. 70B: 240-249.

Kim H. W., Knowles J. C. and Kim H. E. 2004, "Hydroxypatite/poly(ε-caprolactone) composite coating on hydroxypatite porous bone scaffold for drug delivery", *Biomaterials*, vol. 25, pp. 1279-1287.

Kim K. Y., Park S. B., Park H. Y., Haam S. and Kim W. S. 2002, "Characterisation and preparation of PCL encapsulated $Fe_3O_4$ nanoparticles for targeted drug delivery system (Π) ", *Theories and Applications of Chem. Eng*., vol. 8, pp. 5182-5185.

Khalafalla S. E. and Reimers G. W. 1980, "Preparation dilution stable aqueous magnetic fluids", *EEE transactions on Magnetics,* vol. 16, pp. 178-183.

Kobayashi A., Yamamoto N., and Kirschvink J. 1997, "Studies of inorganic crystals in biological tissue: magnetite in human tumour", *Journal of Japan Society of Powder metallurgy,* vol. 44, no. 3, pp. 294-300.

Kutchko B. G. and Kim A. G. 2006, "Fly ash characterization by SEM–EDS", *Fuel*, vol. 85, pp. 2537-2544.

Kötitz R., Weitschies W., Trahms L. and Semmler W. 1999, "Investigation of Brownian and NeHel relaxation in magnetic fluids", *Journal of Magnetism and Magnetic Materials*, vol. 201, pp. 102-104.

Lee S. Y. and Harris M. T. 2006, "Surface modification of magnetic nanoparticles capped by oleic acids: characterization and colloidal stability in polar solvents", *Journal of colloid and interface scienc,*. vol. 293, pp. 401-408.

Lee Y., Lee J., Bae C. J., Park J. G., Noh H. J., Park J. H. and Hyeon T. 2005, "Large-scale synthesis of uniform and crystalline magnetite nanoparticles using reverse micelles as nanoreactors under reflux conditions", *Advanced Functional Materials,* vol. 15, pp. 503-509.

Lee Y. M., Park Y. J., Lee S. J., Ku Y., Han S. B., Choi S. M., Klokkevold P. R. and Chung C. P. 2000, "Tissue engineering bone formation using chitosan/tricalcium phosphate sponges", *J Periodontol,* vol. 71(3), pp. 410-417.

Lewin M., Carlesso N., Tung C. H., Tang X. W. and Cory D. 2000, "Tay peptide-derivatized magnetic nanoparticles allow in vivo tracking and recovery of progenitor cells", *Nat Biotechnol*, vol. 18, pp. 410-414.

Lin P. C., Ueng S. H., Yu S. C., Jan M. D., Adak A. K., Yu C. C. and Lin C. C. 2007, "Surface modification of magnetic nanoparticle via Cu(I)-catalyzed alkyne-azide [2+3] cycloaddition, ", Org. Lett., vol. 9, pp. 2131-2134.

Lobel B., Eyal O., Kariv N. and Katzir A. 2000, "Temperature controlled $CO_2$ laser welding of soft tissues: Urinary bladder welding in different animal models (rats, rabbits and cats)", *Laser Surg Med*, vol. 26, pp. 4-12.

Lobo, S. E. and Arinzeh, T. L. 2010, "Biphasic Calcium Phosphate Ceramics for Bone Regeneration and Tissue Engineering Applications", *Materials*, vol. 3, pp. 815-826.

Luciani A., Coccoli V., Orsi S., Ambrosio L. and Netti P. A. 2008, "PCL microspheres based functional scaffolds by bottom-up approach with predefined microstructural properties and release profiles", *Biomaterials*, vol. 29, pp. 4800-4807.

Ma M., Wu Y., Zhou J., Sun Y., Zhang Y. and Gu N. 2004, "Size dependence of specific power absorption of Fe3O4 particles in AC magnetic field", *Journal of Magnetism and Magnetic Materials*., vol. 268, pp. 33–39.

Mann S. and Hannington J. P. 1987, "Formation of iron oxides in unilamellar vesicles", *Journal of Colloid and Interface Science*, vol. 122, no. 2 pp. 326-335.

Matsura V., Guari Y., Larionova J., Guerin C., Caneschi A., Sangregorio C., Lancelle-Beltran E., Mehdi A. and Corriu R. J. P. 2004, "Synthesis of magnetite silica-based nanocomposites containing $Fe_3O_4$ nanoparticles", *The Royal Society of Chemistry*, vol. 14, pp. 3026-3033.

Mahadevan S., Gnanaprakash G., Philip J., Rao B.P.C. and Jayakumar T. 2007, "X-ray diffraction-based characterization of magnetite nanoparticles in presence of goethite and correlation with magnetic properties", *Physica E*. Vol. 39, pp. 20-25.

Matsura V., Guari Y., Larionova I., Gue´rin C., Caneschi A., Sangregorio C., Lancelle-Beltran E., Mehdi A. and Corriu R. J. P. 2004, "Synthesis of magnetic silica-based nanocomposites containing $Fe_3O_4$ nanoparticles", *Journal of Materials Chemistry*, vol. 14, pp. 3026-3033.

Metsger, D. S., Rieger, M. R., Foreman, D. W. 1999, "Mechanical properties of sintered hydroxyapatite and tricalcium phosphate ceramic", Journal of Materials Science: Materials In Medicine, vol. 10, pp. 9-17.

Moseke, C. and Gbureck, U. 2010, "Tetracalcium phosphate: synthesis, properties and biomedical applications", *Acta Biomaterialia*, vol. 6, pp. 3815–3823.

Mornet S., Vasseur S., Grasset F. and Duguet E. 2004, "Magnetic nanoparticle design for medical diagnosis and therapy", *Journal of Materials Chemistry*, vol. 14, pp. 2161-2175.

Morales F., Bell M. Mcdonald G. and Cole W. 1957, "The prophylactic treatment of cancer at the time of operation", *Ann Surg*, vol. 146, pp. 588-95.

Murray S. S., Murray E. J. B., Clackin C. A., and Urist M. R. 1993, "Bone Morphogenetic Protein Inhibits Differentiation and Affects Expression of Helix-Loop-Helix Regulatory Molecules in Myoblastic Cells", *Journal of Cellular Biochemistry*, Vol. 53, pp. 51-60.

Nedkov I., Merodiiska T., Slavov L., Vandenberhe R. E., Kusano Y. and Takada J. 2006, "Surface oxidation, size and shape of nano-sized magnetite obtained by co-precipitation", *Journal of magnetism and magnetic materials*, vol. 300. pp. 358-367.

Neel L. 1949, "Influence of thermal fluctuation on the magnetization of feeromagnetic small particles", *C. R. Acad. Sci*. vol. 228, pp. 664-668.

Neel L. 1953, "Thermoremanent magnetization of fine powders", *Reviews of Morden Physics*, vol. 25, pp. 293-295.

Niu J., Zhang Z. and Jiang D. 2002, “Investigation of phase evolution during the thermochemical synthesis of tricalcium phosphate", *Journal of Materials Synthesis and Processing*, vol. 9, pp. 235-240.

Nunn A. V. W., Barnard M. L., Bhakoo K., Murray J., Chilvers E. J. and Bell J. D. 1996, "Characterisation of secondary metabolites associated with neutrophil apotosis", *FEBS Lett*, vol. 392, pp. 295-298.

Odenbach S. 1993, "Magnetic fluids", *Adv. Colloid Interface Science*, vol. 46, pp. 263-282.

Oh S. H., Park I. K., Kim J. M. and Lee J. H. 2007, "In viro and in vivo characteristic of PCL scaffolds with pore size gradient fabricated by a centrifugation method", *Biomaterials*, vol. 28, pp. 1664-1671.

Ohno, T., Wakabayashi, T., Takemura, A., Yoshida, J. Ito, A., Shinkai, M., Honda, H. and Kobayashi, T. 2002, "Effective Solitary Hyperthermia Treatment of Malignant Glioma Using Stick Type CMC-magnetite. *In vivo* Study", Journal of Neuro-Oncol, vol. 56, pp. 233-239.

Okawa K., Sekine M., Maeda M., Tada M. and Abe M. 2006, "Heating ability of magnetite nanobeads with various sizes for magnetic hyperthermia at 120 kHz, a noninvasive frequency", *Journal of Applied Physics*, vol. 99, pp. 08H102-1-08H102-3.

Orcutt N. and Gandhi, O. P. 1990, "Use of the impedance method to calculate 3-D power deposition patterns for hyperthermia with capacitive plate electrodes", *IEEE Transaction on biomedical engineering*, vol. 37, pp. 36-43.

Ortner H.M. 1999, "Sampling and characterization of individual particles in occupational health studies", *J. Environ. Monit*., Vol. 1, pp. 273–283.

Pacek A.W., Ding P. and Utomo A. T. 2007, "Effects of energy density, pH and temperature on de-aggregation in nano-particles/water suspensions in high shear mixer", *Powder Technol.*, vol. 173, pp. 203-210.

Pankhurst Q. A., Connolly J., Jones S. K. and Dobson J. 2003, "Application of magnetic nanoparticles in biomedicine", *Journal of physics D: applied physic,* vol. 36, pp. 167-181.

Papell S. S. 1965, Manufacture of Magnetofluids, U.S. Patent, No.3215527

Patience C., Takeuchi Y. and Weiss R. A. 1997, "Infection of human cells by an endogenous retrovirus of pigs", *Nature Medicine,* Vol. 3, pp. 282-286.

Perez M. H., Zinutti C., Lamprecht A., Ubrich N., Astier A., Hoffman M., Bodmeier R. and Maincent P. 2000, "The preparation and evaluation of poly(ε-caplrolactone) microparticles containing both lipophilic and hydrophilic drug", *Journal of controlled release*. Vol. 65, pp 429-438.

Parthiban A., Likhitsup A., Choo F. M. and Chai C. L. L. 2010, "Triblock copolymers composed of soft and semi-crystalline segments—synthesis and characterization of poly[(n-butyl acrylate)-block-(ε-caprolactone)-block-(L-lactide)] ", *Polymer Chemistry*, vol. 1, pp. 333-338.

Perry's chemical engineering's handbook Eight edition Green D. W. and Perry R. H.

Pitt C. G., Gratzl M. M., Kimmel G. L., Surles J. and Schindler A. 1981, "Aliphatic polyester Π. The degradation od poly (DL-lactide), poly (ε-caprolactone), and their copolymers *in vivo*", *Biomaterials*, vol. 2, pp. 215-220.

Pitt C. G., Jeffcoat A. R., Zweidinger R. A. and Schindler A. 1979, "Sustained drug delivery systems. I. The permeability of poly(ε-caprolactone), poly(DL-lactic acid), and their copolymers", *Journal of Biomaterials Research*, vol. 13, pp. 497-507.

Placidi M. and Cannistraro S. 1998, "A dyamic light scattering study on mutual diffusion coefficient of BSA in concentrated aqueous solutions", *Europhysics Letters*. Vol.43, pp. 476-481.

Rawle A., "Basic principles of particle size analysis", *Technical paper. Malvern Instruments Lit*.

Redl F. X., Black C. T., Papaefthymiou G. C., Sandstrom R. L., Yin M., Zeng H., Murray C. B. and O'Brien S. B. 2004, "Magnetic, Electronic, and Structural Characterization of

Nonstoichiometric Iron Oxides at the Nanoscale", *J. AM. CHEM. SOC.*, vol. 126,pp. 14583-14599

Reeve J. and Metz D. 1998, "AgeNet workshop on ageing fragility and the biomechanics of bone", *AgeNet Report*, pp. 1-3.

Reimers G. W. and Khalafalla S. E. 1972, "Preparing magneticfluids by a peptizing method", *US Bureau Mines Tech Rep*, vol. 59, pp.228-881.

Revil A., Pezard P.A. and Glover P. W. J. 1999, "Streaming potential in porous media 1. Theory of the zeta potential", *Journal of Geophysical Research*, Vol. 104, pp. 20021-20032.

Rezwan K., Chen Q. Z., Blaker J. J. and Boccaccini A. R. 2006, "Biodegradable and bioactive porous polymer/inorganic composite scaffolds for bone tissue engineering", *Biomaterials*, vol. 27, pp. 3413–3431.

Rhee S. H. 2003, "Effect of molecular weight of poly(ε-caprolactone) on interpenetration network structure, apatite-forming ability, and degradability of poly(ε-caprolactone)/silica nano-hybrid materials", *Biomaterials*, vol. 24, pp. 1721-1727.

Richardson T. P., Peters M. C., Ennett A. B. and Mooney D. J. 2001, "Polymetric system for dual growth factor delivery", *Nature Biotechnology*, vol. 19, pp. 1029-1034.

Rosa M. D., Carteni M., Petillo O., Calarco A., Margarucci S., Rosso F., Rosa A., Farina E., Grippo P. and Peluso G. 2004, "Cationic polyelectrolyte hydrogel fosters fibroblast spreading, proliferation, and extracellular matrix production: implications for tissue engineering*", Journal of cellular physiology*, vol. 198, pp. 133-143.

Rosensweig R.E. 2002, "Heating magnetic fluid with alternating magnetic field", *Journal of Magnetism and Magnetic Materials*, vol. 252, pp. 370-374.

Safarik I. and Safarikova M. 2004, "Magnetic techniques for the isolation and purification of proteins and peptides", *BioMagnetic Research and Technology*, vol. 2, pp. 1-17.

Saad G. R., Khalil T. M. and Sabaa M. W. J. 2010, "Photo- and bio-degradation of poly(ester-urethane)s films based on poly[(R)-3-Hydroxybutyrate] and poly(ε-Caprolactone) blocks", *Polym Res*., vol. 17, pp. 33–42.

Sahoo S. K., Panyam J., Prabha S. and Labhasetwar V. 2002, "Residual polyvinyl alcohol associated with poly 9D, L-lactide-co-glycolide) nanoparticles affects their physical properties and cellular uptake", *J. of Controlled and Release*, vol. 82, pp. 105-114.

Sahoo Y., Goodarzi A., Swihart M. T., Ohulchanskyy T. Y., Kaur N., Furlani E. P. and Prasad P. N. 2005, "Aqueous Ferrofluid of Magnetite Nanoparticles: Fluorescence Labeling and Magnetophoretic Control", *J. Phys. Chem. B*, vol. 109, pp. 3879-3885.

Sahool Y., Pizem H., Fried T., Golodnitsky D., Burstein L., Sukenik C. N. and Markovich G. 2001, "Alkyl phosphonate/phosphate coating on magnetic nanoparticles: a comparison with faty acids", *Langmuir*, vol. 17, pp. 7907-7911.

Saini S., Stark D. D., Hahn P.F., Wittenberg J., Brady T. J. and Ferrucci J.T. 1987, "Ferrite particles: a superparamagnetic MR contrast agent for the reticuloendothelial system", *Radiology*, vol. 162, pp. 211-216.

Sanders J. P and Gallagher P. K. 2003, "Kinetics of the oxidation of magnetite using simultaneous TG/DSC", *Journal of Thermal Analysis and Calorimetry*, vol. 7272, pp. 777.789.

Schmelzeisenn R., Schimming R. and Sittinger M. 2003, "Making bone: implant insertion into tissue-engineered bone for maxillarysinus floor augmentation—a preliminary report", *Journal of Cranio-Maxillofacial Surgery*, vol. 21, pp. 34-39.

Schnieders J., Gbureck U., Thull R. and Kissel T. 2006, "Controlled release of gentamicin from calcium phosphate-poly(lactic acid-co-glycolic acid) composite bone cement", *Biomaterials*, vol. 27, pp. 4239-4249.

Scholten P. C. 1983, "How magnetic can a magnetic fluid be?", *Int. Magn. Mater*, vol. 39, pp. 99-106.

Seol Y. J., Lee J. Y., Park Y. J., Lee Y. M., Ku Y., Rhyu I. C., Lee S. J., Han S. B. and Chung C. P. 2004, "Chitosan sponges as tissue engineering scaffolds for bone formation", *Biotechnology Letters,* vol. 26, pp.1037-1041.

Simon M. D. and Geim A. K., 2000, "Diamagnetic levitation: Flying frogs and floating magnets ", *Journal of Applied Physics,* vol. 87, pp. 6200.

Sinha V.R., Bansal K., Kaushik R., Kumria R. and Trehan A. 2004, "Poly-ε-caprolactone microspheres and nanospheres: an overview", *International Journal of Pharmaceutics*, vol. 278, pp. 1-23.

Sorensen C. M. in: Klabunde K. J., editor. 1998, "Nanoscale materials in chemistry", New York: Wiley.

Stock U. A. and Vacanti J. P. 2001, "Tissue engineerng: Current State and Prospects", *Annu. Rev. Med,* vol. 52, pp. 443–51.

Sun Z. X., Su F. W., Forsling W. and Samskog P. O. 1998, "Surface characteristics of magnetite in aqueous suspension", *Journal of colloid and interface science*, vol. 197, pp. 151-159.

Stevens, B., Yang, Y., Mohandas, A., Stucker, B. and Nguyen, K. T. 2008, "A Review of Materials, Fabrication Methods, and Strategies Used to Enhance Bone Regeneration in Engineered Bone Tissues", *Journal of biomedical materials research Part B: applied biomaterials*, vol. 85B, pp. 573-582.

Shimoiizaka, J. 1966, "Flocculation and dispersion of powders in liquids", *Funtai Oyobi Funmatsuyakin (Japan Soc. Powder and Powder Metallurgy)*, vol. 13, pp. 263-274.

Tang Z. G., Black R.A., Curran J. M., Hunt J. A., Phoodes N. P. and Williams D. F. 2004, "Surface properties and biocompatibility of solvent-cast poly[e-caprolactone] films", *Biomaterials*, vol. 25, pp. 4741-4749.

Teixeira J. O. C. and Urist M. D. 1998, "Bone morphogenetic protein induced repair of compartmentalized segmental diaphyseal defects", *Arch Orthop Trauma Surg*, Vol. 117, pp. 27-34.

Terris B. D. and Thomson T. 2005, "Nanofabricated and self-assembled magnetic structures as data storage media", *Journal of physics D: Applied Physics*, vol. 38, pp. 199-222.

Thapa D., Palkar V. R., Kurup M. B. and Malik S. K. 2004, "Properties of magnetite nanoparticles synthesized through a novel chemical route", *Material letters*. Vol. 58, 99. 2692-2694.

Tombacz E., Majzik A., Horvat Z. S. and Illes E. 2006, "Magnetite in aqueous medium coating its surface and surface coated with it", *Romanian Reports in Physics*, vol. 58, pp. 281–286.

Turcu R., Nan A., Craciunescu I., Pana O., Leostean C. and Macavei S. 2009, "Smart composites based on magnetic nanoparticles and responsive polymers", *Journal of Physics: Conference series*, vol. 182, pp. 1-4.

Ural E., Kesenci K., Fambri L. Migliaresi C. and Piskin E. 2000, "Poly(D, L-cactide/ ε-caprolactone)/hydroxypatite composites", *Biomaterials*, vol. 21, pp. 2147-2154.

Wada S., Tazawa K., Furuta I. and Nagae H. 2003, "Antitumor effect of new local hyperthermia using dextran magnetite complex in hamster tongue carcinoma", *Oral Dis*, vol. 9, pp. 218-223.

Wang, L., Shelton, R. M., Cooper, P. R., Lawson, M., Triffitt, J. T. and Barralet, J. E. 2003, "Evaluation of sodium alginate for bone marrow cell tissue engineering", *Biomaterial*, vol. 24, pp. 3475-3481.

Wang Y., Chang H. I., Wertheim D. F., Jones A. S., Jackson C. and Coombes A. G. A. 2007, "Characterisation of the macroporosity of polycaprolactone-based biocomposites and release kinetics for drug delivery", *Biomaterials*, vol. 28, pp. 4619-4627.

Wei G. and Ma P. X. 2004, "Structure and properties of nano-hydroxyapatite/polymer composite scaffolds for bone tissue engineering", *Biomaterial*, vol. 25, pp. 4749-4757.

Weissleder R., Bogdanov A., Neuwelt E. A. and Papisov M. 1995, "Long circulation iron oxides for MR imaging", *Adv. Drug Deliv Rev,* vol. 16, pp. 321-334.

Weissleder R., Moore A., Mahmood U., Bhorade R., Benveniste H., Chiocca E. and Basilion J. B. 2000, "In vivo MR imaging of transgene expression", *Nat Med,* vol. 6, pp. 351-355.

Williams J. M., Adewunmi A., Schek R. M., Flanagan C. L., Krebsbach P. H., Feinberg S. E., Hollister S. J. and Das S. 2005, "Bone tissue engineering using polycaprolactone scaffolds fabricated via selective laser sintering", *Biomaterials,* vol. 26, pp. 4817-4827.

Woo K., Hong J. Choi S., Lee H., Ahn J., Kim C. and Lee S. W. 2004, "Easy synthesis and magnetic properties of iron oxide nanoparticles", *Chem. Mater,* vol. 16, pp. 2814-2818.

Xiong Z., Yan Y., Zhang R. and Sun L. 2001, "Fabrication of porous poly(L-lactic acid) scaffolds for bone tissue engineering via precise extrusion", *Scripta Materialia,* vol. 45, pp. 773-779.

Yamaguchi A., Nasu S., Tanigawa H., Ono T., Miyake K., Mibu K. and Shinjo T. 2005, "Effect of Joule heating in current-driven domain wall motion", *Applied Physicsc Letters,* vol. 86, pp. 012511-1-01251-3.

Yang F. Wolke J. G. C. and Jansen J. A. 2008, "Biomimetic calcium phosphate coating on electrospun poly (ε-caprolactone) scaffolds for bone tissue engineering", *Porous Inorganic Materials for Biomedical Applications,* vol. 137, pp. 154-161.

Yashimoto H., Shin Y. M., Terai H. and Vacanti J.P. 2003, "A biodegradable nanofiber scaffold by electrospinning and its potential for bone tissue engineering", *Biomaterials,* vol. 24, pp. 2077-2082.

Yin Y., Ye F., Cui J., Zhang F., Li X. and Yao K. 2003, "Preparation and characterization of macroporous chitosan-gelatin/β-tricalcium phosphate composite scaffolds for bone tissue engineering", *Wiley Periodicals,Inc,* pp.845-855.

Yoshizawa S., Fourmy D. and Puglisi J. D. 1998, "Structure origins of gentamicin antibiotic action", *The EMBO Journal*, vol. 17, pp. 6437-6448.

Yoon, D. M. and Fisher, J. P. 2006, "Polymeric Scaffolds for Tissue Engineering Applications," in *The Biomedical Engineering Handbook: Tissue Engineering & Artificial Organs*, 3 edn, Joseph D.Bronzino, ed., Taylor & Francis Group, pp. 37-1-37-18.

Zalipsky S. 1995, "Functionalized Poly(ethy1ene glycol) for Preparation of Biologically Relevant Conjugates", *Bioconjugafe Che,* vol. 6, pp. 150-1 65.

Zaitsev V. S., Filimonov D. S., Presnyakov I. A., Gambino R. J. and Chu B. 1999, "Physical and chemical properties of magnetite and magnetite-polymer nanoparticles and their colloidal dispersions", *J. Colloid Interface Sci.* vol. 212, pp. 49-57.

Zambaux M. F., Bonneaux F. and Gref F. 1998, "Influence of experimental parameters on the characteristics of poly (lactic acid) nanoparticles prepared by a double emulsion method", *J. Controlled Release*, vol. 50, pp. 31-40.

Zhang J. and Misra R. D. K. 2007, "Magnetic drug-targeting carrier encapsulated with thermosensitive smart polymer: core-shell nanoparticle carrier and drug release response", *Acta Biomaterialia,* vol. 3, pp. 838-850.

Zhang Y., Kohler N. and Zhang M. 2002, "Surface modification of superparamagnetic magnetite nanoparticles and their intracellular uptake", *Biomaterials*, vol. 23, pp. 1553–1561.

Zhao M., Beauregard D. A., Loizou L., Davletov B. and Brindle K. M. 2001, "Non-invasive detection of apoptosis using magnetic resonance imaging and a targeted contrast agent", *Nat Med*, vol. 7, pp. 1241-1244.